University of Milano - Bicocca
Faculty of Mathematics, Physics and Natural Sciences
Department of Geological Sciences and Geotechnologies
PhD Course XXIII Cycle

EO-ALPINE EVOLUTION OF THE CENTRAL SOUTHERN ALPS INSIGHTS FROM STRUCTURAL ANALYSIS AND NEW GEOCHRONOLOGICAL CONSTRAINTS

PAOLO D'ADDA

2010

University of Milano - Bicocca
Faculty of Mathematics, Physics and Natural Sciences
Department of Geological Sciences and Geotechnologies
PhD Course XXIII Cycle

EO-ALPINE EVOLUTION OF THE CENTRAL SOUTHERN ALPS INSIGHTS FROM STRUCTURAL ANALYSIS AND NEW GEOCHRONOLOGICAL CONSTRAINTS

PhD Student:
Paolo D'Adda
Matr: 033064

Tutor:
Prof. Andrea Zanchi

Co-tutors:
Dr. Stefano Zanchetta
Dr. Maria A. Bergomi
Dr. Marco Malusà

CONTENTS

Abstract.....1

Chapter 1.

Introduction.....3

1.1 Motivations and purposes of the work.....4

1.2 Previous works.....5

1.3 Structural setting of the Central Southern Alps (CSA).....8

1.4 Study areas.....11

Chapter 2.

Alpine deformations and relative chronology Central Southern Alps.

Field data and structural analysis.....13

2.1 Alpine deformations in the Orobic basement. Structural analysis along the Orobic and Porcile thrusts.....14

2.1.1 Introduction.....14

2.1.2 Geological & structural map of the Orobic thrust–Porcile thrust triple junction (*Plate1*).....15

2.1.3 Cleavage, folds and fault analyses.....19

2.1.4 Pseudotachylytes along the Orobic and Porcile thrusts: fabric and petrography.....24

2.1.5 Relative chronology of Alpine deformational events along the Orobic and Porcile thrusts.....27

2.2 Polyphase deformations in the Triassic cover: syn-thrust structures and relative chronology in the Grem-Vedra Transverse Zone.....30

2.2.1 Introduction.....30

2.2.2 The Grem – Vedra Transverse Zone (GVTZ).....31

2.2.3 Description of tectonic units and fault zones.....34

- Tectonic units of the GVTZ area.....34

- The main fault zones of the GVTZ.....39

2.2.4 A 3D model of the GVTZ.....42

2.2.5 Structural evolution of the GVTZ during Alpine tectonics.....44

- First pre-Adamello compressional stage.....45
- Second pre-Adamello compressional stage.....46
2.2.6 Syn-thrust deformations in the GVTZ.....47

2.3 Relationships between thrusting and dyke emplacement in the Gandino and Presolana areas.....51
2.3.1 Introduction.....51
2.3.2 The Gandino area.....51
- Stratigraphic succession.....51
- Tectonic units and regional structures.....51
- Magmatic bodies.....55
- Mesostructural analysis.....56
2.3.3 The Presolana area.....59
- Tectonic units and regional structures.....59
- Magmatic bodies.....60
2.3.4 Petrography and geochemistry of magmatic bodies.....60
2.3.5 Relative chronology between thrusting, faults and dykes.....62

Chapter 3.
Geochronological constraints for Alpine tectonics in the Central Southern Alps.....65

3.1 $^{40}Ar/^{39}Ar$ dating of fault-related pseudotachylytes along the Orobic and Porcile thrusts.....66
3.1.1 The $^{40}Ar/^{39}Ar$ method applied to pseudotachylytes: assumptions and problems.....66
3.1.2 $^{40}Ar/^{39}Ar$ results.....67

3.2 SHRIMP U-Th-Pb dating of magmatic bodies: results from the Gandino and Presolana areas.....74

3.3 Fission track dating of apatites from the Gandino area.....77
3.3.1 General principles.....77
3.3.2 Results from the Gandino area.....78

Chapter 4.

Discussion: The Alpine tectonic evolution of the CSA.....79

4.1 Significance of the new geochronological constraints for the Alpine evolution of the CSA.....80

4.2 Implications for the Alpine orogeny.....85

Chapter 5.

Conclusions.....89

References.....93

Acknowledgements.....107

Appendix 1 – $^{40}Ar/^{39}Ar$ dating of fault-generated pseudotachylytes.....109

Appendix 2 – SHRIMP U-Th-Pb analytical techniques.....113

Appendix 3 – Apatite fission track dating.....115

Plate 1 – Geological & structural map of the Orobic thrust – Porcile thrust triple junction

ABSTRACT

The timing of the Alpine deformation in the Central Southern Alps (CSA or Orobic Alps) has always been a debated topic, since the scarcity of reliable absolute age constraints has prevented an accurate chronological reconstruction of the evolution of this sector of the European Alps.

In this work, detailed structural analyses performed in different areas of the CSA allowed us to distinguish different compressive features within both the crystalline basement and the sedimentary cover. The integration of these field data with new isotopic data provides time constraints for the reconstruction of the evolution of the CSA during the Alpine orogeny.

In the northern sector of the belt a Variscan polymetamorphic basement is stacked southward on the Permian to Mesozoic cover along two main regional faults (Orobic and Porcile thrusts). Fault zones, slightly postdating a first folding event of Alpine age (D3), experienced a complex evolution through the ductile and brittle deformation regime, showing greenschists facies mylonites overprinted by a penetrative cataclastic deformation (D4). Generation of fault-related pseudotachylytes marks the onset of brittle conditions, lasting up to the youngest episodes of fault activity.

Thrusting along this structures also produced thrusting within the Permian-Triassic cover with the formation of different south-verging thrust stacks. This first thrusting event was followed by the activation of new deeper thrust surfaces leading to the emplacement of three regional anticlines (Orobic Anticlines) which tilted to the south the previously stacked units. During this long compressive stage (Orobic-Porcile thrusts and Orobic Anticlines) the sedimentary cover of the CSA was also involved in thrusting and different stacks of Mesozoic units were emplaced to the south. $^{40}Ar/^{39}Ar$ dating of the pseudotachylyte matrix of 9 samples from both the Orobic and Porcile thrusts give two separated age clusters: Late Cretaceous (80-68 Ma) and Early to Middle Eocene (55-43 Ma). These new data provide evidence that the pre-Adamello evolution of the CSA was characterized by the superposition of different tectonic events accompanying the exhumation of the deepest part of the belt through the brittle-ductile transition. The oldest pseudotachylyte ages demonstrate that south-verging regional thrusting in the CSA was already active during the Late Cretaceous, concurrently with both the HP metamorphism that affected the Austroalpine units of the eastern Alps, and the development of a syn-orogenic foredeep basin where the Upper Cretaceous Lombardian Flysch was deposited.

In the Early to Middle Eocene a minor reactivation of the Orobic and Porcile thrusts occurred, as testified by the youngest pseudotachylyte ages obtained by $^{40}Ar/^{39}Ar$ dating. This event was probably related with the closure of the Ligurian-Piedmont and the ongoing of the Europe-Adria collision.

South of the Orobic Anticlines system the Triassic sedimentary succession is stacked into several units bounded by south-verging low-angle thrust faults, which are related to different steps of crustal shortening. Different thrust stacks occur within the Triassic cover between the Como Lake to the west and the Adamello batholith to the east. They usually have an antiformal arrangement and are separated by each other by different N-S trending transverse zones, such as the poorly known Grem-Vedra Transverse

Zone (GVTZ), formed during complex deformational phenomena in a transpressional regime coeval with thrust emplacement. The GVTZ formed during the southward imbrication of the older thrust sheets of the Menna-Arera group, strongly interacting with syn-thrust ductile structures, and was reactivated during the growth of the Orobic Anticlines belt. The GVTZ and other transverse zones of the CSA probably reflect the occurrence of pre-existing fault systems that characterize the Norian to Jurassic rifting history of the Lombardian basin, and were reactivated as strike-slip features during Alpine tectonics.

In the Gandino and Presolana areas thrust surfaces are cut by high-angle extensional and strike-slip faults, which controlled the emplacement of hypabissal magmatic intrusions that post-date thrusts motions. Intrusion ages based on SHRIMP U-Th-Pb zircon dating span between 42±1 and 39±1 Ma, suggesting close time relationships with the earliest Adamello intrusion stages and, more in general, with the widespread calc-alkaline magmatism described in the Southern Alps. Fission track ages of magmatic apatites are indistinguishable from U-Pb crystallization ages of zircons, suggesting that the intrusion occurred in country rocks already exhumed above the partial annealing zone of apatite (depth < 2-4 km).

These data indicate that the northern and central sectors of the CSA were already structured and largely exhumed in the Middle Eocene and no major internal deformations has occurred in these areas after the Bartonian. Neogene deformations were instead concentrated further south, along the frontal part of the belt (Milano Belt).

These new data provide a direct evidence that thrusting and nappe stacking were active during Late Cretaceous times not only in the Eastern Alps, but also in the CSA, significantly extending southward the sector of the Alpine belt affected by the Cretaceous orogenic event. In this view, the Late Cretaceous Southern Alps can be interpreted as the south-verging retrobelt of a pre-collisional orogenic wedge, which formed during the subduction of the Alpine Tethys beneath the attenuated northern Adria margin.

Chapter 1

INTRODUCTION

1.1 Motivations and purposes of the work

The definition and dating of deformational events in orogenic belts is a crucial problem for the reconstruction of their structural history. Crosscutting relationships among folds, faults and intrusive rocks, coupled with radiometric dating of syntectonic minerals and stratigraphic analysis in nearby sedimentary basins, provide reliable constraints for regional tectonic reconstructions.

In the Southern Alps of northern Italy, the relative chronology of major deformation events has been the subject of several regional reconstructions (Laubscher 1985; Schönborn 1992; Castellarin et al. 2006). However, the absence of reliable time markers has still now hampered a precise interpretation of the timing of the Alpine deformation in this area.

The Central Southern Alps (CSA or Orobic Alps) represent the south-verging retro-belt of the European Alps (Laubscher 1985; Schönborn 1992; Carminati et al. 1997), separated from the axial belt by the E-W trending Insubric Fault (Schmid et al. 1987). They represents an impressive example of thick-skinned fold-and-thrust belt (Schönborn 1992; Forcella and Jadoul 2000; Carminati 2009). During the Alpine orogenic event the CSA experienced severe shortening that took place along generally E-W trending, S-verging, thrusts and faults, under low-grade to non-metamorphic conditions. The amount of shortening and the absolute and relative age of emplacement of the several thrust sheets are still a matter of debate. One of the crucial issues is the age of the beginning of the Alpine deformation, supposed to be Cretaceous only on the base of indirect evidence. Stratigraphic and structural data roughly constrain the age of the

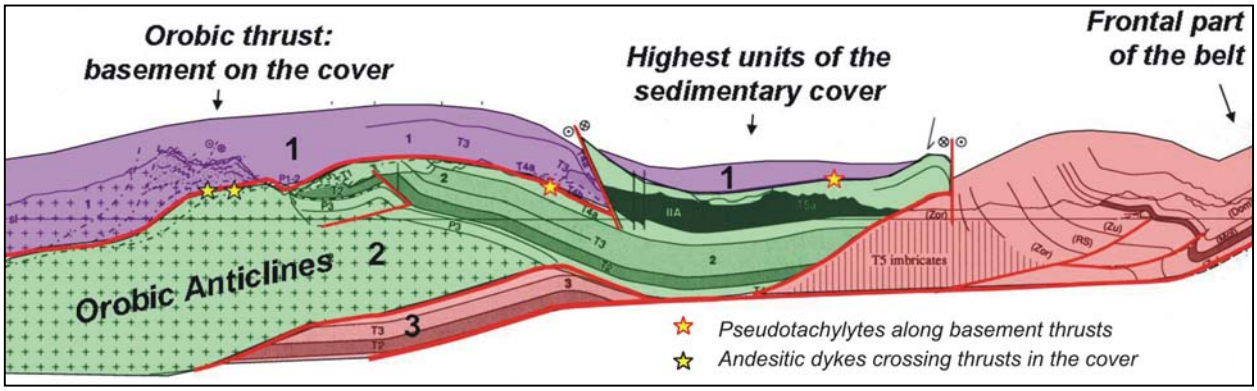

Fig. 1.1.1 Simplified geological section across the CSA (modified from Schönborn 1992). The emplacement of thrust sheets in the northern sector of the belt (involving basement units) caused southward thrusting also within the sedimentary cover. Find links and relationships between these units, and provide a chronological reconstruction for their emplacement using new reliable radiometric data, are the main objectives of this work.

main compressive phases in the Late Cretaceous – Early Tertiary time interval, i.e. during/after the deposition of the Cretaceous turbidites of the Lombardian Basin (Doglioni and Bosellini 1987; Bernoulli and Winkler 1990; Bersezio et al. 1993) and the emplacement of the southern Re di Castello unit (42 Ma) of the Adamello batholith, sealing the main structures. Existing sparse radiometric data on mafic to intermediate dykes, showing different relationships with the main structures, range between 63 Ma for andesitic dykes intruded in the Presolana stack (Zanchi et al. 1990a) and 50-35 Ma for dykes swarms near Gandino (Fantoni et al. 1999). The large time interval shown by these age determinations, does not provide reliable constraints on the first stages of Alpine deformation in the CSA.

Aim of this work is to provide a reconstruction of the deformational events which led to the emplacement of the main thrust sheets in the CSA. Furthermore, such reconstructed structural evolution is anchored to new reliable radiometric age data.

New structural data will be presented and discussed together with new $^{40}Ar/^{39}Ar$ data obtained on fault-related pseudotachylyte veins, U-Th-Pb zircon ages and apatite fission track data on dykes displaying clear crosscutting relationships with the main tectonic structures.

The new proposed model will be finally discussed in the light of the Alpine orogeny, in order to understand the role that the CSA played during the progressive closure of the Alpine Tethys, the subsequent continent-continent collision and the subduction of the European margin below Adria plate.

1.2 Previous works

Already at the end of ‘800 and in the first decades of ‘900 the Orobic sector of the Southern Alps (CSA) was the subject of geological studies (i.e. Taramelli 1890; Philippi 1895; Porro 1903; Trümpy 1930). These works represented the starting point for many subsequent stratigraphic, paleontological and structural studies, many of which were aimed to the understanding the setting and the structural evolution of this sector of the European Alps. As summarized in De Sitter and De Sitter-Koomans (1949) the first important works on the structural evolution of the CSA were realized by a group of Dutch authors. They proposed the concept of “gravitational tectonics” based on the assumption that differential uplift of the crystalline basement was the cause of sliding of the sedimentary cover to the south. This gravitational model excluded basement and cover shortening (De Sitter 1963; De Jong 1979) and was not questioned until the late 1970’s. In fact, Castellarin (1979) and Gaetani and Jadoul (1979) assumed that shortening was the main cause of the emplacement of thrust sheet within the sedimentary cover. Laubscher (1985) was he first to recognize a link between the Orobic basement thrusts and the sedimentary *décollement surfaces*. He constructed generalized balanced cross-sections and suggested that the basement-Permian anticlines developed south of the Orobic thrust are ramp folds of deeper thrust systems. Publication of seismic lines across the Po Plain (Pieri and Groppi 1981) revealed the occurrence of a deeply buried fold-and-thrust system, named “Milano Belt” by Laubscher (1985). After these fundamental works different studies were focused on the reconstruction of the structural setting within the sedimentary cover (i.e. Forcella 1988; Bersezio and Fornaciari 1988; Milano et al. 1988; Zanchi et al. 1990a) and Roeder (1992) proposed a model linking the buried structures of the frontal part of the belt with those of the exposed sectors to the north. Moreover, the relationships between the Orobic structures and the tertiary Adamello batholith (e.g. Brack 1981; Brack 1984) began to be investigated, while Zanchi et al. (1990a) provided the first radiometric datings of some andesitic dykes which cut across the main thrust stacks of the Triassic cover.

The most complete and comprehensive structural model of the CSA was proposed by Schönborn (1992) who summarized the results of previous studies and proposed, on the basis of new field data, a general reconstruction of the evolution of the belt during the Alpine orogeny (Fig. 1.2.1). He also constructed

several balanced cross-sections postulating a total shortening of 80-120 km during different N-S directed compressive events. On the basis of this excellent work many other studies have been then realized.

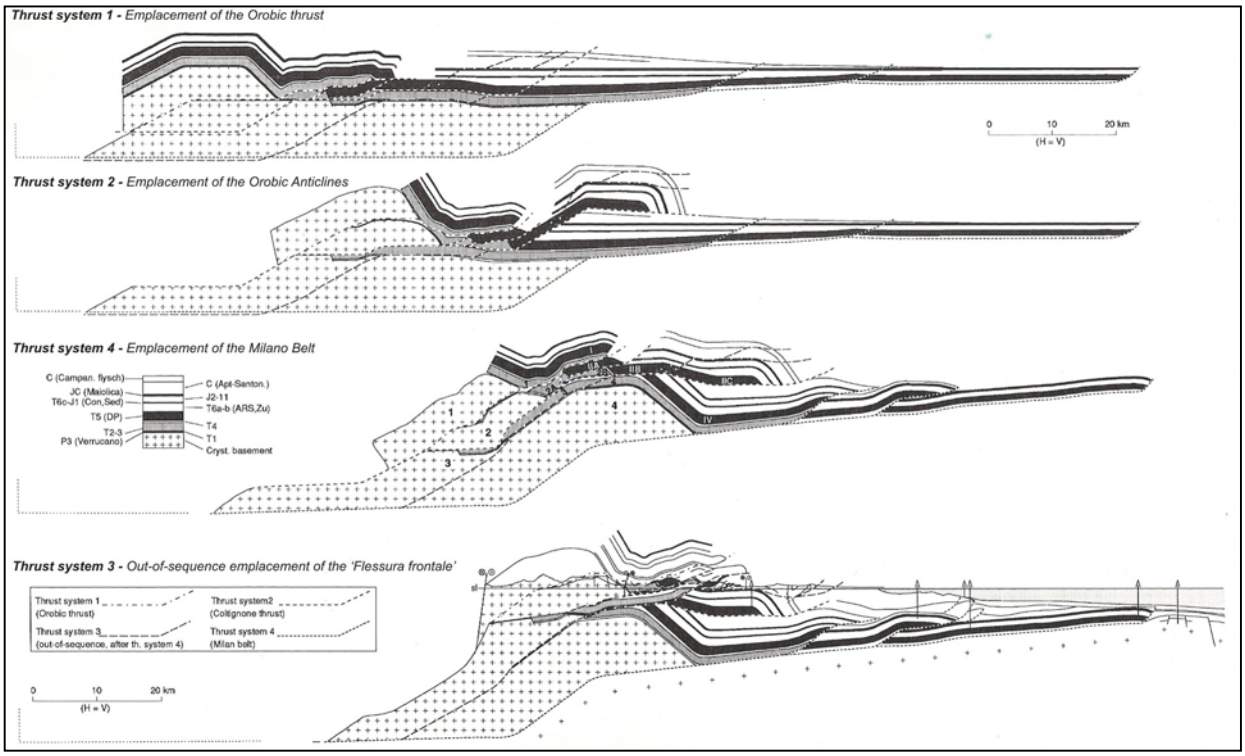

Fig. 0.2.1 Structural evolution of the CSA proposed in the Schönborn's (1992) model. Thrust system 1 led to the emplacement of the Orobic thrust (and related units within the Triassic cover) and was followed by the growth of the Orobic Anticlines during Thrust system 2. After the second stage of thrusting the emplacement of the Adamello batholith occurred. The successive stage of shortening (Thrust system 4) caused the stacking of several units in the frontal part of the belt (Milano Belt) and was finally followed by the growth of the 'Flessura Frontale due to the activation of and out-of-sequence thrust.

Detailed descriptions of the structures of the Orobic sector have been provided for both the basement (i.e. Siletto et al. 1993; Carminati and Siletto 1997; Spalla and Gosso 1999; Spalla et al. 1999; Colombo and Tunesi 1999; Carminati 2009) and the sedimentary cover (i.e. Bersezio et al. 1993, 1997, 2001; Forcella and Jadoul 2000; Di Giulio et al. 2001; Fantoni et al. 2004; Schiunnach and Tremolada 2004; Ravaglia et al. 2006).

The crystalline basement of the CSA is mainly composed by metapelites and metapsamnites with minor metagranitoids, and is the results of metamorphic events related to the Variscan orogeny. Two different pre-Alpine, syn-metamorphic deformational phases are recognizable, traditionally known in the literature as D1 and D2. Structures related to the D1 phases are associated to an amphibolite-facies metamorphic event occurred around 330 Ma, while D2 structures formed before 280 Ma ago during a greenshists-facies event (Diella et al. 1992). S2 schistosity is the most pervasive foliation at the regional scale and locally shows a mylonitic character, obliterating pre-existing fabrics. Although the characters of the metamorphic products of the pre-Alpine events and related deformational structures are quite uniform, some differences have been recognized. The reconstruction of the P-T-t paths in different areas of the exposed basement allowed to identify four different 'tectono-metamorphic' units (Milano et al. 1988; Diella et al. 1992; Albini et al. 1994; Maroni et al. 1995; Cadel et al. 1996; Spalla et al. 1999) suggesting that a complex evolution occurred in the Southern Alps during the Variscan event. The onset of the

Alpine orogeny strongly interested the CSA, producing shortening and further deformations in the crystalline basement. At least two main compressive events have been recognized, generally known as D3 and D4 (Cassinis et al. 1986; Cadel et al. 1996; Milano et al. 1988; Carminati et al. 1997) and related to the formation of south-verging folds and thrusts. The D3 event caused the formation of chevron to sub-isoclinal folds, generally not associated to the development of an axial plane schistosity. These structures usually trend E-W, with N-dipping planes although in some areas (i.e. near the San Marco pass, as indicated by Carminati and Siletto 2005 and Zanchetta et al. 2010) they are partially rotated, showing N-NE dipping axes. The D4 phase is less pervasive and produces ENE-WSW oriented shear zones related with the occurrence of crenulation cleavages and kink folds.

Some authors described the tectonic contacts between basement and cover (Blom and Passchier 1997; Cadel et al. 1996; Carminati et al. 1997; Carminati and Siletto 2005) while other works were focused on the deformations within the sedimentary cover. During the Alpine compressions the Permian to Caenozoic sedimentary cover of the CSA was also strongly affected by deformations, with the development of several thrust surfaces along which a substantial shortening occurred (Laubsher 1985; Schönborn 1992). Different authors (i.e. Forcella 1988; Zanchi et al. 1990a; Berra et al. 1991; Bersezio et al. 1997) investigated the structural setting and the deformations through the Triassic succession, suggesting that it was mainly deformed during the earliest stages of compression, when several thrust stacks were formed. The emplacement of these structures was followed by the intrusion of the Adamello batholith, from the Middle Eocene. Different authors investigated the relationships between the pluton and the previously formed structures, also providing radiometric ages for magma emplacement (i.e. Brack 1981; Brack 1984; Callegari and Brack 2002 for a review).

In other works the first radiometric data on the age of magmatic bodies of the CSA and fault rocks were published. Fantoni et al. (1999) proposed new dating of some tertiary magmatic products of the CSA (previously dated by Zanchi et al. 1990a) and Meier 2003 provided the first $^{40}Ar/^{39}Ar$ dating of pseudotachylyte veins along the Orobic and Porcile thrusts. At the same time new zircon U/Pb ages for the Adamello batholith were provided by Mayer et al. (2003).

Some other authors investigated the structures of the southern part of the CSA. The pioneer work of Pieri and Groppi (1981), based of seismic and borehole studies, revealed the occurrence of a series of embricated thrust units buried below the Po Plain Plio-Quaternary fill. The emplacement of these structures was related by Laubscher (1985) and Schönborn (1992) to the youngest phases of shortening in the CSA.

On the basis of most of these works and new studies along the Giudicarie fault system Doglioni and Bosellini (1987), Castellarin et al. (2006) and Castellarin (2009) proposed a general reconstruction and chronology of the deformational events that affected the Southern Alps during the Alpine orogeny. They suggested that the CSA were involved in the Alpine tectonics already during the Cretaceous, with the activation of an E-W oriented foredeep, filled by thick turbidic sequences (Cretaceous flysch), south of the growing thrust-and-folds belt. During this fir phase of compression the CSA were separated from the

eastern sector of the Southern Alps by the activation of the NE-SW oriented Giudicarie faut system.
In the next paragraph the structural setting of the CSA wilt be described in detail.

1.3 Structural setting of the Central Southern Alps (CSA)

During the Alpine orogeny, the CSA experienced a polyphase evolution and severe shortening under low-grade to non-metamorphic conditions. Alpine deformations involved both the Variscan metamorphic basement exposed to the north, and the Permian to Cenozoic sedimentary cover preserved to the south

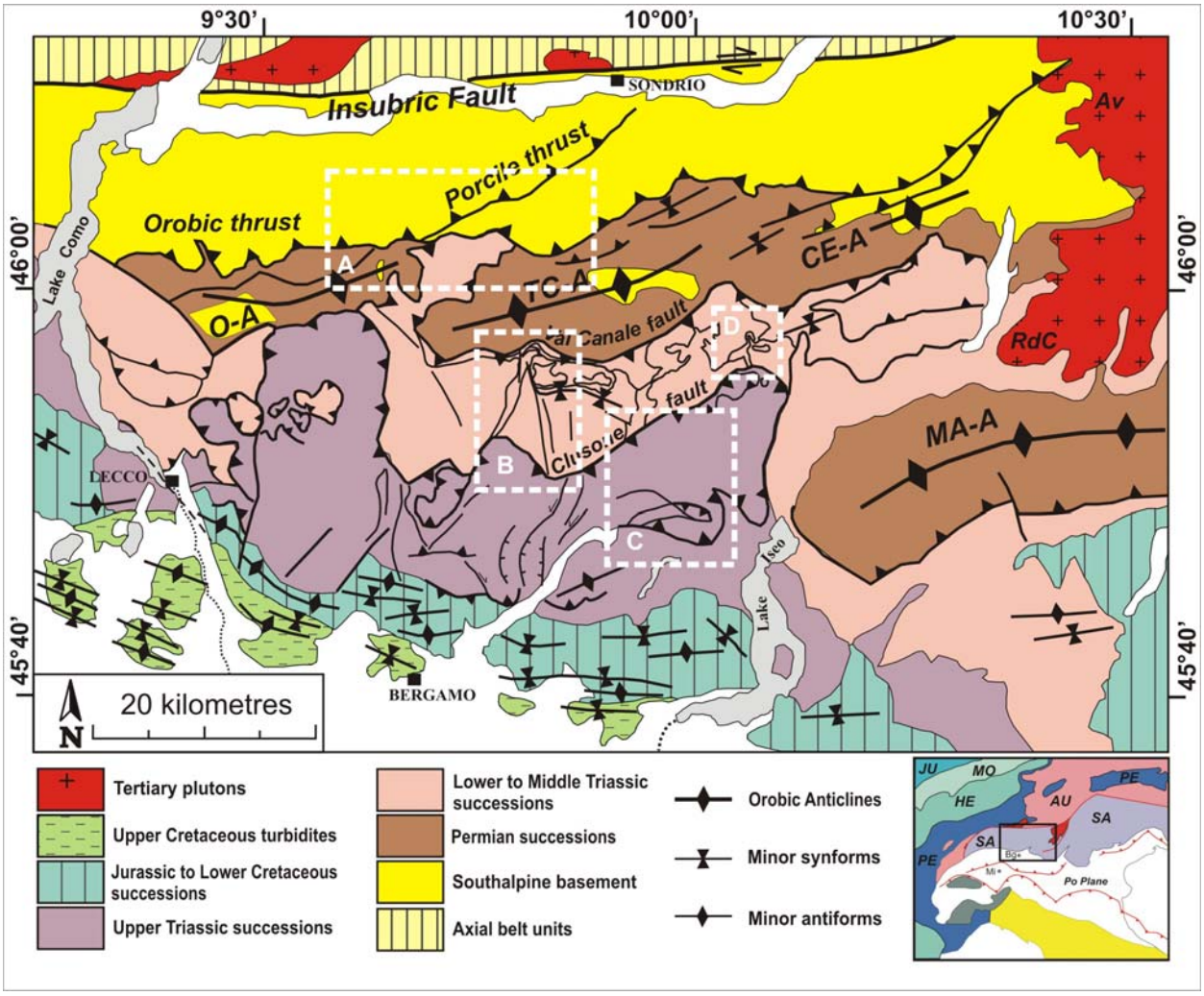

Fig. 1.3.1 Structural scheme of the CSA (Central Southern Alps, Italy), modified from D'Adda et al. 2010. *O-A*, Orobic Anticline; *TC-A*, Trabuchello-Cabianca Anticline; *CE-A*, Cedegolo Anticline; *MA-A*, Maniva Anticline; *RdC* (Re di Castello Unit) and *Av* (Avio Unit): Adamello batholith. Dashed rectangles indicate the locations of maps in Fig. 2 (Gandino area) and Fig. 8 (Presolana area). Bottom right: simplified scheme of the Alps. *SA*, Southern Alps; *AU*, Austroalpine domain, *PE*, Penninic domain; *HE*, Helvetic domain; *MO*, Molasse; *JU*, Jura belt.
Dashed boxes indicate the study areas of this work: A) San Marco Pass – Porcile Lakes area; B) Grem – Vedra Transverse Zone; C) Gandino – Sovere thrust system; D) Presolana antiformal stack.

(Schönborn 1992; Albini et al. 1995; Spalla and Gosso 1999). The base of the thrust wedge is marked by a major detachment surface, observed in boreholes and seismic sections, deepening from the Po Plain towards the Insubric Fault (Pieri and Groppi 1981; Schönborn 1992; Montrasio et al. 1994; Scrocca et al. 2003). The amount of shortening, the age of thrust sheet stacking and the correlation with deformation stages in the axial belt are still matters of debate. In general terms, two Alpine compressive stages were recognized, one pre-dating and one post-dating the emplacement of the Adamello batholith in the Late

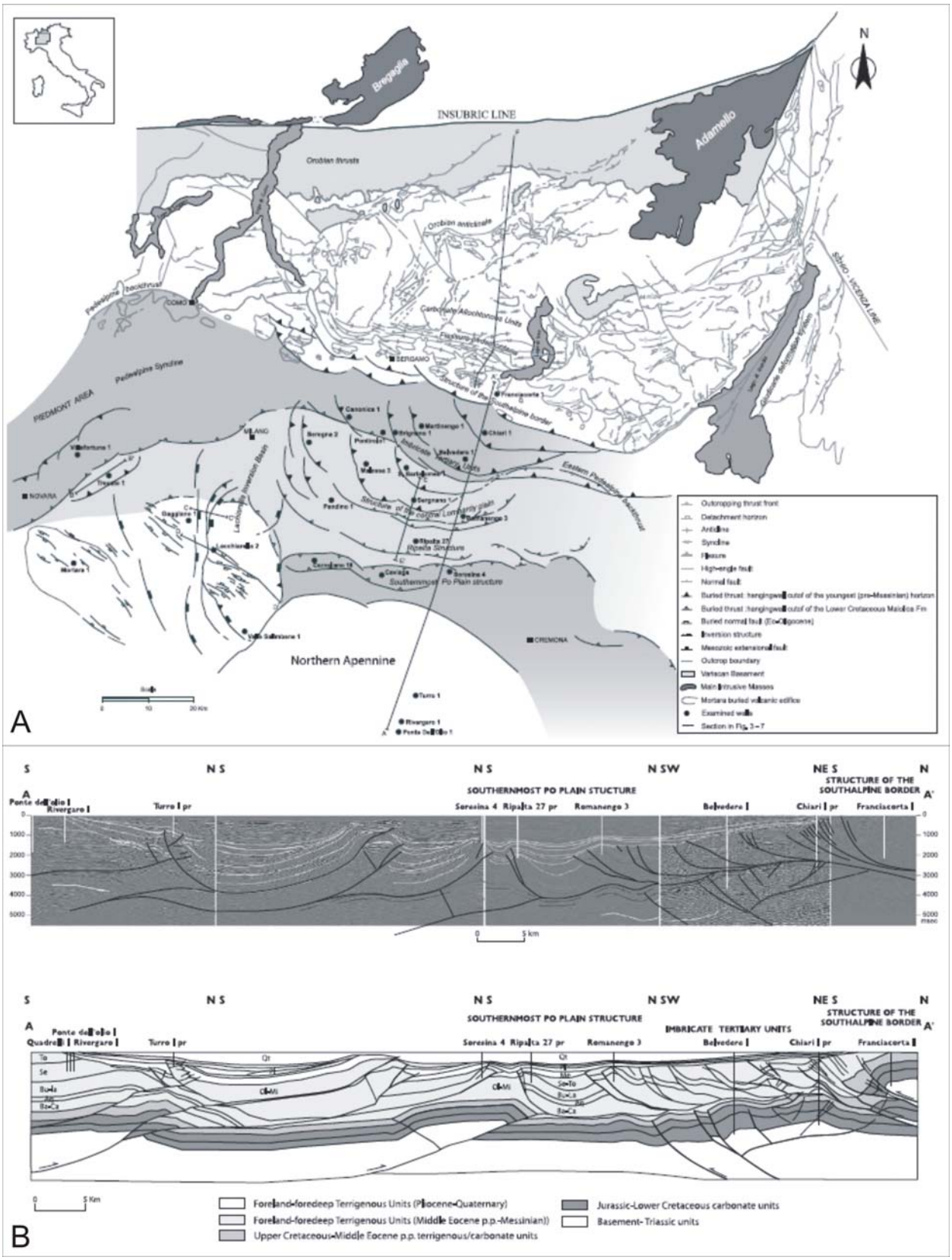

Fig. 1.3.2 (A) Structural scheme of the CSA and their foreland; (B) Seismic profile and relative geological section through the southern margin of the CSA and Po Plain foreland. (Modified from Fantoni et al. 2004)

Eocene-Early Oligocene (42-30 Ma) (Brack 1981; Del Moro et al. 1985; Schönborn 1992; Mayer et al. 2003). Cretaceous tectonics in the Eastern Alps and in their retro-belt is recorded by the thick clastic wedge of Upper Cretaceous siliciclastic turbidites, now involved in the southernmost part of the belt (Bernoulli and Winkler 1990; Bersezio et al. 1993; Castellarin et al. 2006). During Late Oligocene and Miocene, renewed compressions resulted in the formation of a younger foreland basin south of the growing Alpine orogenic wedge (Pieri and Groppi 1981; Gelati et al. 1991; Bersezio et al. 2001; Fantoni et al. 2004; Castellarin et al. 2006). In Middle-Late Miocene, thrusting was especially active along the frontal part of the CSA ("Milano Belt", Laubscher 1985), and involved the Oligo-Miocene Gonfolite clastic wedge fed from the growing Lepontine dome to the north (Gelati et al. 1991; Carrapa and Di Giulio 2001; Sciunnach and Tremolada 2004; Garzanti and Malusà 2008). Thrusts are generally sealed by the post-Messinian fill of the Po Plain (Pieri and Groppi 1981; Bersezio et al. 2001; Ravaglia et al. 2006). Reactivation of the frontal structures during Pliocene and Quaternary, also suggested by seismicity, has been locally described (Fantoni et al. 2004; Ravaglia et al. 2006).

Different structural levels can be recognized through the CSA. The deepest are exposed in the northern sector while the shallower are exposed to the south. A brief description of these levels is given below.

The Variscan crystalline basement of the Orobic Alps consists of micaschists and paragneisses with minor metagranitoids, amphibolites and marbles (Siletto et al. 1993; Spalla and Gosso 1999). Alpine metamorphism did not affect significantly the Variscan basement (Albini et al. 1994; Carminati et al. 1997), although it was involved in Alpine deformation (Cadel et al. 1996; Blom and Passchier 1997; Carminati and Siletto 1997, Carminati 2009). During the Alpine orogeny, the crystalline basement was thrust southward onto the Permian to Lower Triassic successions along the Orobic thrust (Fig 1.3.1), a complex N-dipping reverse fault that locally reactivated pre-existing Permian faults (Blom and Passchier 1997, Froitzheim et al. 2008). $^{40}Ar/^{39}Ar$ ages from pseudotachylyte veins (Meier 2003; Zanchetta et al. 2010) indicate that the Orobic thrust was already active in the Late Cretaceous.

South of the Orobic thrust three WSW-ENE regional anticlines with a dextral *en-échelon* arrangement, consisting of Permian - Triassic cover rocks cored by metamorphic basement, are exposed (Orobic Anticlines). They are the result of the southward propagation of a deep thrust surface developed in the footwall of the Orobic thrust. The easternmost one (Cedegolo Anticline, Fig. 1.3.1) is cut by the Adamello batholith which clearly post-dates the earliest Alpine folds and foliations in the country rocks (Callegari and Brack 2002).

The southern limbs of the Orobic Anticlines are marked by steeply south-dipping back thrusts (Valtorta - Val Canale system). Between the Valtorta – Val Canale system to the north and the Clusone fault to the south (Fig. 1.3.1), several S-verging thrust sheets are bounded by thrust surfaces that nucleated and propagated inside the Carniola di Bovegno (Olenekian). They form antiformal stacks, e.g. the Presolana stack, involving Anisian to Carnian carbonate dominated units (Forcella 1988; Zanchi et al. 1990). According to Laubscher (1985) and Schönborn (1992), the lower boundary of the uppermost thrust sheets exposed between the Valtorta – Val Canale and the Clusone faults would represent the prolongation of

the Orobic thrust to the south, and is thus referred to the earliest stages of Alpine tectonics. The southern portion of these imbricates is underthrust below the south-dipping Clusone fault, which forms a complex triangle zone related to the back-thrusting of the Upper Triassic units in its hanging wall (Zanchi et al. 1990a; Schönborn, 1992).

South of the Clusone fault, the Upper Triassic carbonate succession is doubled and stacked onto the Rhaetian to Palaeogene units of the Lombardian foothills (Berra et al. 1991).

These Rhaetian to Palaeogene units form an ESE-WNW alignment of folds and thrust structures. They are related to the Middle-Late Miocene emplacement of the youngest and most external part of the belt, called 'Milano Belt' (Laubscher 1985; Schönborn 1992), which is now deeply buried beneath the Plio-Quaternary Po basin fill (Fig 1.3.2).

1.4 Study areas

As shown in Fig. 1.3.1, four key areas, each of these representative of a precise structural level, have been investigated. They have been chosen following the occurrence of major structures (thrusts, faults, folds) or magmatic bodies with clear geometrical relationships with the main thrust sheets, useful for structural analysis and for the collection of samples suitable for isotope dating.

The northernmost area (area A, in Fig. 1.3.1) is located in the upper Brembana Valley, between the San Marco pass to the west, and the upper Cervia Valley to the east (see also Fig. 2.1.1 in chapter 2). In this area the crystalline basement is thrust southward onto the sedimentary cover along the Orobic thrust, which also join with the Porcile thrust.

The second area (area B) in located further south, between Val Canale and the lower Seriana Valley, comprising the southern limb of the Orobic Anticlines system (Val Canale fault) and the northern limit of the Upper Triassic units (Clusone fault). In this area the Lower to Middle Triassic sedimentary cover is interested by several thrust faults which form two main thrust stacks, separated from each other by a N-S directed transverse zone (Grem-Vedra Transverse Zone).

Between the middle Seriana Valley and the Iseo Lake (area C) two main thrust faults interest the Upper Triassic succession of the CSA. These thrusts are cut by mafic to intermediate dykes and hypabissal bodies emplaced following E-W trending minor normal faults.

In the upper Seriana Valley (area D) the Presolana massif is made of a large antiformal stack developed through the Lower to Middle Triassic units of the CSA. As in the case of Area C, the thrust pile is cut by E-W trending mafic to intermediate dykes, emplaced following local extensional stress fields.

In the following chapters a detailed description of the structural and geometrical features observed during field activity in these areas will be given.

Chapter 2

ALPINE DEFORMATIONS AND RELATIVE CHRONOLOGY IN THE CENTRAL SOUTHERN ALPS.
FIELD DATA AND STRUCTURAL ANALYSIS

2.1 Alpine deformations in the Orobic basement. Structural analysis along the Orobic and Porcile thrusts

2.1.1 Introduction

Understanding the deformation mechanisms along large-scale faults and thrusts zones is of fundamental significance in solving many tectonic problems such as modelling the evolution of a polyphase orogenic belt. The recognition of different structures in both the hangingwall and the footwall of regional thrusts and faults allows to define a relative chronology of compressive or extensional events that affected the belt during its growth. However, absolute age constraints are needed for a precise reconstruction of the deformational history. The study of the seismic history of the major faults over geological time could also be a useful tool to achieve this goal. The seismic history of active faults over recent geological time,

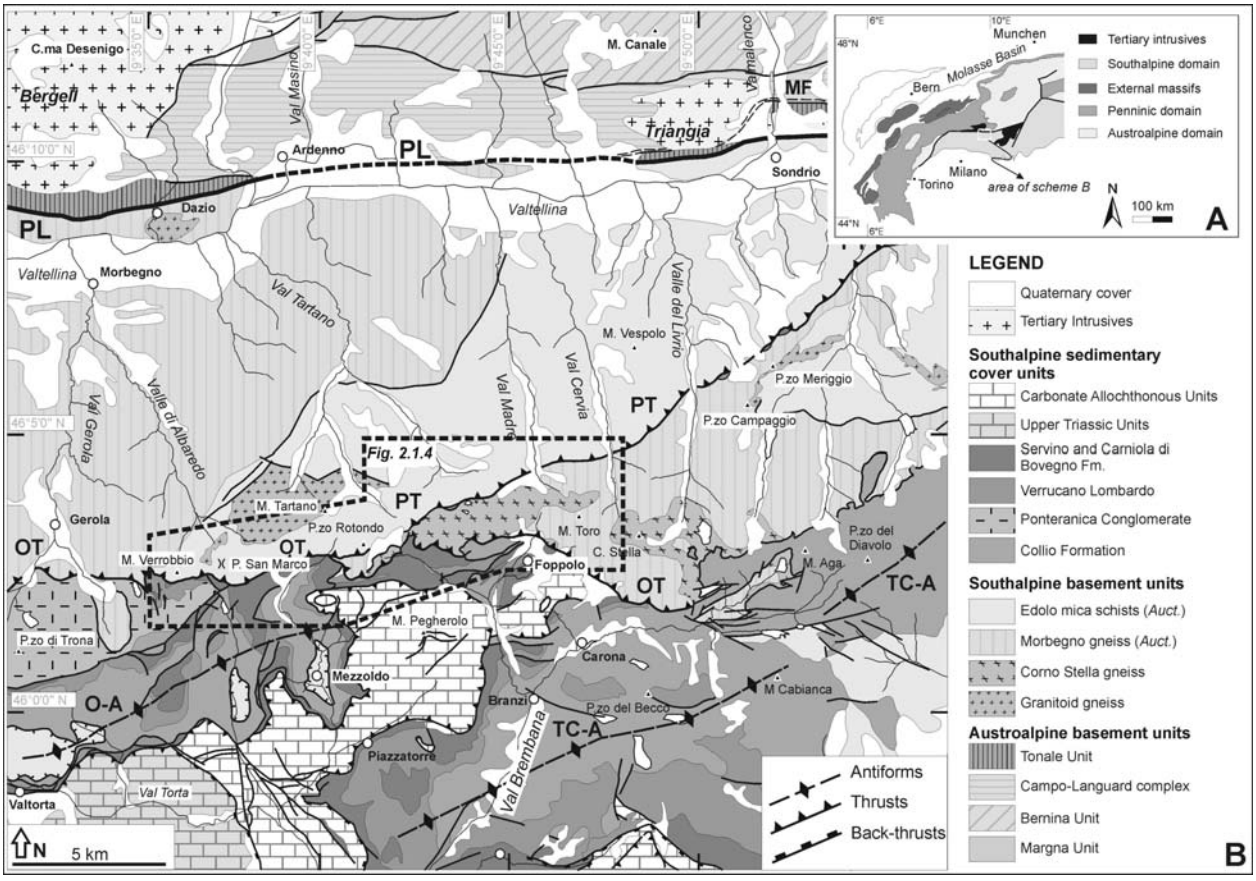

Fig. 2.1.1 Tectonic outline of the study area (Zanchetta et al. 2010). (A) Tectonic outline of the Western and Central Alps. (B) Geological sketch of the central Orobic Alps (Southalpine tectonic domain). The Orobic and Porcile thrusts are evident east of Passo San Marco where the South Alpine basement overrides the Permian-Mesozoic sedimentary cover along the Orobic and the Porcile thrusts represent an intra-basement brittle/ductile shear zone. The extent of the detailed geological map of Fig. 2.1.2 is highlighted. The geological sketch was drawn on the basis of existing maps (Casati et al. 1987; Forcella and Jadoul 2000) and original field work by the authors. OT: Orobic Thrust; PT: Porcile Thrust; PL: Periadriatic Lineament; MF: Mortirolo Fault; O-A: Orobic Anticline; TC-A: Trabuchello-Cà Bianca Anticline.

generally during the Late Pleistocene and Holocene, can be understood with the help of trenching surveys. However, reconstructing the earlier seismic history and rupture processes of long-lived active faults requires a different approach.

Fault rocks commonly provide primary evidence of the faulting history and deformation process of seismic slip at all depths from the near-surface to deep levels in the crust. Fault rocks that form at

relatively deep levels, even in the lower crust, are eventually uplifted by crustal movements and exhumed by erosion. It is therefore possible to gain an insight into the formation processes of fault rocks by studying the structures, textures, physical properties and chemical compositions of fault-related rocks exposed at the surface.

In the northern sector of the CSA the metamorphic pre-Alpine basement is thrust southward on the Permian-Mesozoic cover along a composite thrust surface, named Orobic thrust. It roughly trends E-W with a N-dipping plane and cut an important intra-basement structure, the Porcile thrust (Fig 2.1.1). The Porcile thrust trends NE-SW with an high-angle, N-dipping surface, and is marked by the occurrence of thin slices of the Permo-Triassic cover and Pre-Alpine metagranitoids, pinched along the fault zone. The reconstruction of the relative chronology of the deformational events that interested these fault zones during the growth of the Orobic belt was carried out through detailed field mapping and structural analysis of cleavage, folds and faults. To pose absolute time constraints to the reconstructed structural evolution we used $^{40}Ar/^{39}Ar$ dating of fault-related pseudotachylytes. In the case of low- to non-metamorphic orogenic belts, the isotope dating of syntectonic recrystallised minerals is not applicable, otherwise dating of pseudotachylyte veins is a powerful method to constrain the age of fault activity (Kelley and Spray 1997; Müller et al. 2002) since it allows to directly date deformation not associated to metamorphism. Moreover, overprinting criteria between plastic or brittle fabrics and pseudotachylyte veins can be used to define maximum/minimum age for the transition from ductile to brittle regime (Williams et al. 1994; Carminati et al. 1997).

This chapter provides a reconstruction of the tectonic evolution of the Orobic and Porcile thrusts and adjacent basement and Permo-Mesozoic cover.

A complete description of textural and petrographical characters of analyzed pseudotachylytes is also provided.

$^{40}Ar/^{39}Ar$ data obtained on pseudotachylytes are described in chapter 3.

2.1.2 Geological & structural map of the Orobic thrust – Porcile thrust triple junction (*Plate 1*)

The geological-structural map of *Plate 1* has been realized by original field mapping at the scale of 1:5000 and then reduced to 1:10000.

The mapped area is located in Lombardy (northern Italy), in the northernmost sector of the Bergamo province, at the boundary with the Sondrio province, and extends for about 5 kilometres from the San Marco pass (to the West) to the San Simone pass (to the East).

The chosen area is located along the E-W trending tectonic boundary between the crystalline basement of the CSA and its sedimentary cover (Orobic thrust) and comprises the triple junction of this main structure with the intra-basement Porcile thrust. Field mapping has been characterized by a detailed structural analysis (discussed in the next paragraph), aimed to understanding the relationships between these two main thrusts and to the reconstruction of the deformations induced by them in both basement and

sedimentary cover during the Alpine orogeny. A brief description of the main lithothypes cropping out in the area will be given below.

Lithologies of the crystalline basement

Micaschists (Scisti di Edolo, Auct.)

This lithotype is the most common within the mapped area and constitutes most of the outcropping crystalline basement. It is represented by fine to medium grained micaschists, gray to dark-gray in outcrop, with a typical mineralogical association made of muscovite, quartz, plagioclase, biotite and minor garnet and staurolite. Garnet and biotite are partially replaced by chlorite indicating retrograde metamorphism.

A pervasive schistosity (S2) is the typical character and is defined by the shape preferred orientation of phyllosilicates. Fine grained phyllonites are common, especially approaching thrust fault zones. They are usually dark coloured and often interested by retrograde metamorphism as testified by the occurrence of abundant chlorite replacing other mineralogical phases.

The occurrence of quartz lenses is also a common feature. Lenses are characterized by highly variable sizes and are usually elongated parallel to the main foliation. Moreover, grey to light-gray quartzitic layers are quite frequently observable. They are characterized by thin quartz layers alternated with layers of phyllosilicates producing a marked foliation.

Two-mica gneiss

In the study area they crop out only north of Cima dei Siltri, in the tectonic slice comprised between the Orobic and Porcile thrusts, especially near the Porcile thrust fault-zone.

They are represented by medium grained paragneiss with quartz, plagioclase, biotite, muscovite and minor garnet and chlorite.

They are always interleaved with micaschists displaying transitional contacts with them. Quartz lenses and quartzitic layers are generally absent.

Leucocratic gneiss (Gneiss Chiari del Corno Stella, Auct.)

These rocks form elongated bodies along the Porcile fault and occur also along a secondary plane related with the Orobic Thrust, NE of Cima dei Siltri.

They are represented by medium to coarse grained ortogneiss, white to light-gray in outcrop, with a typical mineralogical association of quartz, albite, plagioclase, muscovite, biotite, minor chlorite and rare crystals of tourmaline.

The lithotype is characterized by a metamorphic S2 foliation marked by the preferred orientation of white mica along preferential schistosity planes, usually alternated with common millimetric to centimetric porphyroclasts of K-feldspar. However, as in the mapped area these rocks crop out only within the Porcile thrust fault-zone, their textural characters are almost completely overprinted by cataclastic deformation.

Granitoid gneiss (Ortogneiss del Monte Fioraro, Auct.)

This lithotype crops out in the north-western sector of the map (Mt. Fioraro massif), forming an old intrusive body of Ordovician age metamorphosed during the Varisican orogeny (Bergomi et al. 2004).

It is represented by granitoid gneiss with K-feldspar eye-shaped porphyroclasts. His typical mineralogy is given by K-feldspar, quartz, plagioclase, muscovite, biotite, with minor garnet, titanite and chlorite.

The regional foliation (S2) is defined by isoorientation of phyllosilicates and K-feldspar porphyroclasts and is locally crenulated and folded by D3. The contacts with micaschists are folded by D3 N-dipping folds and are characterized by the occurrence of various-sized xenolites of micaschsits.

Amphibolites

These rocks crops out only in a two-meters large, E-W oriented lenses, north of Cima dei Siltri. They are characterized by a mineralogical association given by amphibole, plagioclase, minor quartz, garnet, biotite and chlorite.

The S2 foliation is defined by compositional layering or by shape preferred orientation of amphibole, although it is not well recognizable since it is partially overprinted by cataclastic deformation.

Pre-Alpine dykes

These bodies crops out in the north-western sector of the map, mainly within the margins of the Mt. Fioraro metagranitoid complex. They roughly trend E-W with sharp contacts with country rocks and are folded by D3 structures, suggesting that they are of pre-Alpine age.

They are composed by dark coloured and very fine grained porphyrites, with plagioclase, biotite, amphibole and minor quartz. A slight S2 foliation is observable where an isoorientation of amphibole and biotite occur.

Lithologies of the sedimentary cover

Basal Conglomerate

These dark green to grey breccias and sandstones derived from the erosion of the metamorphic south-alpine basement and are of Early Permian age. They crop out in the south-eastern sector of the map, north of San Simone pass.

Clasts are millimetric to centimetric and consist of quarzites, metapelites and minor metagranitoids. The original bedding is not recognizable in the area since a N-dipping cataclastic foliation, related with the polyphasic activity of the Orobic thrust, strongly overprint the original texture.

Cabianca Volcanite (Collio vulcanico, Auct.)

Red to brown volcanic and volcaniclastic deposits, with minor alternating sandstone and siltstones. Within the mapped area they crop out only in a small sector east of Rifugio Madonna delle Nevi.

They represent the stratigraphically lowest part of a volcanic and volcanoclastic formation of Early

Permian age, known in literature as "Collio Formation". They are the result of a widespread calcalcaline magmatism and transtensional tectonics that led to the development of fault-controlled troughs filled by continental deposits.

Verrucano Lombardo

The typical lithotype of this unit is represented by red to brown continental conglomerates and breccias with lenses of red sandstones and pelites. Clasts are millimetric to centimetric and consist of quartz, red volcanites and volcanoclastites and minor metapelites.

They were deposited during Late Permian and derived from the erosion of the Early Permian volcanics ("Collio Formation", Auct.) and metamorphic basement of the Southern Alps.

The unit crops out in the south-eastern sector of the mapped area. East of Rifugio Madonna delle Nevi the stratigraphic contact with the Cabianca Volcanite unit is partially preserved and poorly deformed. On the contrary, north of the San Simone pass the unit is involved by high angle fault systems related with thrusting along the Orobic thrust.

Servino

This unit of Induan-Olenekian age is mainly composed by well bedded quartz sandstones with green to light green pelites and minor yellow to green marls. It crops out in the southern sector of the map, in the footwall of the Orobic thrust.

Bedding is often involved in E-W trending folds, and cataclastic layers are common near the tectonic boundary with the overthrusted metamorphic basement.

Carniola di Bovegno

Yellow vacuolar dolomitic limestones and dolostones with lenses of grey to green marls and clay. This rocks of Olenekian-Anisian age are usually localized along tectonic contacts and are interested by a N-dipping cataclastic foliation. In the southern sector of the map the occurrence of *carniòules* within the Servino unit suggest tectonic repetitions with a southward direction of transport.

2.1.3 Cleavage, fold and fault analyses

In the study areas a poly-metamorphic basement consisting of metapelites, paragneiss and acidic metaintrusive gneisses is thrust over the Lower Permian – to earliest Triassic succession of the

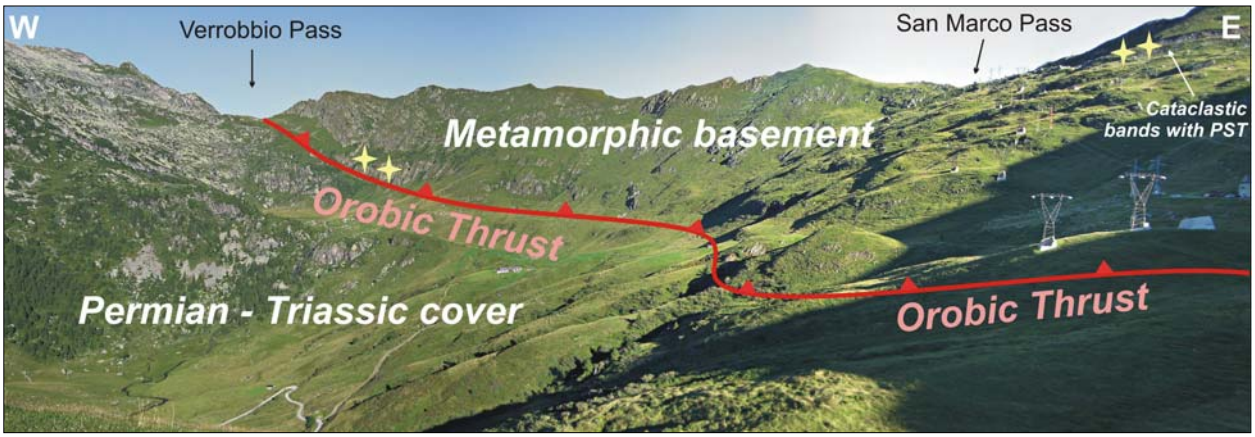

Fig. 2.1.2 Panoramic view of the Verobbio Pass – San Marco Pass area. Yellow stars indicate the location of sampled pseudotacylyte veins.

sedimentary cover of the CSA along the Orobic thrust (Fig 2.1.2).

Another important structure that interests the metamorphic basement is represented by the Porcile thrust (Fig. 2.1.3), which is cut by the Orobic thrust 2 km WNW of Cima dei Siltri (see geological map in Plate 1). West of this point the Orobic thrust trends E-W and stacks micaschists and gneisses ("Scisti di Edolo"

Fig 2.1.3 The Porcile thrust in the Porcile Lakes area, seen from the Verrobbio Pass. Yellow stars indicate the location of sampled Pst veins.

Auct.) over the Servino Fm. and the Upper Permian Verrucano Lombardo.

The Porcile thrust is generally steeper than the Orobic thrust and trends ENE. The basement unit between these two faults consists of biotite - white mica gneisses and mica schists ("Gneiss di Morbegno" Auct.) with minor leucocratic gneisses ("Gneiss Chiari del Corno Stella" Auct.). The Porcile thrust is marked by the occurrence, along the fault zone, of tectonic slices derived from Servino and Verrucano Lombardo, locally associated to thin layers (up to 7-8 m) of Carniola di Bovegno (Fig. 2.1.3 and Fig. 2.1.4). In the Laghi di Porcile area (Fig. 2.1.3) the fault zone is also marked by meter-thick quartz veins containing distinctive Fe deposits.

A polyphase history can be observed within the metamorphic basement which displays at least three deformation phases. D1 structures consist of relict small rootless folds within the regional foliation, and have been mainly observed within quartz-rich lithologies. The S1 foliation is rarely preserved within granitoid gneisses where is marked by shape-preferred-orientation of biotite and minor white mica. On the base of the mineralogical assemblages amphibolite-facies conditions have been suggested for the syn-D1 metamorphic event (Spalla et al. 1999; Cadel et al. 1996; Carminati and Siletto 2005).

The S2 foliation dips to N-NW with dip angles ranging between 35° and 70°. Its development is generally assumed to be Variscan in age (Cadel et al. 1996; Spalla et al. 1999) and corresponds to a diffused

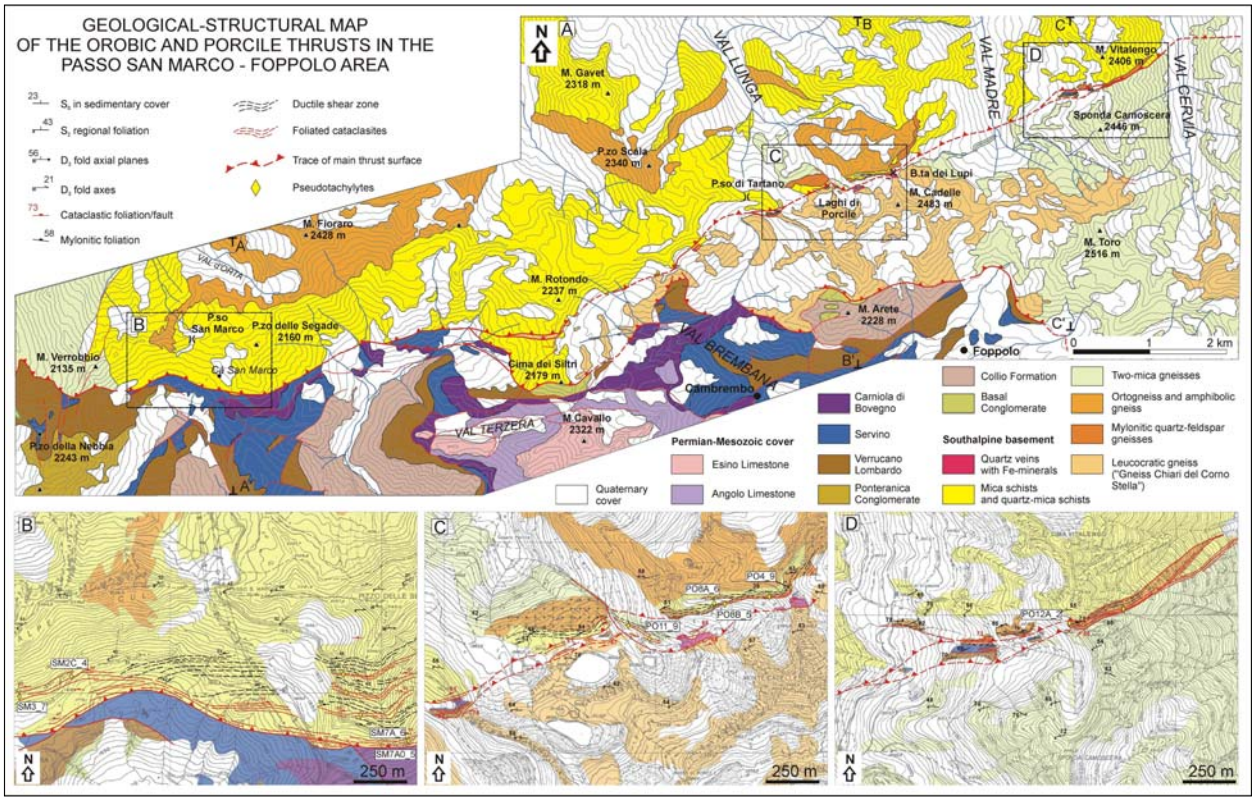

Fig. 2.1.4 Geological-structural maps of the study area (Zanchetta et al. 2010). *A*) Geological-structural map of the Orobic and Porcile thrusts close to the San Marco Pass (BG, Italy). The three insets (*C*, *D* and *E*) show in details the location of the studied pseudotachylyte samples and the structural pattern along the analysed thrust segments.

retrogression at greenschists-facies conditions. This pervasive foliation characterizes the meso- and microfabric of all basement lithotypes and is marked by the shape-preferred-orientaion of chlorite, white mica and minor biotite. The transposition of the igneous contacts of the meta-intrusives bodies of

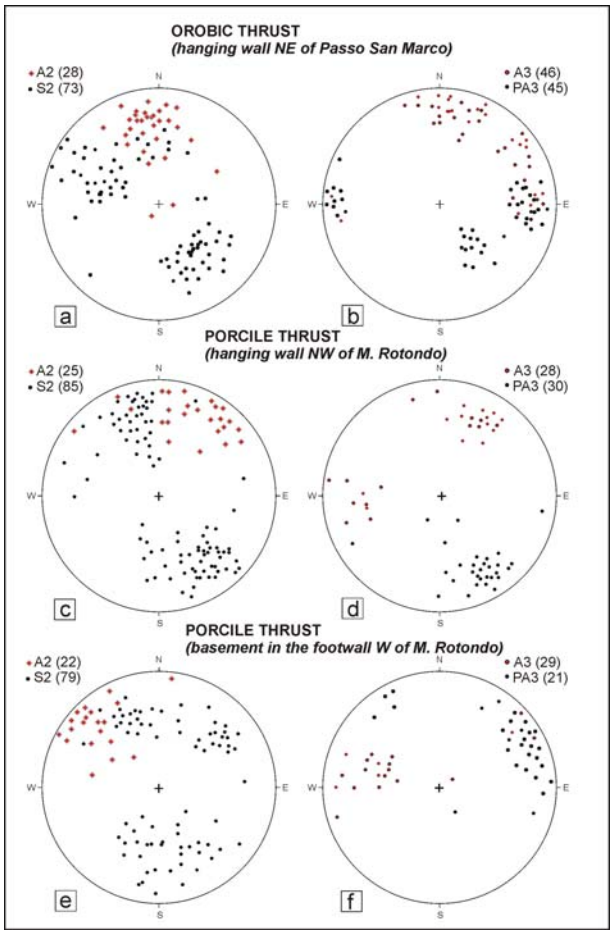

Fig. 2.1.5 Structural data of fold elements in the basement (Zanchetta et al. 2010). Equal area, lower hemisphere stereographic projections of structural data referred to the South Alpine basement in the hanging wall of the Orobic thrust and along the Porcile thrust (see text for comments).

Ordovician age occurring in the area (Siletto 1990; Bergomi 2004) suggests a Variscan age for both D1 and D2 deformation phases and associated metamorphism.

The age and the extent of the D3 deformation phase in the crystalline basement is not yet completely understood (Carminati and Siletto 2005; Spalla et al. 1999). Our field structural analyses highlighted that D3 open to medium-tight folds interfere with pre-existing D1 and D2 structures without the development of an axial plane schistosity (Fig. 2.1.5). Within mica-rich lithologies a millimetre-scale crenulation accompanies the development of D3 folds. W of Cima dei Siltri, in the hanging wall of the Orobic and Porcile thrust (Fig 2.1.4 and geological map in Plate 1), D3 fold axes dip from N to NW with dip angles ranging from of 20°-35° to 55-70°. D3 fold axes are steeper toward W, where they strongly affect the contact between metapelites and the meta-intrusive body that crops out in the Mt. Fioraro area (Gneiss del Monte Fioraro, Auct.). Toward the E they are characterized by less dipping axes and in the footwall of the Porcile thrust and are rotated plunging gently eastward. The Alpine age of the D3 deformation phase in the basement was postulated by Carminati and Siletto (2005) on the base of fold geometry and similarities with the deformation pattern developed in the adjacent cover, but it is still not well constrained. Continuous outcrops along the road south of San Marco Pass allow a detailed study of the geometrical relationships between D2 and D3 structures and the fault zone of the Orobic thrust. Approaching to the fault zone, D3 folds progressively rotate becoming parallel to the greenschists-facies mylonitic foliation developed in the upper part of the fault zone. The re-orientation of pre-existing D3 fold axes suggests that the first stages of the ductile evolution of the Orobic thrust postdate D3 deformation.

The greenschists-facies mylonitic foliation dips N to NNW with dip angles close to 45° (Fig. 2.1.6) and is only locally preserved within the fault zone, as brittle structures strongly overprint the pre-existing fabric. The mylonitic foliation is in fact cross-cut by steeper, dark-coloured cataclastic shear zones. A loosely constrained reverse shear sense is determined from s-c and s-c' structures, observed within the mylonitic shear zone. Several fault planes occurring within cataclastic bands have been measured along the Orobic thrust in the San Marco pass and San Simone pass areas (Fig 2.1.6 and Fig. 2.1.7). Rose diagrams relative to reverse faults show a preferential ENE-WSW trend with a northward dip ranging

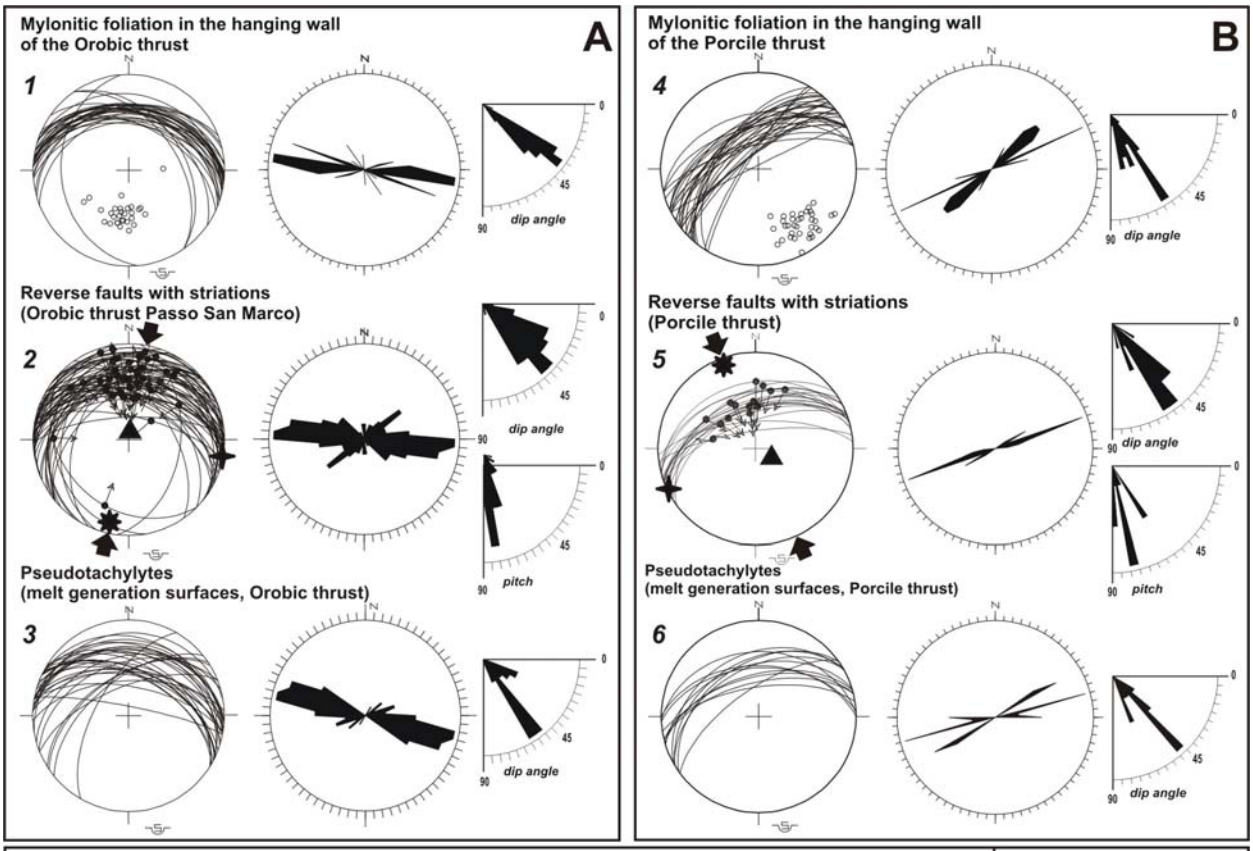

Site	Method	N° of data	σ_1	σ_2	σ_3	Ratio	ANG		RUP	
			plunge/dip	plunge/dip	plunge/dip	φ	av(°)	M(°)	av(%)	M(%)
2	I	42	187/15	97/1	gen-75	0,686	11	28	27	48
5	I	18	345/8	254/3	142/82	0,7	10	26	28	48

Fig. 2.1.6 *A*) Structural data of the Orobic thrust fault zone. Equal area, lower hemisphere stereographic projections of mylonitic foliation, reverse faults and pseudotachylyte fault veins along the Orobic thrust. Reverse dip-slip faults dip 5° to 10° steeper than the pre-existing greenschists mylonitic foliation. Pseudotachylyte fault veins display coherent geometries with the measured reverse faults and allow a direct association of friction-induced melting to reverse movements along the Orobic thrust.. *B*) Structural data of the Porcile thrust fault zone. Equal area, lower hemisphere stereographic projections of mylonitic foliation, reverse faults and pseudotachylyte fault veins along the Porcile Thrust in the study area. The greenschist facies mylonitic foliation results here steeper than subsequent reverse faults and associated pseudotachylyte veins. (Modified from Zanchetta et al. 2010).
The following indications are reported in table: number of site; inversion method: I (INVD), R (R4DT); number of data used for tensor calculation; plunge/dip of the main stress axes σ1, σ2, σ3 (σ1>σ2>σ3); ratio φ: (σ2-σ3)/(σ1-σ3); average value av (°) and maximum value M(°) of ANG; average value av(%) and maximum value M(%) of RUP for solutions obtained with INVD;. Numerical solutions have been accepted for average and maximum value of ANG respectively lower than 10-12° and 24-28°, and average and maximum value of RUP respectively lower than 35 and 55.

between 20° and 60°, due to the occurrence of secondary R shears. Striations along the measured fault surfaces mainly indicate different stages of dip-slip motions and minor strike slip reactivations in a N-S directed compressive regime. Near the San Marco pass melt generation surfaces (*mgs*) of pseudotachylyte veins show very similar geometrical features with a medium-angle dip (50°-60°), suggesting that the genesis of pseudotachylytes is directly related to the main brittle stage of thrust propagation (Fig. 2.1.6). Along the San Marco pass road and near the San Simone pass a successive deformation phase was observed. Discrete brittle shear planes cross-cut mylonitic foliation, cataclastic bands and pseudotachylyte veins (SP1 and SP2 in Fig.2.1.7 and Fig. 2.1.8). Both SP1 and SP2 display a reverse kinematics inferred from centimetre-scale drag folds and offset of pre-existing fabric elements.

The Porcile thrust shows a similar structural evolution. Greenschists-facies mylonites are overprinted by

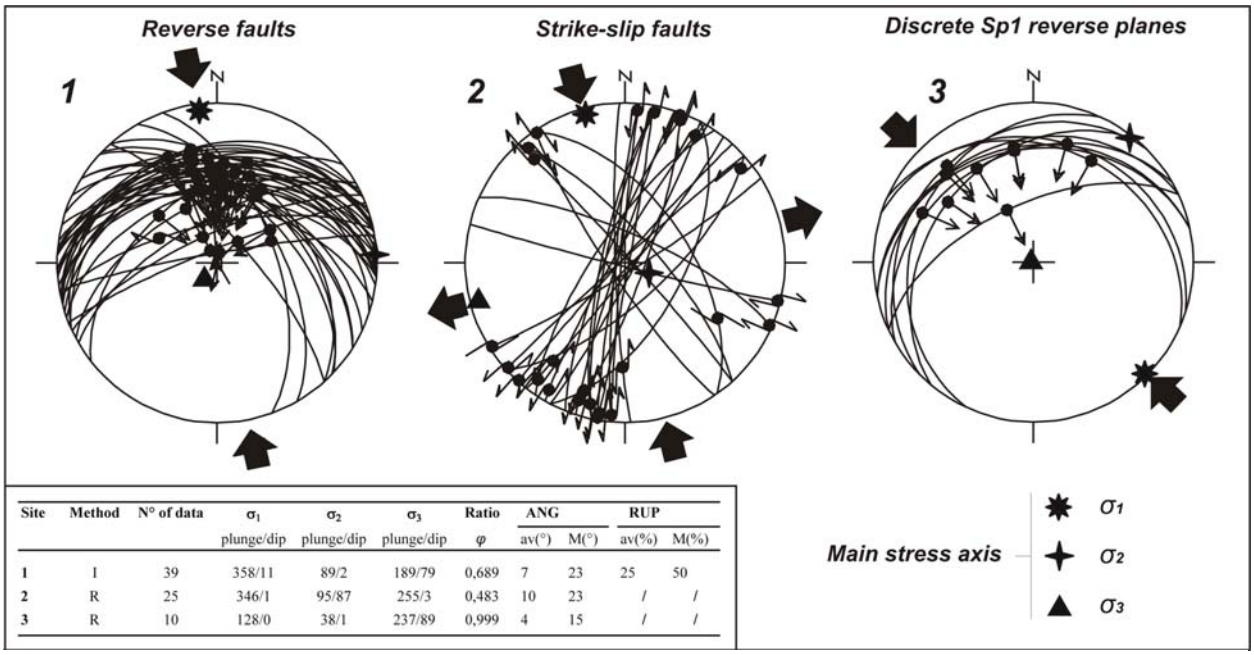

Site	Method	N° of data	σ_1	σ_2	σ_3	Ratio	ANG		RUP	
			plunge/dip	plunge/dip	plunge/dip	φ	av(°)	M(°)	av(%)	M(%)
1	I	39	358/11	89/2	189/79	0,689	7	23	25	50
2	R	25	346/1	95/87	255/3	0,483	10	23	/	/
3	R	10	128/0	38/1	237/89	0,999	4	15	/	/

Fig 2.1.7 Different faults populations measured along the Orobic thrust near the San Simone pass (see geological map in Plate 1) highlighting that the fault zone was interested by distinct compressive events. The following indications are reported: number of site; inversion method: I (INVD), R (R4DT); number of data used for tensor calculation; plunge/dip of the main stress axes σ1, σ2, σ3 (σ1>σ2>σ3); ratio φ: (σ2-σ3)/(σ1-σ3); average value av (°) and maximum value M(°) of ANG; average value av(%) and maximum value M(%) of RUP for solutions obtained with INVD;. Numerical solutions have been accepted for average and maximum value of ANG respectively lower than 10-12° and 22-24°, and average and maximum value of RUP respectively lower than 35 and 55.

cataclastic bands with pseudotachylyte veins, suggesting an earlier ductile stage followed by a transition to brittle conditions. The mylonitic foliation dips to NW with a mean dip angle of 55°-60° (Fig. 2.1.6), considerably steeper with the mylonitic foliation that occurs along the Orobic thrust. Along the contacts between the cover tectonic slices and the mica schist forming the hanging wall of the fault zone, the formation of cataclasites (1 to 20 m thick) indicates the transition to the brittle regime. Measured fault planes dip NNW, with a 10° to 15° clockwise rotation with respect to mylonites. Kinematic indicators along the brittle fault zone point to a mainly dip-slip motion, with a reverse sense accompanied by a minor left-lateral component. Pseudotachylyte veins occur within cataclasites along dip-slip reverse faults (Fig. 2.1.6) and are of both *mgs* and injection type. Their occurrence suggests that paleoseismic faulting activity was closely related to pure thrusting along the Porcile thrust. Post-thrusting deformation resulted in left- and right-lateral strike-slip faults that reactivated some of the main thrust surfaces, pointing to a complex evolution through the entire Alpine history of the Porcile thrust. The Permian to Lower Triassic cover succession forming the footwall of the Orobic thrust shows open to medium-tight, E-W trending folds with a metre-scale wavelength, well developed in the terrigenous succession of Servino. In fine-grained sandstones and siltstones an axial plane pressure-solution cleavage locally occurs. Fold axial planes and cleavage dip N to NW with dip angles ranging between 40° and 55° (Fig.

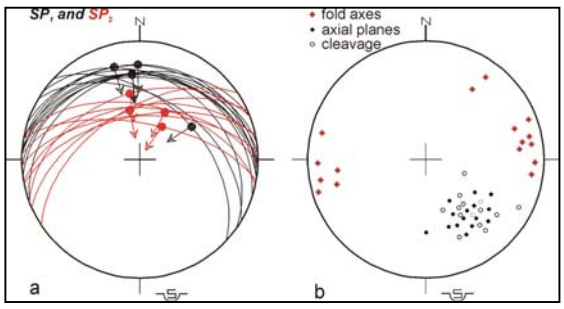

Fig. 2.1.8 Structural data in the sedimentary cover (Zanchetta et al. 2010). Equal area, lower hemisphere stereographic projections of fold axes, axial planes and cleavage data in the sedimentary cover cropping out in the footwall of the Orobic and Porcile thrusts. Data on shear planes (SP_1 and SP_2) postdating pseudotachylytes are also reported.

2.1.8), resulting subparallel to the Orobic thrust surface. The geometric features of folds and cleavage suggest close relationships between thrusting and folding in the sedimentary cover.

2.1.4 Pseudotachylytes along the Orobic and Porcile thrusts: fabric and petrography

Pseudotachylytes represent a fundamental tool in reconstructing the deformational history of a long-lived fault zone. These peculiar rocks are products of wear, comminution and friction-induced melting during seismic slip along a shear zone (Sibson 1975; Magloughlin and Spray 1992; Swanson 1992). They may

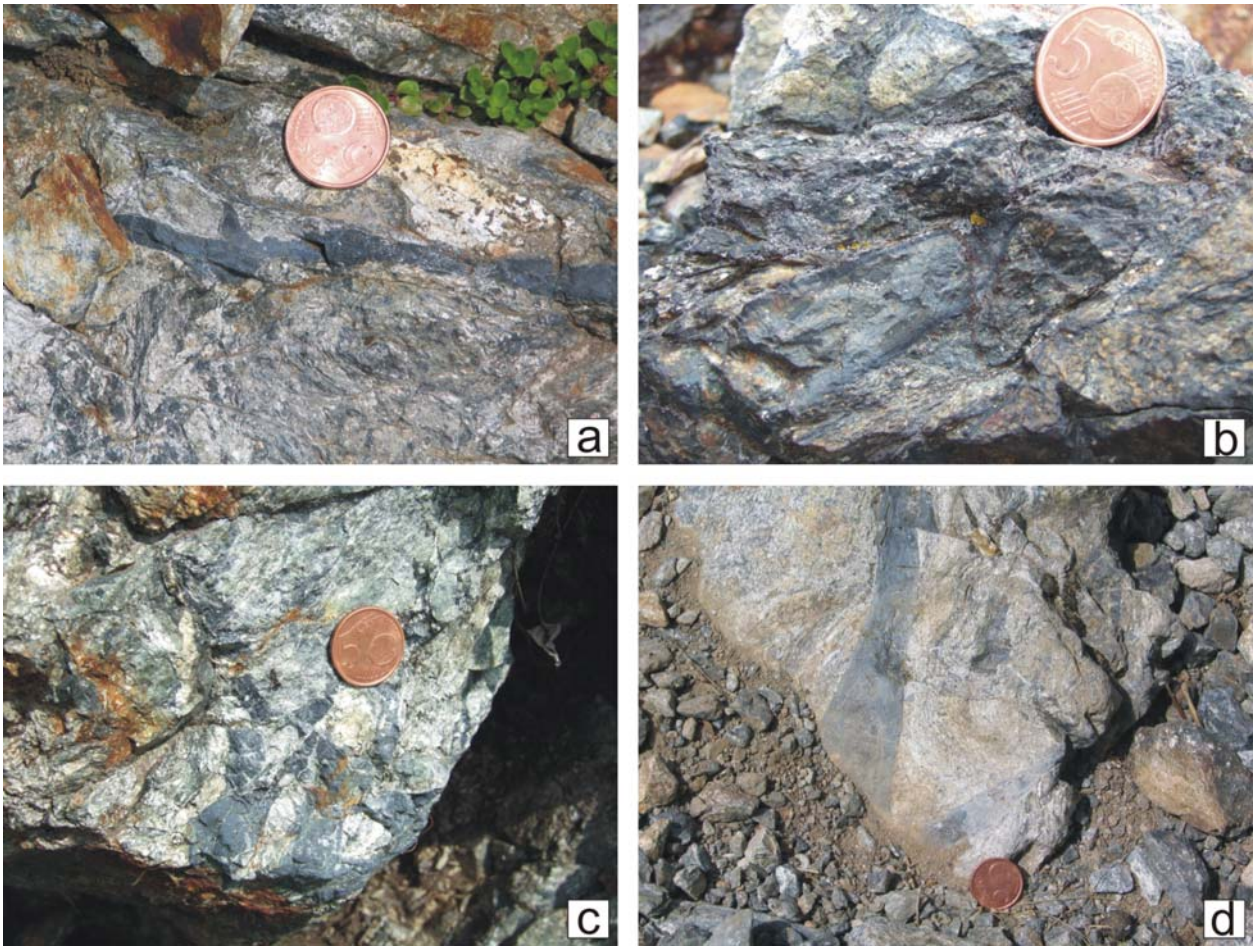

Fig. 2.1.9 Field photographs of pseudotachylyte veins (Zanchetta et al. 2010). *A*) Pseudotachylyte vein within two mica gneisses along the Orobic thrust (near the Verrobbio Pass). It consists of a fault-vein with sharp but undulate contacts with the host rock and minor reservoir/injection veins. Coin diameter in all figures is 20 mm. *B*) Symmetrically zoned pseudotachylyte fault vein with clast laden black rims (1-2 mm thick) and a central, lighter coloured part with minor clasts. *C*) Cataclasites overprinting pre-existing pseudotachylyte veins. *D*) Large pseudotachylyte injection vein within K-feldspar gneisses along the Porcile thrust

be potentially used to constrain fault plane processing during earthquakes in exhumed paleoseismic faults as their glassy or cryptocrystalline matrix can be isotopically dated ($^{40}Ar/^{39}Ar$). However, pseudotachylytes dating is complicated by their very fine-nature and by the common presence of devitrified and recrystallized material and rock fragments. This make it fundamental a petrographical and textural characterization of dated materials from selected pseudotahylyte veins. The pseudotachylyte (pst) veins occurring along the Orobic and Porcile thrusts (Fig. 2.1.9) discontinuously decorate fault planes and typically display thickness from few millimetres to 20-25 mm, with rare reservoir (or injection *sensu*,

Sibson 1975) veins reaching 70-80 mm along the Porcile thrust, east of Porcile Lakes. They are found inside different lithologies, two- mica gneiss, mica schists and K-feldspar gneiss (Porcile Lakes area). The host rocks usually display a cataclastic/ultracataclastic fabric and only in a few cases pseudotachylytes are found inside greenschists-facies mylonites. Pseudotachylyte veins display only minor reactivations along a successive set of discrete brittle shear planes (SP1 and SP2) almost parallel to the main reverse fault planes. Dilatational epidote-chlorite veins, 1-5 mm thick, locally crosscut all the previous thrust-related structures. The white mica + chlorite greenschists-facies mylonitic foliation is always post-dated by cataclastic bands related to the brittle evolution of the Orobic and Porcile thrusts.

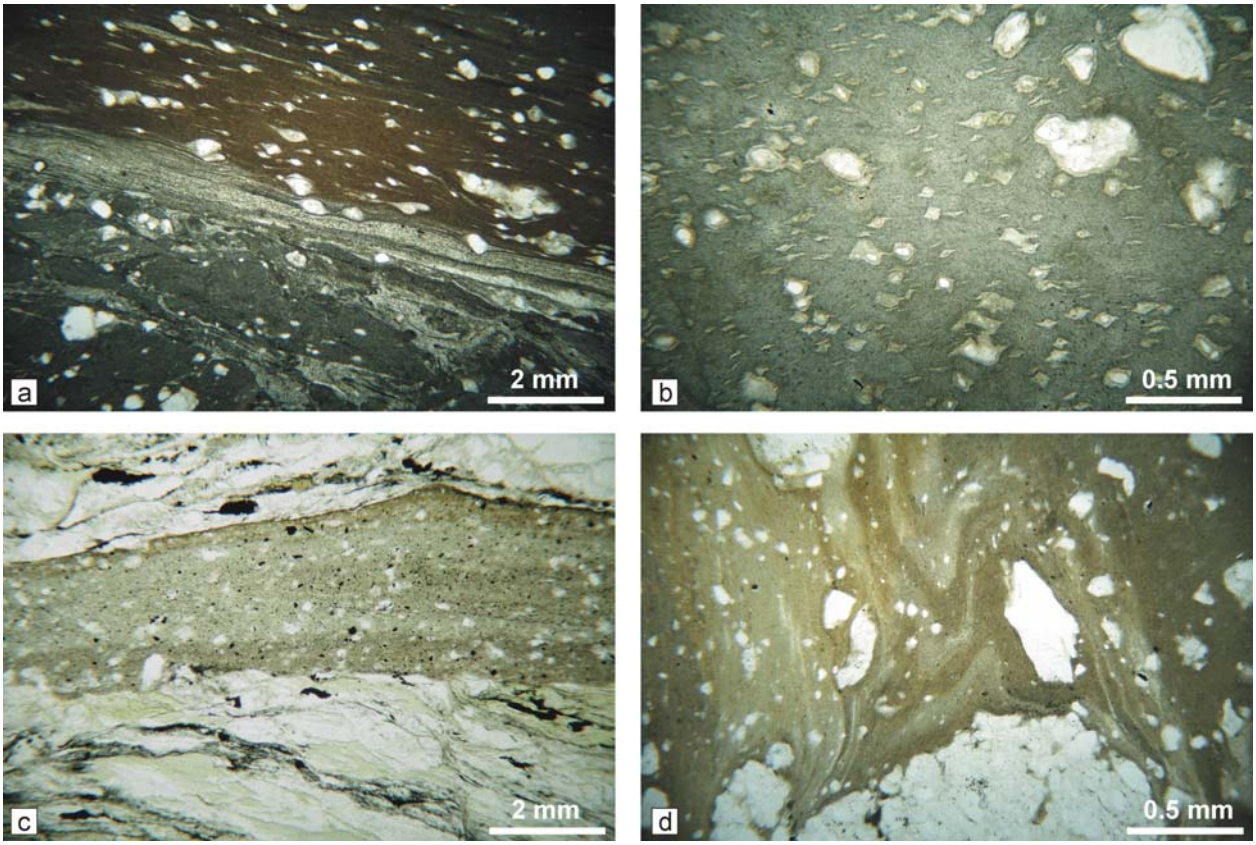

Fig. 2.1.10 Optical microscope images of pseudotachylyte microfabric, all images at parallel nicols (Zanchetta et al. 2010). *A*) two generation of pseudotachylytes. The first one (on the left-bottom part of the image) has a darker colour and isotropic fabric. The second pseudotachylyte vein displays flow structures. The light rim between the two veins belongs to the second pseudotachylyte as well as the light areas within the first generation vein. Such areas are made of melt intruded in the pre-existing fractured pseudotachylyte as confirmed by EMP analyses (sample SM2C). *B*) inherited quartz clasts within cryptocrystalline pseudotachylyte matrix. Pristine biotite preferentially crystallised in haloes around clasts (sample PO11). *C*) clast laden pseudotachylyte vein cross-cutting chlorite + white mica mylonitic foliation (SM3). *D*) convolute folds individuated by flow banding in pseudotachylyte matrix (SM7A0).

Cataclasites are in turn cross-cut by pseudotachylyte veins. Structural analyses of the fault zones suggest that pseudotachylyte generation is related to the late stages of fault evolution occurring at temperatures lower than 350-400°C, which represent the higher temperature limit for white mica + chlorite phase assemblage in mylonites. Microstructural analyses in thin sections revealed that quartz recrystallization is mainly dominated by grain bulging, pointing to temperature not in excess of 400°C (Passchier and Trouw 1996; Stipp et al. 2002). Evidence of multiple events of friction-induced melting within the Orobic and Porcile thrusts fault zones were easily observed at the micro-scale (Fig. 2.1.10), but systematic cross-cutting relationships between different pseudotachylyte generations were never observed in the field. Pseudotachylyte veins with thickness in excess of 5 mm usually display two symmetric outer black layers

and a lighter-coloured vein centre containing large inherited clasts. The dark grey to brass-like coloured vein centre has in most cases sharp contacts with black outer layers. Petrography and microfabric of pseudotachylyte veins were determined by optical microscopy and SEM (Scanning Electron Microscopy) on polished thin sections (Fig. 2.1.11). Clasts derived from the wall rock consist of quartz, plagioclase and minor lithics. The clast/matrix ratio decreases towards the vein centre, whereas the clast size increases. Reservoir pseudotachylyte veins, derived from the melt injections from the *mgs* towards the wall rock, usually occur along pre-existing fractures or secondary veins, are typically unzoned and display a clast/matrix ratio close to zero, probably due to a "bottle-neck" effect (O'Hara 2001). Quartz and plagioclase clasts are rounded or sub-rounded, with an aspect ratio comprised between 1 and 1.5. Elongated clasts are usually aligned parallel to the vein margins. The effective presence of melt during pseudotachylyte formation is supported by the occurrence of widespread resorption embayments in quartz and lithic clasts (Fig. 2.1.10 and Fig. 2.1.11). Isoclinal and convolute folds marked by alternating light and dark coloured matrix layers are common features observed in most of the analysed samples and are likely to be an effect of melt flow (Berlenback and Roering 1992; Lin 2008). The pseudotachylyte vein matrix consists of a cryptocrystalline poly-mineralic aggregate of quartz + biotite + plagioclase ± titanite ± epidote ± K-feldspar. Magnetite, ilmenite and sulfides sporadically occur in some samples derived from K-feldspar gneisses and epidote-bearing gneisses. In samples where both ilmenite and titanite crystallized from the pristine melt, ilmenite is found only within the black walls rimming the pseudotachylyte/wall rock contact, whereas titanite is present only in the central part of the veins.

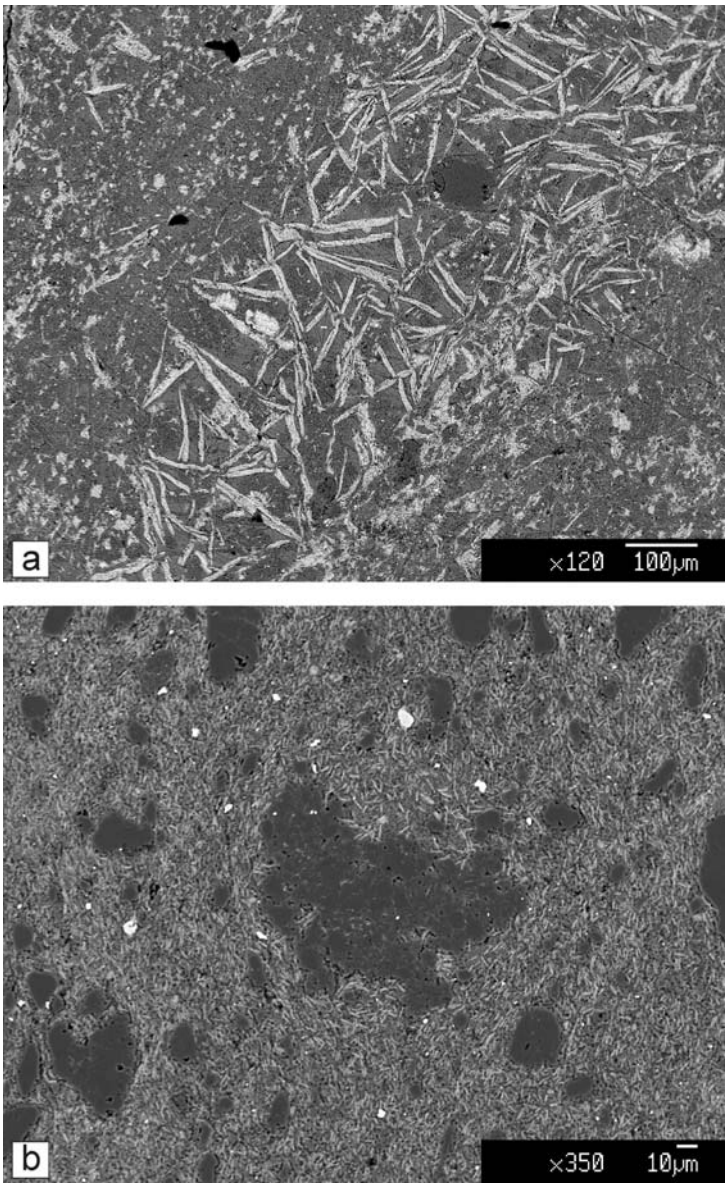

Fig. 2.1.11 Backscattered electron images (BSE - SEM) of microstructures within the pseudoachylyte veins (Zanchetta et al. 2010). (a) interleaved biotite-rich and biotite-poor layers within matrix. Biotite laths reach 80-100 µm in size. Injection vein in K-feldspar gneisses along the Porcile Thrust (sample PO8B). (b) biotite crystallites with a poorly defined SPO deflected around large quartz clasts (sample SM3).

Biotite represents the most abundant pristine mineral phase. It occurs both as spherulithic aggregates

reaching 50 μm in diameter and in laths up to 100 μm in length (Fig. 2.1.11). Biotite crystallites are typically more abundant close to the vein/wall rock contact and decrease towards the vein centre. In several samples biotite laths are concentrated in 20 to 100 μm thick layers within the pseudotachylyte vein (Fig. 2.1.10 and Fig. 2.1.11), instead of being homogeneously distributed as in other samples. The shape preferred orientation of biotite parallel to vein margins is likely to be an effect of syn-flow crystallization. Biotite laths crystallised from the melt differ from host rock biotite not only for shape, size and microstructures, but also in composition, with a systematically higher Ti-content.

2.1.5 Relative chronology of Alpine deformational events along the Orobic and Porcile thrusts

On the basis of collected field structural data, a relative chronology of the Alpine deformational events that interested the Orobic and Porcile thrusts areas can be reconstruct. Two main Alpine deformational events, referred as D3 and D4 in the literature (D5 and D6 in Blom and Passchier 1997), have been recognised in the hanging wall and footwall of the Orobic and Porcile thrusts.

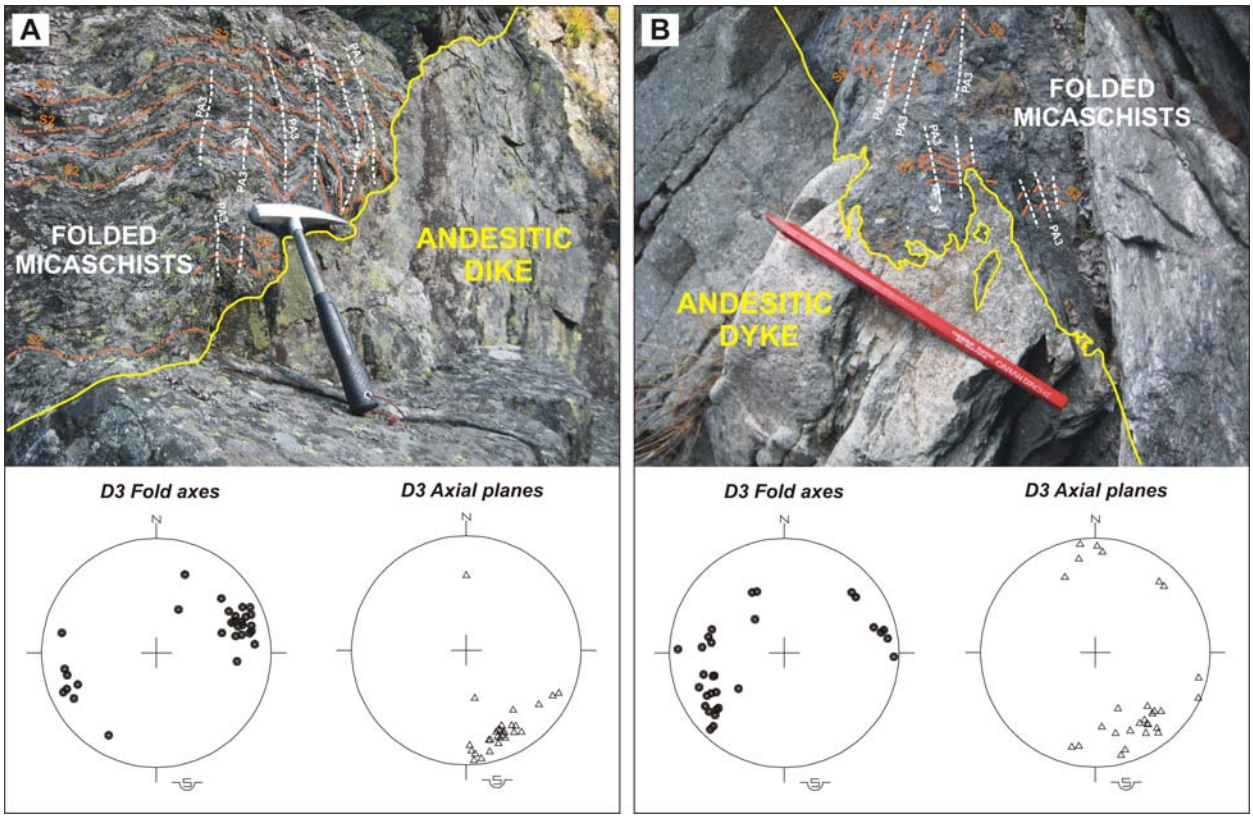

Fig. 2.1.12 Andesitic dikes croscutting D3 folds within the cristalline basement in the Scaiss Lake (A) and Venina Lake (B) areas.

In the San Marco pass – Porcile Lakes area the D3 event is related to the development of N-NW dipping folds which interfered with pre-Alpine D1 and D2 structures, without the formation of an axial plane schistosity. In other areas of the basement these folds have different orientations, usually showing E-W to ENE-WSW trending axes(i.e. Scaiss and Venina Lakes areas, Fig. 2.1.12). In the San Marco pass – Porcile Lakes area, the N-NW direction of D3 fold axes could be attributed to the presence of the Mt.

Fioraro ortogneiss complex, which acted as a rigid body modifying the local strss field during the initial stages of the Alpine compressions.

This event has been generally considered to pre-date the Adamello batholith (Siletto 1990; Carminati and Siletto 2005; Albini et al. 1994; Milano et al. 1988; Cadel et al. 1996), since overprinting relationships can be observed near the contacts with the intrusion. The occurrence of intermediate to mafic dykes cross-cutting D_3 folds developed within the basement (Fig. 2.1.12) could be used to define age constraints for this phase (Cadel et al. 1996). Unfortunately, their age is presently unknown.

A successive compressive event (D4) caused the formation of mylonites along the Orobic and Porcile thrusts and subsequent overprinting by cataclastic deformation (Fig. 2.1.13). Cataclasite bearing almost completely obliterated the pre-existing ductile fabric which is now only partly preserved within the hanging walls of the fault zones. Pseudotachylyte veins originated within cataclastic and ultracataclastic shear bands, and are interpreted to be syn- to post-cataclasis, thus providing a minimum age for the ductile-brittle transition along thrusts.

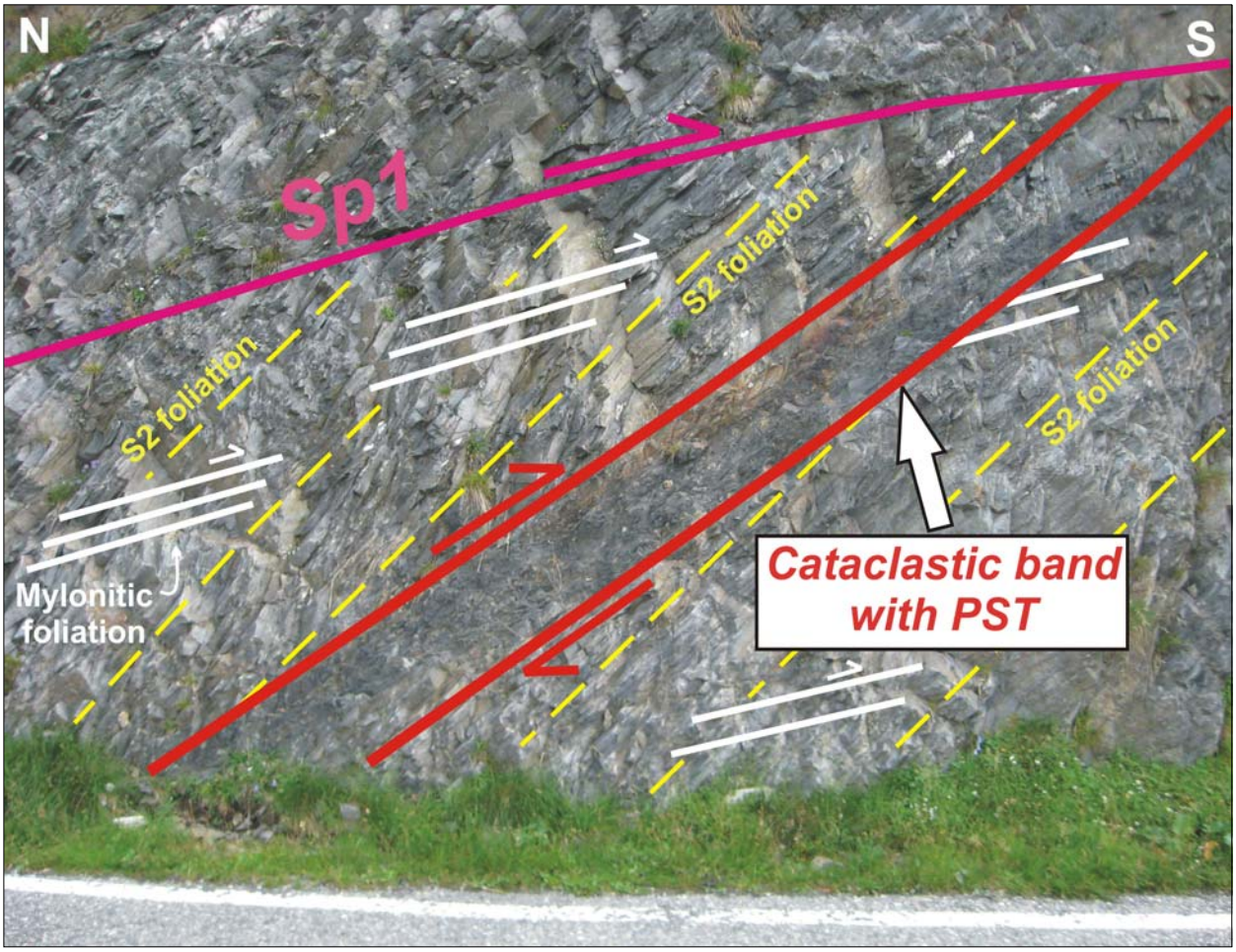

Fig. 2.1.13 Overprinting relationships among different deformational structures within the metamorphic basement in the hanging wall of the Orobic thrust (along the road to the San Marco pass). The pre-Alpine metamorphic S_2 foliation is partially overprinted by a N-dipping Alpine mylonitic foliation developed during the earliest stages of thrust activity. Later, both the S2 and the mylonitic foliations were strongly overprinted by cataclastic deformation with the formation of N-dipping cataclastic shear bands with several Pst veins. Cataclastic bands were in turn finally crosscut by discrete reverse fault planes (SP1 and SP2).

According to previous authors (Cadel et al. 1996; Carminati 2008), during D_3 compressions the transition from the ductile to the brittle deformational field occurred, and this event was therefore considered pre-

to syn-thrust. However, detailed field structural analyses performed in this work suggest that the D3 folding pre-dates the greenschists-facies mylonites related to the Orobic and Porcile thrusts, as mylonitic foliations cross-cut D3 folds. A progressive re-orientation of the D3 structures has been also observed moving toward the fault zones. Moreover, the ductile syn-thrust deformation is strongly partitioned between the fault zone (mylonites) and the sedimentary cover exposed along the footwall thrust, where a slaty cleavage affects the Permian to Lower Triassic units. For this reason the greenschists-facies mylonitic foliation and the following brittle structures developed within the basement (D4) can be geometrically associated to folding and related cleavage formation in the Permian-Triassic cover, whereas the D3 folding of the San Marco basement may be slightly younger than in the cover.

During field activity two different generations of pseudotachylyte veins have been recognized and this has been also confirmed by $^{40}Ar/^{39}Ar$ dating (see chapter 3). This suggests a reactivation of both the Orobic and Porcile thrusts during a later stage of compression.

Finally, a last deformational event caused the formation of low-angle, N-dipping reverse shear planes (SP1 and SP2 in Fig. 2.1.7, Fig. 2.1.8 and Fig. 2.1.13) which cross-cut all the previously formed structures.

2.2 Polyphase deformations in the Triassic cover: syn-thrust structures and relative chronology in the Grem-Vedra Transverse Zone

2.2.1 Introduction

Transverse zones affect fold-and-thrust belts and play a major role during their evolution, as they represent regional across-strike shear zones displacing adjacent sectors characterized by different deformation styles and/or amounts of shortening. These complex and articulated structures are the site for the development of tear faults and lateral ramps that interact with frontal ramps and thrust-related folds, causing abrupt along-strike changes in the lateral continuity of thrust-stacks.

The location of transverse zones within an orogenic belt are related to different controlling factors (Thomas 1990). Possible controls can be ascribed to changes in the tectonic regime or the existence of older tectonic lineaments or abrupt lithological changes, which act as weakness zones able to drive the development of these structures.

The study of transverse zones is favoured when they are developed within sedimentary units with a well-known stratigraphic setting, as in this case it is possible to use stratigraphic markers to confidently constrain (a) the throw of the faults and (b) the correlation of tectonic units across the transverse zone.

A favourable area for the study of transverse zones is represented by the fold-and-thrust belt of the Italian Southern Alps, which is segmented by the occurrence of important transverse zones. They generally reflect the reactivation of Upper Triassic to Jurassic normal faults related to the Mesozoic evolution of the Southalpine domain, which are oriented roughly parallel to the Alpine compressions (Berra and Carminati 2010 and references therein). The major example of this kind in the Southern Alps is the Giudicarie line, which represents the reactivation of a Mesozoic paleogeographic lineament separating the Trento Plateau from the Lombardian basin (Castellarin et al. 2006 for a synthesis). In the CSA Schönborn (1992) described other transverse zones, as the Faggio-Morterone, the Lugano and the Lake Lecco lines, whose position is controlled by the reactivation of Jurassic extensional faults which deeply interacted with the emplacement of thrust units during the Alpine compressions.

Another interesting transverse structure is represented by the poorly-known Grem–Vedra Transverse Zone (GVTZ), which is located in the CSA. Although the fault system was identified and described since the beginning of systematic studies of the Orobic Alps (De Sitter and De Sitter-Koomans 1949), due to the presence of Zn-related ore deposits of the Gorno mine district across the GVTZ, its interpretation is still controversial (Schönborn 1992; Forcella and Jadoul 2000). An important, often ignored, contribution to the understanding of the deep structure of the fault system was given by Rodeghiero and Vailati (1978), based on geological studies carried out during the construction of deep mining tunnels.

Aim of this chapter is to describe this complex N-S transverse zone providing a detailed scheme of its geometrical and structural setting, in order to understand its role during the tectonic evolution of the CSA.

The reconstruction of the GVTZ is supported by the production of a 3D geological model, which was built in order to validate our structural interpretation and obtain intelligible 3D visualizations of the main structures.

The kinematic history of the GVTZ has been also related with the relative chronology of the major deformation events occurring Southern Alps, contributing to the reconstruction of evolution of the entire thrust belt.

2.2.2 The Grem-Vedra Transverse Zone (GVTZ)

The study area (Fig. 2.2.1 and Fig. 2.2.2) includes part of the southern side of the Orobic Anticlines system, the Lower-Middle Triassic imbricates and the northern sector of the Upper Triassic succession. These different structural domains have a general E-W trend and are separated from each other by two main lineaments: the Valtorta - Val Canale Fault to the north and the Clusone fault to the south.

North of the Valtorta – Val Canale fault a Permian-Lower Triassic succession occurs (Trabuchello-Cabianca Anticline), including the Lower Permian volcanic and volcaniclastic successions of the Pizzo del Diavolo Fm. and Cabianca Vulcanite (Collio Formation *Auct.*), unconformably covered by the Upper Permian red conglomerates and sandstone of the Verrucano Lombardo, up to the Induan-Olenekian quartz-sandstones and siltstones of the Servino.

The Lower Triassic to Carnian succession to the south is arranged in a number of S-verging ramp-and-flat thrust systems which form a thrust stack with a regional antiformal arrangement. The oldest unit in the antiformal stack is represented by the sabkha facies of the Carniola di Bovegno, consisting of evaporitic dolostones with gypsum layers occurring along the main thrust surfaces as tectonic slices. The Anisian to Carnian succession (Fig. 2.2.3) includes subtidal and peritidal carbonates (Angolo Limestone, 250-300 m thick), basinal marly limestones (Prezzo Limestone, 10-15 m), carbonate platform facies (Esino Limestone, 600-700 m) characterized at the top by a regressive carbonate unit (Calcare Rosso), testifying to subaerial exposure. The Calcare Rosso is covered by peritidal (Breno Fm.) and later subtidal limestones (Calcare Metallifero Bergamasco, 80-100 m), followed by 150 to 300 m of lagoon marls and limestones (Gorno Fm.), laterally interfingering with deltaic sandstones (Val Sabbia Sandstone). The youngest unit in the thrust stack is represented by terrigenous-carbonate sabkha facies deposits of the San Giovanni Bianco Fm. (about 100 m preserved), including gypsum layers.

This antiformal stack is bounded to the south by the Clusone Fault which represents the detachment horizon developed along the San Giovanni Bianco Fm. The overlying Upper Triassic succession is mainly represented by the carbonate platform system of the Dolomia Principale and coeval basinal facies (more than 1 kilometer thick), exposed immediately south of the Clusone fault.

The Grem-Val Vedra Transverse Zone (GVTZ) is confined within the Middle Triassic to Carnian units, between the Valtorta – Valcanale and the Clusone faults.

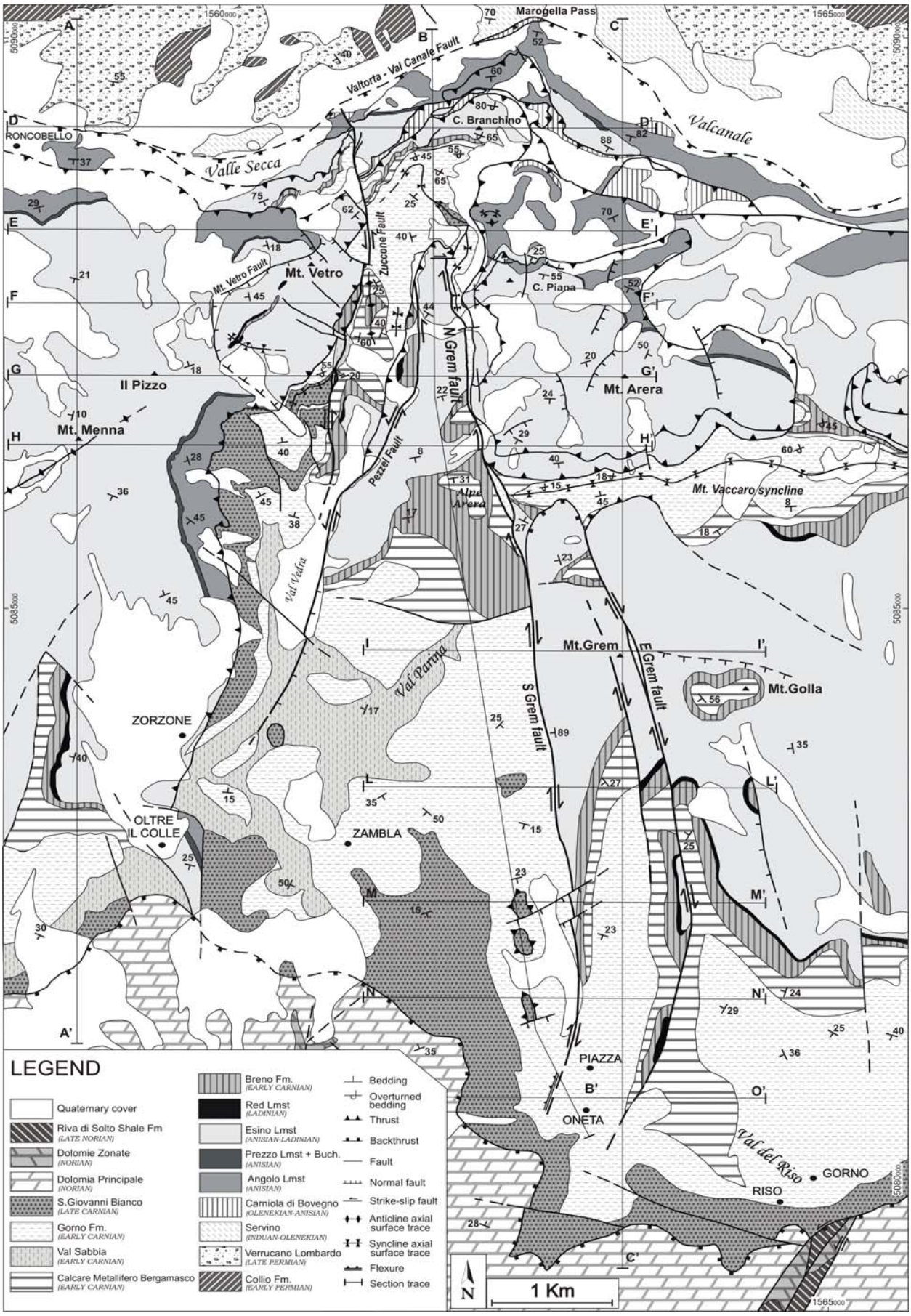

Figure 2.2.1 Geological-structural map of the GVTZ from original field mapping at 1:5,000 and 1:10,000 scale (D'Adda et al. submitted).

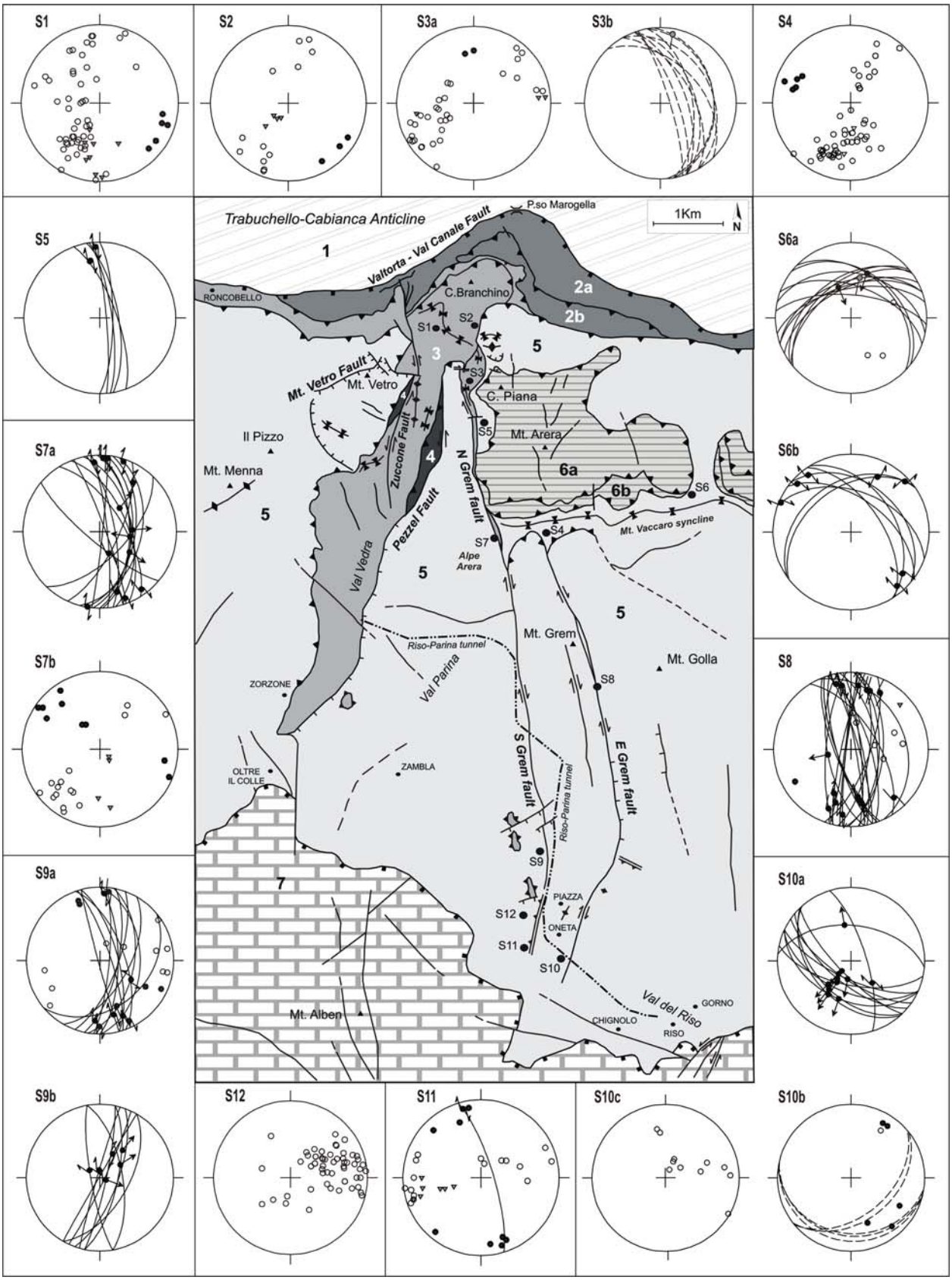

Figure 2.2.2 Interpretative tectonic scheme of the study area (D'Adda et al. submitted). The main tectonic units (see text for description) were identified on the base of mesostructural and stratigraphic analyses. Faults attitude and kinematic are described in the correlated stereographic projections (equal area, lower hemisphere). The trace of the Riso-Parina tunnel cross-cutting the GVTZ at depth is also reported.

2.2.3 Description of tectonic units and fault zones

The tectonic units were defined through original 1:5,000 to 1:10,000 field mapping improving the available 1:10,000 geological sheet "Roncobello" (CARG Regione Lombardia 2000) and the 1:50,000 Geologocal map of th Bergamo Province (Forcella and Jadoul 2000). Tectonic units are numbered according to their structural position from the lowest to the highest one. Stratigraphic and structural analyses, performed along all the transverse zone in the different tectonic units, are described in the following paragraphs.

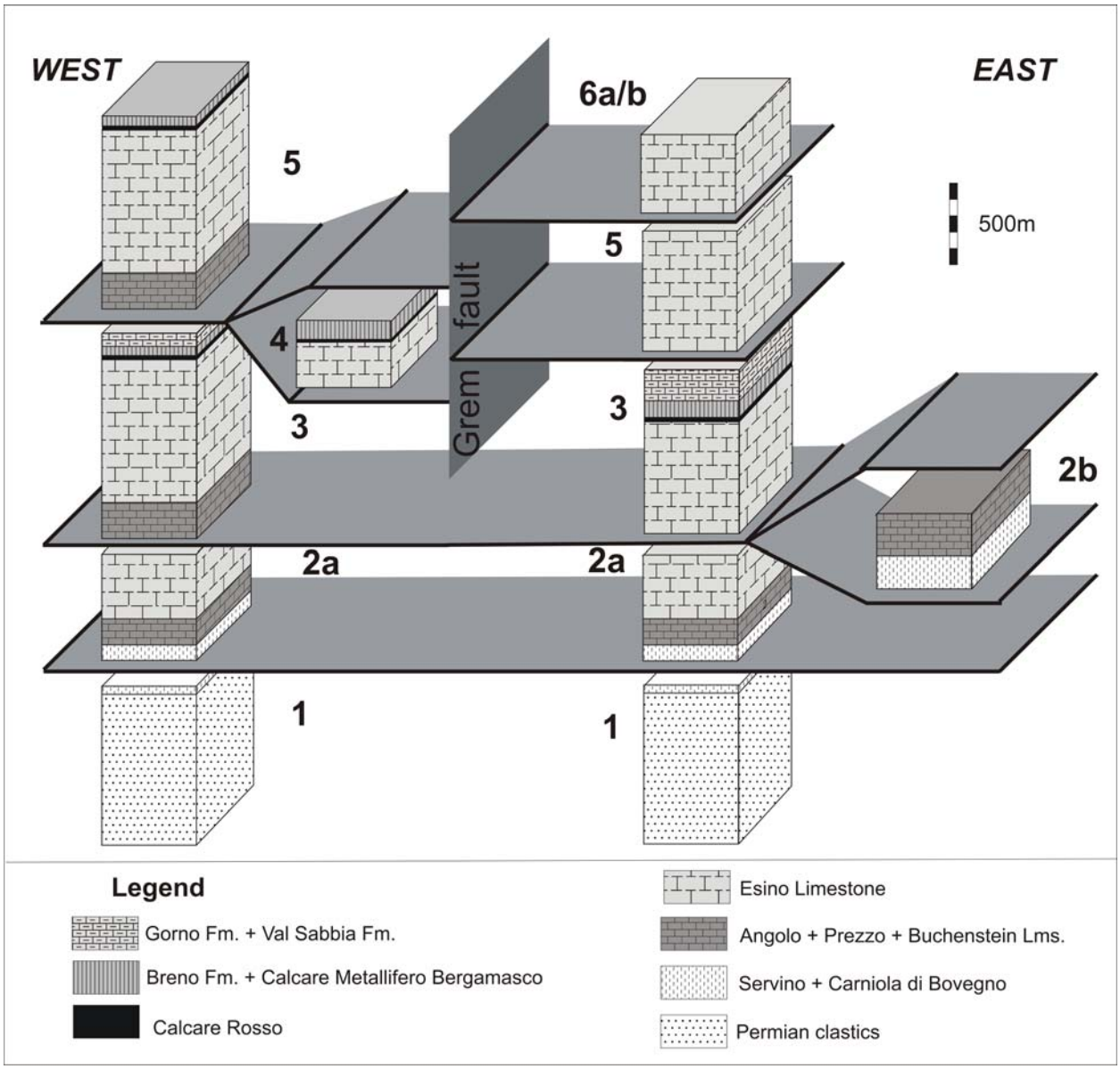

Figure 2.2.3 Schematic reconstruction of the stratigraphic setting of the study area (D'Adda et al. submitted).

Tectonic units of the GVTZ area

Unit 1: the *Trabuchello-Cabianca Anticline* (Fig. 2.2.2 and Fig. 2.2.4) belongs to the Orobic Anticline belt forming the structurally lowermost unit of the area. The Early Permian to Olenekian succession is folded in an open ramp anticline with sharp and regular flanks with angular hinges, interpreted as the

consequence of the south-verging propagation of a deep thrust surface (Schönborn 1992). A N-S trending fault crosses the unit to the north of the study area, tipping out around Baite di Mezzeno (Forcella and Jadoul 2000), but it does not cross the Valtorta – Val Canale fault and thus no relationships occur between this structure and the GVTZ.

The anticline is wedged under the imbricate Triassic units which are detached along the Valtorta – Val Canale fault.

Unit 2; *Val Canale unit* (Fig. 2.2.2 and Fig. 2.2.4): it develops south of the Valtorta – Val Canale fault, and consists of an Olenekian to Ladinian succession including thin layers of the Prezzo and Buchenstein Fms. at the base of the Esino Limestone. In the upper Val Secca (east of Roncobello) the unit is folded in an open asymmetric anticline with a N-dipping axial plane that clearly supports a southward transport during thrust stacking. The thickness of the unit increases eastwardand is well exposed all along Val Canale. A minor duplex structure due to a tectonic repetition (2b in Fig. 2.2.3) is present below the basal thrust surface of unit 3. The whole unit has been tilted southward due to the successive propagation of the Trabuchello-Cabianca Anticline (sections B-B' and C-C'; Fig. 2.2.4). Field data suggest that unit 2 disappears southward at depth below the overlying unit 3. The N-S Zuccone fault cross-cuts unit 2 to the north, forming a complex horse-tail branching termination exposed along Valsecca, east of Roncobello.

Unit 3; *Branchino unit* (Fig. 2.2.2): it forms the left side of Val Secca, the Corno Branchino massif, and a large part of Val Vedra. It is characterized by an Olenekian to Upper Carnian succession, strongly deformed along the GVTZ. The overturned syncline of Corno Branchino is one of the most peculiar elements of this unit. We interpret this fold as a footwall syncline related with the emplacement of higher thrust sheets now eroded in this area. The axial surface dips N-NE, indicating top-to-the-south transport direction during the growth of the thrust stack. Increasing distortion of the axial surface from E-W to N-S at the northern tip of the Grem fault, west of Corna Piana (Fig. 2.2.2) suggests that the right-lateral slip along the fault was coeval to the growth of the fold during thrust emplacement. An overturned syncline with similar characters crops out along the right side of Val Vedra south of Mt. Vetro . Despite its smaller amplitude and wavelength, this fold is very similar to the Branchino syncline, suggesting that they both formed as footwall fault propagation folds during southward thrusts motion. NW of Oneta three small tectonic windows expose unit 3 below unit 5 along the Riso valley. The top of the underlying unit is marked by mylonites formed between the marly limestones of the Gorno Fm. (unit 5) and the characteristic layers of tectonic "carniola" belonging to the underlying San Giovanni Bianco Fm. (unit 3). Further constraints on the deep setting of unit 3 come from subsurface geological observations made during the construction of the Riso-Parina mine tunnel (Rodeghiero and Vailati 1978; trace of the tunnel in Fig. 2.2.2). As shown by the E-W trending geological cross-sections along the southern sector of the Grem fault (Fig. 2.2.7), which integrate our own surface observation with subsurface data form Rodeghiero and Vailati (1978), the eastern portion of unit 3 is lowered by a lateral ramp, progressively passing eastward to the floor thrust of the unit. The N-S trending lateral ramp directly juxtaposes the Esino Limestone of the overlying unit 5 to the deformed Gorno Fm of unit 3. This structural setting drove

the

Figure 2.2.4 N-S cross sections (D'Adda et al. submitted). Cross section A-A' and C-C' are located outside the GVTZ, to the W and E repsectively. The B-B' cross section trace id entirely within the GVTZ. Cross sections traces are reported on the geological map of Fig. 2.2.1.

excavation of the Riso-Parina tunnel, which flanks for more than 2 kilometers the ramp, before turrning westward into the San Giovanni Fm. of unit 3 (Rodeghiero, pers. com.). Mylonitic layers formed in the Gorno Fm., similar to the ones exposed along the Riso valley, characterize this fault surface along the N-S track of the Riso-Parina tunnel. This lateral ramp represents the deep expression of the southern portion of the Grem fault. According to our data, unit 3 continues in depth also in the southern portion of the study area.

Unit 4; *Val Vedra Unit* (Fig. 2.2.2): it is a small horse formed between units 3 and 5, exposed along Val Vedra. This previously unknown unit has a maximum thickness of 100 meters and consists of a succession spanning from the upper part of the Esino Limestone to the lower part of the Breno Fm.

Unit 5; *Menna-Nossana Unit* (Fig. 2.2.2): it is the largest thrust sheet occurring in the study area. It consists of a thick and continuous Anisian to Carnian carbonate succession largely including the Angolo and Esino Limestone which forms the Mt. Menna, Corna Piana and Mt. Arera massifs. The unit is split into three sectors by the the Zuccone and Grem faults of the GVTZ (Fig. 2.2.2). Previous authors considered them as different units, but no significant lithological, stratigraphic and structural differences occur among these units. In addition, the stratigraphic continuity of the Carnian succession across the central and eastern sectors south of Oneta, where the Grem fault tips out, shows that they all belong to the same thrust sheet.

The westernmost sector is characterized by a south-verging *ramp and flat* system sole thrust flooring the rigid body of thr Mt. Menna – Mt. Vetro massif. The same unit is gently folded south of the summit of Mt-Menna reaching the village of Zorzone, along the western side of Val Vedra. The floor thrust of the unit is cut by the Zuccone fault (Fig. 2.2.1 and Fig. 2.2.2). Mt. Vetro is crossed by a N-S trending, E-dipping normal fault lowering the eastern sector of the massif. As this fault ends west of the Zuccone fault and does not cross the thrust surface at the base of unit 5, it can be confidently interpreted as a pre-thrusting structure, passively transported during thrust stacking. A more complex geometrical setting can be recognized to the east, as unit 5 is cut by the Grem fault which separates the central and the eastern sectors, and by other minor faults forming minor blocks and tectonic repetitions. The central sector (Zambla - Val Parina; Fig. 2.2.2) is comprised between the Grem and Pezzel faults. It behaved as a rigid wedge-shaped block partially juxtaposed to unit 3 in its northern part and in contact with the eastern portion of unit 5 south of Alpe Arera. This sector of unit 5 thins out to the south, due to the formation of a ramp cutting through the folded Ladinian carbonates and reaching the Carnian succession as documented by small tectonic windows along the Riso valley. in which the San Giovanni Bianco Fm. of the underlying unit 3 is exposed below mylonitic limestones of the Gorno Fm. Of unit 5 (Fig. 2.2.2). South of Oneta, where the southern portion of the Grem fault tips out within the Gorno Fm., the central and eastern sectors of unit 5 directly merge, confirming that the three sectors belong to the same tectonic unit. The eastern sector of the unit also shows a lateral ramp with unit 3 around Passo Branchino (Fig. 2.2.5a) passing to the transpressional Grem fault southward, where it is partially covered by the uppermost thrust sheets of the stack (unit 6). The E-W trending Vaccaro overturned syncline, which formed during the

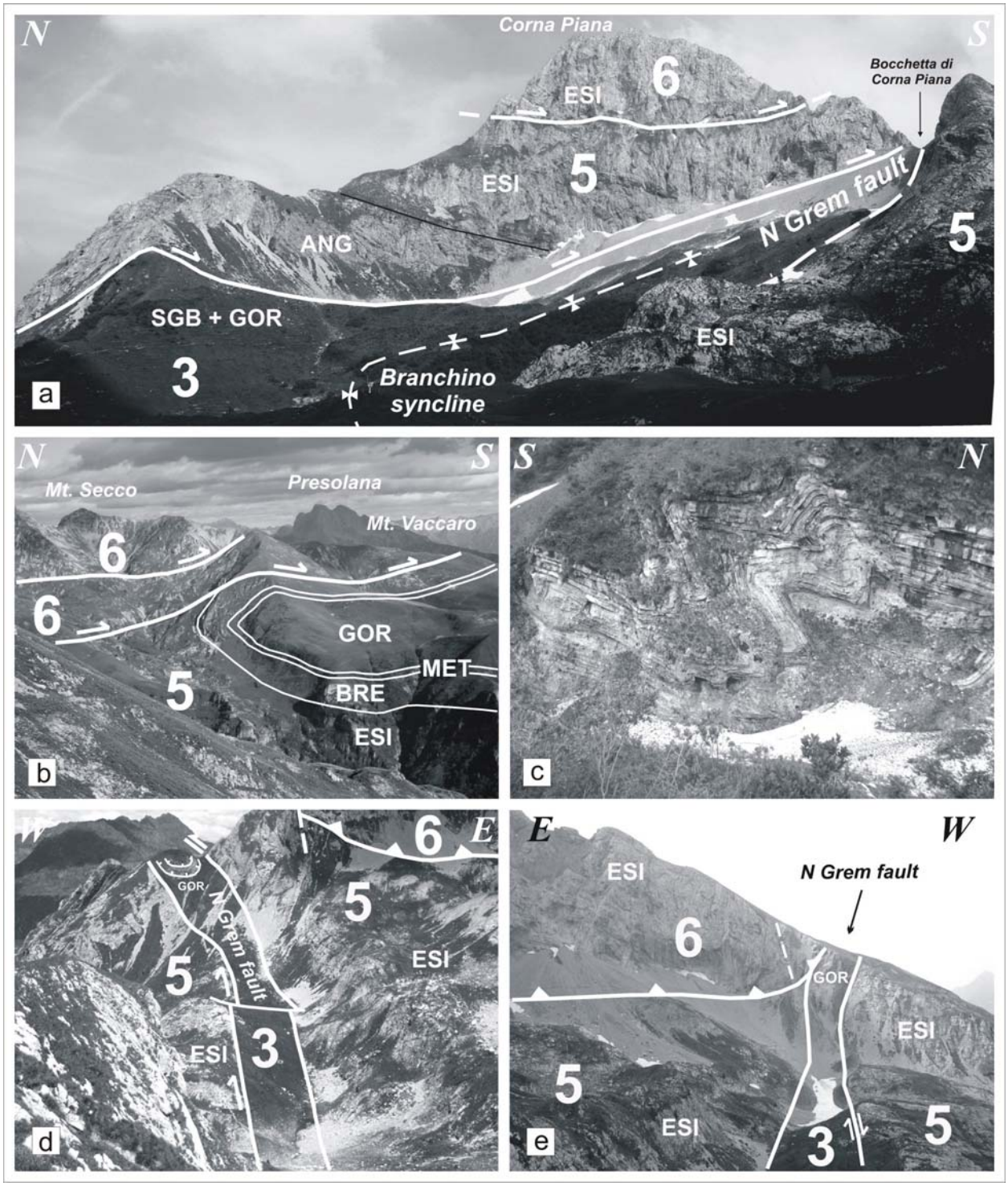

Figure 2.2.5 Field photographs of the main structures in the study area (D'Adda et al. submitted). a) The uppermost thrust sheets: the Menna-Nossana (5) and the Arera (6) units exposed on the west flank of Mt. Corna Piana. b) the Mt. Vaccaro syncline. c) Asymmetric parasitic folds along the lower limb of the Mt. Vaccaro syncline. d) the S termination of the Corno Branchino syncline E of Mt. Arera. e) Relationships between the N Grem fault and the floor thrust of the Mt Arera unit (6).

southward thrusting of the higher thrust sheets (units 5 and 6; section C-C' in Fig. 2.2.4 and Fig. 2.2.5b), occurs south of Mt Arera. The fold has a N-dipping axial surface and is characterized by parasitic folds on its normal flank (Fig. 2.2.5c and site S4 in Fig. 2.2.2).

The whole structure, extending from Mt. Vaccaro to Mt. Arera, is sharply cut westward by the Grem fault without any distortion of the axial surface. Forcella and Jadoul (2000) suggested that the Vaccaro and

Branchino synclines were part of the same structure, then displaced by the Grem fault with a right-lateral throw of at least 1,5 - 2 kilometers. However, field data indicate that the Vaccaro syncline belongs to a higher structural level (unit 5) with respect to the Branchino syncline (unit 3), implying that they cannot be used as markers to evaluate the displacement occurred along the Grem fault.

North of Mt Grem, along Val Parina, the Esino Limestone is partially back-thrust onto the Carnian units at the core of the Vaccaro syncline. The E-W backthrust is bounded to the west by the Grem fault and by a NNW-SSE trending right lateral strike-slip to the east, here named E-Grem fault, which cut across the unit near the top of Mt. Grem (Fig. 2.2.2, site S8).

According to subsurface observations (Rodeghiero & Vailati, 1978) along the Riso-Parina tunnel (550 m a.s.l.), the floor thrust of the eastern sector of unit 5 gently dips southward running within the Esino Limestone, so that the sole thrust of unit 5 is much deeper than to the west of the Grem fault.

Unit 6; *Arera unit* (Fig. 2.2.2): it forms the klippe of the Corna Piana-Mt. Arera massif which is exposed east of the Grem fault. This unit also includes an Anisian to Ladinian succession with the Angolo, Prezzo and Esino Limestones (Fig. 2.2.3). The basal thrust is well exposed along the northern slope of Corna Piana, where it forms a ramp dipping between 30° and 40° to the north, marked by carbonate mylonites up to 3 m thick. Southward, along the southern slope of Mt Arera, the thrust surface is nearly flat, documenting a ramp-and-flat geometry. Duplex structures, revealed by the occurrence of small horses consisting of cataclastic layers in the Esino Limestone, occur along the southern part of the floor thrust of the unit. In addition, small normal faults displace the thrust sheet north of Mt. Corna Piana. Unit 6 is the uppermost unit of the stack and its structural position is comparable with the Presolana unit east of Val Seriana (Forcella 1988; Zanchi et al. 1990a). The occurrence of mylonites along their floor thrusts suggests similar deformation mechanisms during thrusting in both units.

The main fault zones of the GVTZ

The main fault of the GVTZ is represented by the Grem fault. It has a NNW-SSE trend and occurs just south of Passo Branchino passing along the western flank of Corna Piana and along the SW flank of Mt. Arera. The fault extends southward along the western slope of Mt. Grem, tipping out NW of Oneta (Fig. 2.2.2). The fault has been always represented as an unique continuous structure, but our field data suggest that it consists of two different segments with different characters and structural meaning.

The northern segment (N-Grem fault) is marked by a few meters-large tectonic slice consisting of strongly deformed and folded marly limestones attributed to the Gorno Fm. of unit 3 (Fig. 2.2.5 d-e; Fig. 2.2.6, cross sections F-F', G-G', H-H'). In this area the N-Grem fault represents the steep lateral ramp for units 5 and 6, as suggested by the geometry of their thrust surfaces west of Mt. Arera (Fig. 2.2.6, cross sections F-F', G-G', H-H').

The termination of the N-Grem fault north of Passo Branchino, as well as the lateral closure of unit 3 east of Corno Branchino, suggests that the fault is confined in unit 3, 5, and 6. Dextral motion with a slight oblique reverse component is supported by striations, growth fibers, and pressure solution cleavage along

the fault plane (Fig. 2.2.2, sites S5, S7, S9a). These data are consistent with dragging and torsion of the Corno Branchino syncline, which is progressively rotated clockwise from E-W to N-S along the fault trace (Fig. 2.2.2, sites S1, S2 and S3), suggesting that the N-Grem fault was already active during the growth of the Branchino syncline.

The southern branch of the Grem fault (S-Grem fault) separates the central and eastern sector of unit 5. It

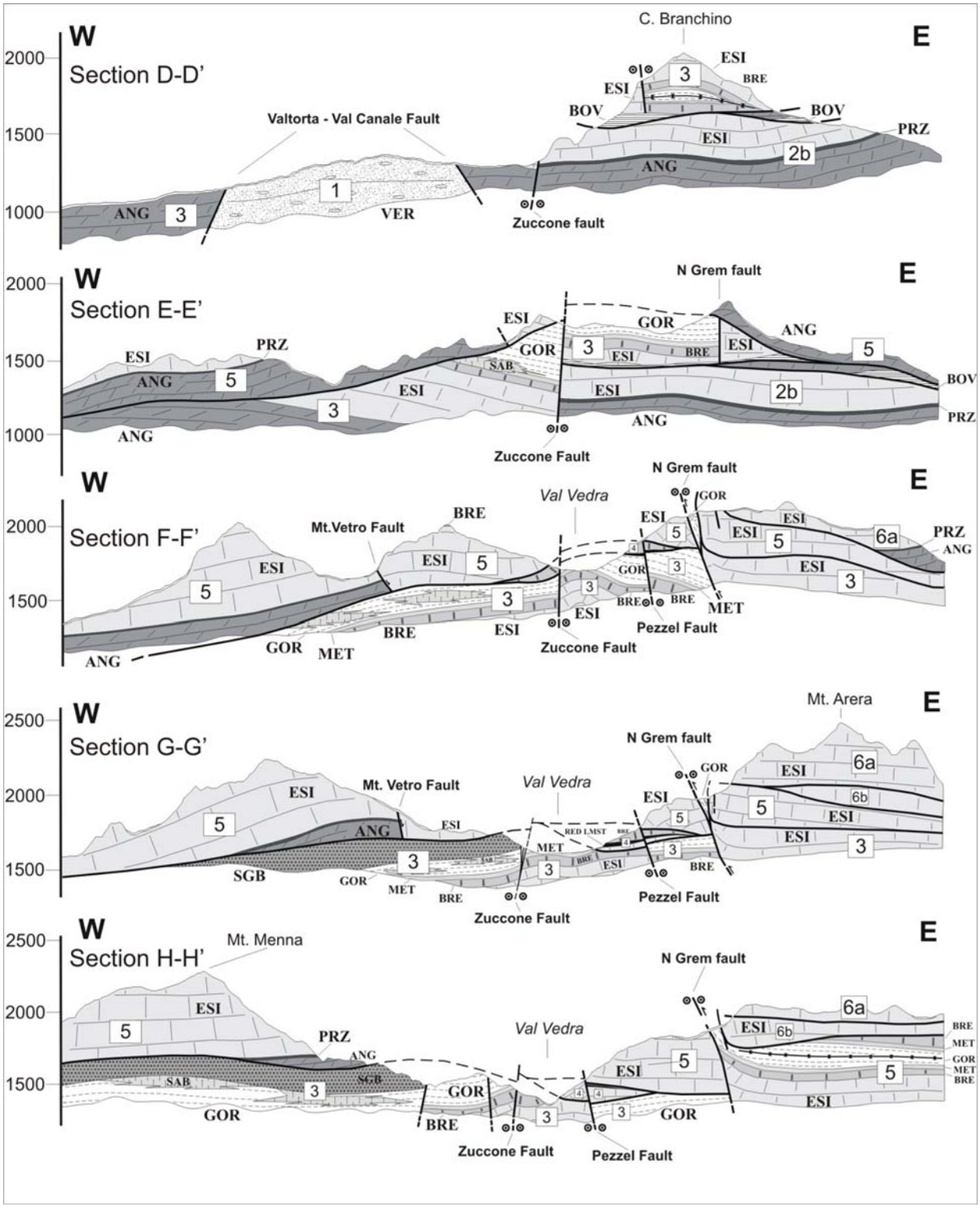

Figure 2.2.6 E-W cross sections across the GVTZ (N Grem fault segment) N of the Mt. Vaccaro syncline (D'Adda et al. submitted). Cross sections traces are reported on the geological map of Fig. 2.2.1.

shows different features with respect to N-Grem fault, as it becomes steeper and continues southward as a tear fault parallel to the thrust propagation direction. The S Grem fault also shows a significant vertical displacement reaching a maximum throw of a few hundred meters (Rodeghiero and Vailati 1978), due to oblique motion along the exposed portion of the fault system (Fig. 2.2.7). A similar amount of the maximum horizontal displacement can be also evaluated. As shown in Figure 2.2.2 and in cross sections of Figure 2.2.8, moving southward from Val Parina, the throw of the S-Grem fault decreases and the fault ends SW of Oneta where it tips out in a N-S trending flexure. South of Mt. Arera, part of the displacement occurring along the S-Grem fault within unit 5 is respectively partitioned along the E-Grem fault, which shows similar features and kinematics, and by the successive back-thrusting of the Esino Limestone on the Vaccaro syncline.

The S-Grem fault nucleates on a deeper wrench fault represented by the lateral ramp of the sole thrust of unit 5. The lateral ramp is responsible for the lateral juxtaposition at depth of the San Giovanni Fm. of unit 3 with the Esino Limestone of unit 5 for more than 2.5 km, as observed along the N-S segment of the Riso-Parina tunnel. Units 3 and 5 are here separated by a thick, N-S trending, steep cataclastic to mylonitic shear zone enclosing strongly deformed

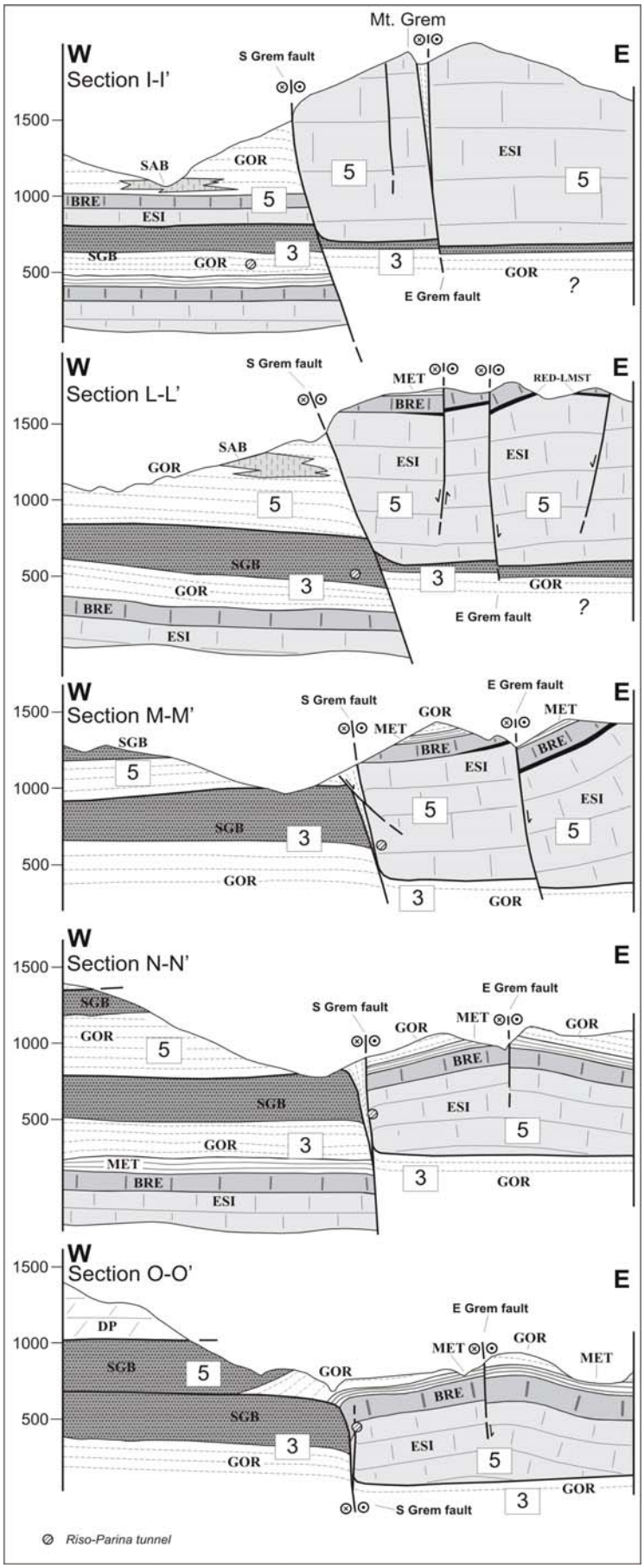

Figure 2.2.7 E-W cross section across the GVTZ (S Grem fault segment) S of the Mt. Vaccaro syncline (D'Adda et al. submitted). Cross sections traces reported on the geological map of Fig. 2.2.1.

layers of the Gorno Fm. The lateral ramp can be observed also at a depth of about 200 meters south of Oneta, where the S-Grem fault tips out at the surface. The ramp has been successively cross-cut by a vertical strike-slip fault which corresponds to the presently exposed segment of the S-Grem fault. This shallower portion of the fault accommodates the vertical offset between the eastern and central portion of unit 5. The total vertical displacement progressively increases from the southern tip of the fault (Oneta) toward the north (Val Parina), where the eastern block is uplifted of several hundred meters with respect to the central sector of the unit due to back-thrusting on the Vaccaro syncline.

The Zuccone Fault is a composite N-S to NNE-SSW left-lateral system crossing the western flank of Val Vedra. It steeply deeps westward and extends for about 5-6 km ending with a horse-tail branching termination into the lowermost unit just south of the Valtorta – Val Canale fault (Fig. 2.2.1 and 2.2.2). The displacement of the overturned syncline exposed south of Mt. Vetro (unit 3), and kinematic indicators along the main fault plane, supports a left-lateral kinematics of the fault. The Zuccone fault was probably active during the emplacement of units 5 and 4, similarly to the N-Grem fault. At least 250m of vertical offset was accommodated by this fault. The hanging wall (unit 5, Mt. Menna) is clearly lowered westward and this may be partially related to a later reactivation of the structure as a normal fault, which accounts for the apparent dextral displacement of the thrust surfaces along the northern part of the fault.

The NE-SW trending and E-dipping Pezzel fault bounds to the W the central sector of unit 5 (Fig. 2.2.1, Fig. 2.2.2 and cross sections F-F', G-G', H-H' in Fig. 2.2.6). Vertical mylonitic foliation oblique to the fault strike suggest a left-lateral motion, as also suggested by previous authors (Rodeghiero and Vailati 1978; Vailati 1978). A minor extensional reactivation affected the southernmost part of the fault. The southern continuation of the fault bounds the eastern side of the Val Vedra half-window, juxtaposing unit 5 and unit 3.

2.2.4 A 3D Model of the GVTZ

The 2D representation of geological structures shown in traditional geological maps is often inadequate to represent exhaustively the structural intricacy of a complex area. The use of 3D software techniques for structural modelling gives the opportunity to analyse, reconstruct and visualize more efficiently complex structures. A 3D model can also be useful to validate structural interpretations based on 2D field data and to eventually check different hypotheses when surface structural data are poor or uncertain. Several examples of integration of different type of data to reconstruct subsurface geological objects have been published, with particular regards to those based on field data (de Kemp 1999, 2000; Husson and Mugnier 2003; Maxelon and Mancktelow 2005; de Kemp et al. 2006; Zanchi et al. 2009). On the basis of these previous experiences, a 3D model of the Vaccaro and Branchino synclines have been realized (Fig. 2.2.8 and Fig. 2.2.9) and will be discussed below. The Branchino syncline has been chosen in order to describe its complex geometry which can not be reliably represented though conventional 2D cross-sections and then compared to the simpler Vaccaro syncline. Three main typologies of geometric features and related attributes were managed in a GIS-database and later exported into the 3D modeling software Move (©

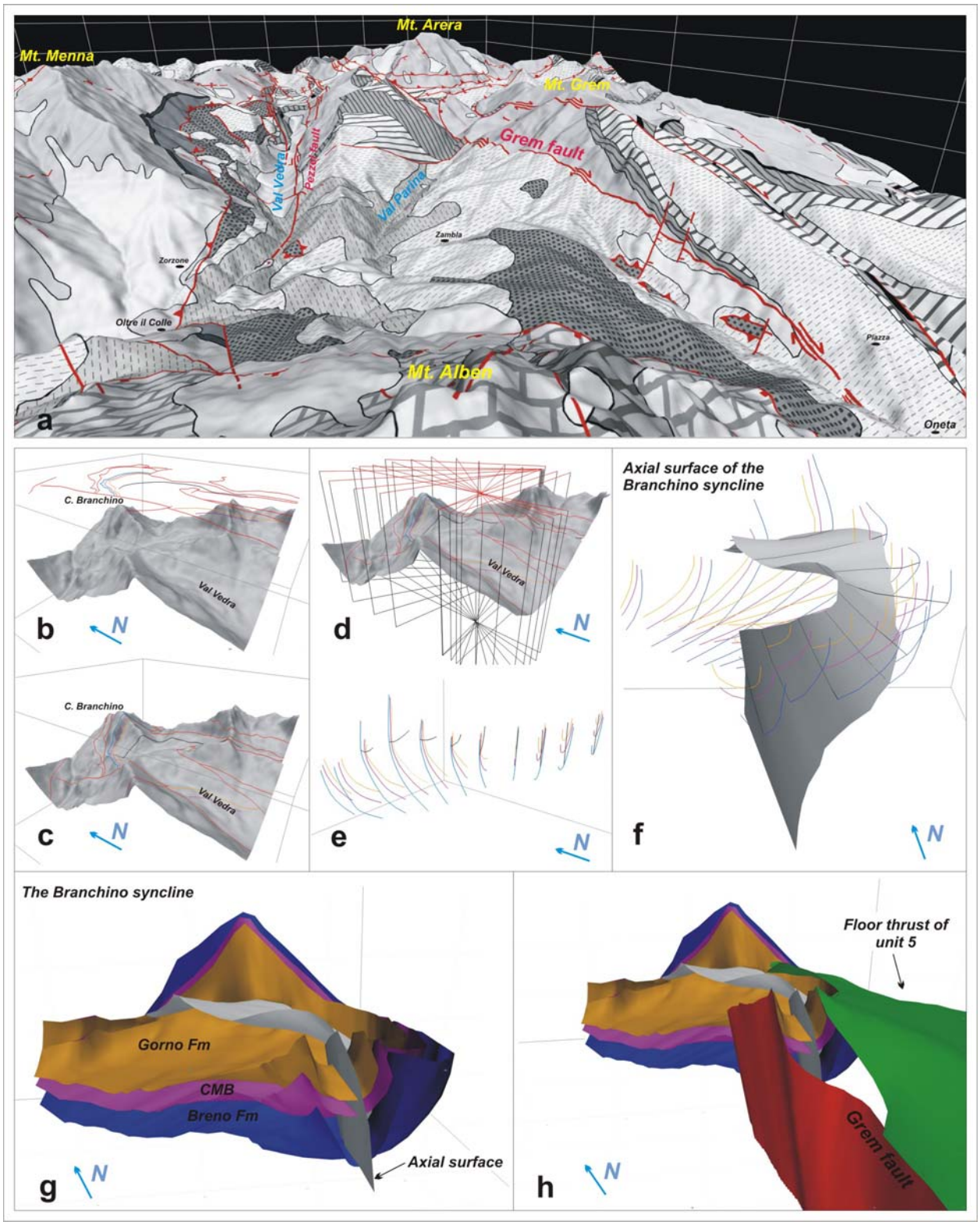

Figure 2.2.8 3D model of the GVTZ (D'Adda et al. 2010). a) Geological structural map draped on the 20 m pixel size DEM of Regione Lombardia. b-f) The workflow used to integrate field data as lithological boundaries, fault and thrust surface traces in a 3D environment to build a 3D cross sections grid. g-h) Reconstructed 3D surfaces of the Corno Branchino syncline, the N Grem fault and the floor thrust of the Menna-Nossana thrust sheet (unit 5).

Midland Valley Inc): a digital elevation model (DEM) of the topographic surface (obtained using the 20m pixel size Digital-Terrain-Model of Regione Lombardia), stratigraphic and tectonic boundaries, traces of fold axial plane (2D poly-lines), and structural data as point features. After having imported all objects in Move, linear features have been vertically projected on the DEM in order to obtain a 3D geological map

(Fig. 2.2.8a) showing the main stratigraphic and structural elements in the northern part of the GVTZ. Geometrical constraints (Chilès et al. 2004) to be used for the construction of a grid of cross sections have been defined based on field structural analyses and also on orientation analyses of the collected data through Move. The analysis has mainly concerned the attitude of planar and linear features as bedding, faults, foliations, fold axes and axial planes. Particular care has been given to the attitude of mesoscopic features (bedding and cleavage), in order to provide an accurate description of this complex structure, and to better evaluate its geometry.

A grid with about 20 geological cross sections has been drawn in Move; the strike and the extent of each section have been chosen in order to introduce into our model all the constraints derived from field structural analyses. The surfaces representing thrust planes, strike-slip faults, stratigraphic boundaries and

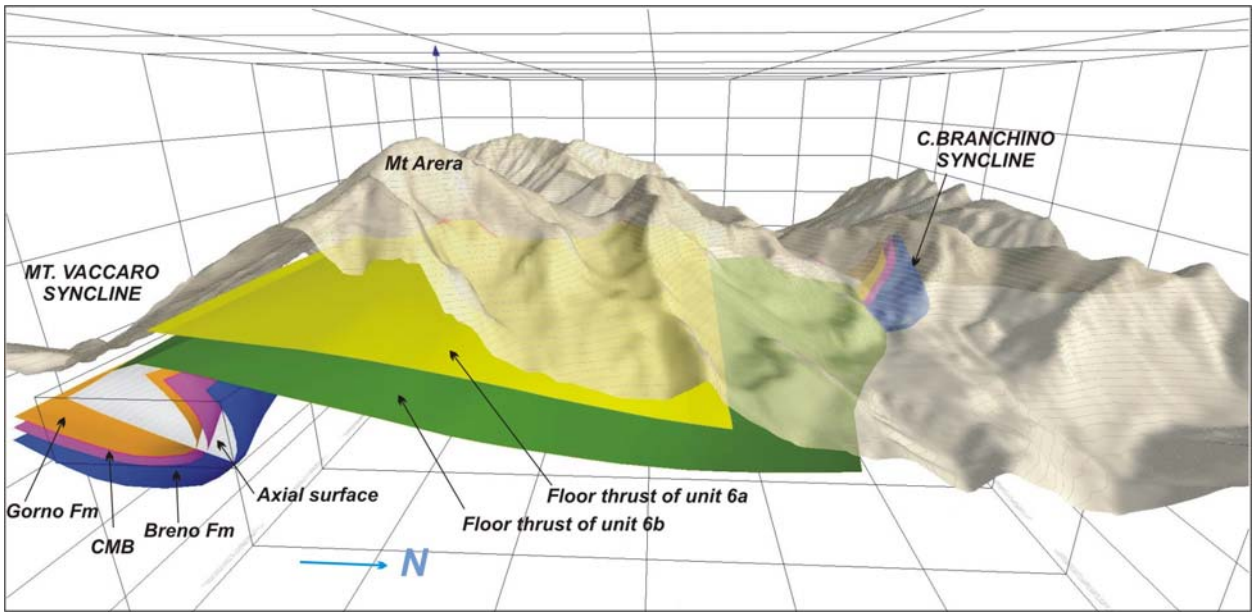

Figure 2.2.9 3D image of the Mt. Vaccaro syncline, developed in the floor thrust of the Arera unit (image b in Fig. 2.2.5). (D'Adda et al. submitted).

axial planes of folds have been then obtained interpolating the corresponding linear features contained in the cross sections grid. The obtained models have been refined until it strictly honored the field data.

The Branchino and Vaccaro folds have been built using cross sections perpendicular to the strike of axial planes (Fig 2.2.8f), whereas both parallel and perpendicular cross sections were used to reconstruct fault planes (Fig 2.2.8h). The 3D model of the Branchino syncline helps to constrain the extension at depth of this structural object and promptly visualize its geometrical and kinematic relationships with the boundary faults of the transverse zone (especially the Grem fault) and the main thrust surfaces.

2.2.5 Structural evolution of the GVTZ during Alpine tectonics

Two main compressive stages affected the CSA before the intrusion of the Upper Eocene – Lower Oligocene Adamello batholith (Brack 1981; Laubscher 1985; Doglioni and Bosellini 1987; Schönborn 1992; Castellarin et al. 2006; Zanchetta et al. 2010; D'Adda et al. 2010 and this work). In the GVTZ area the occurrence of two deformational events is highlighted by the presence of compressive structures with different styles and geometries, suggesting a close relationship between the evolution of the transverse

zone and the progressive growth of the thrust belt (Fig. 2.2.10 and Fig. 2.2.11). It follows that it is therefore possible to confidently relate the two-stage evolution of the GVTZ to the two pre-Adamello compressive stages recognized in the CSA.

First pre-Adamello compressional stage

According to Laubscher (1985) and Schönborn (1992), the first Alpine compressive event resulted in the emplacement of the Orobic thrust sheet. Both basement and cover were thrust southward forming a thick imbricate thrust stack (Thrust system 1, Schönborn 1992). This first compressive phase lasted for a rather long time and was Late Cretaceous in age, as recently pointed out by $^{40}Ar/^{39}Ar$ dating of fault-related pseudotachylytes along the Orobic thrust (Meier 2003; Zanchetta et al. 2010, and this work), and previously postulated by other authors (Doglioni and Bosellini 1987; Bernoulli and Winkler 1990; Zanchi et al. 1990; Bersezio et al. 1993; Castellarin et al. 2006) on the basis of the occurrence of the Cenomanian to Campanian turbiditic successions of the Lombardian Flysch.

We refer to this phase the emplacement of the whole imbricates south of the Valtorta – Val Canale fault (from unit 2 to unit 6), which were stacked southward following a break-forward thrusting sequence.

During the southward thrusting of the Arera unit (unit 6), the upper part of the Anisian to Carnian succession of the underlying Menna-Nossana unit (unit 5) was dragged and involved in a regional E-W trending overturned footwall syncline (Vaccaro syncline, Fig. 2.2.10a) as a result of early fault-propagation folding and subsequent out-of-anticline evolution of the thrust surface. The N-Grem fault formed as the lateral ramp of unit 6, with a dextral strike-slip kinematics.

The continuation of the compression (Fig 2.2.10b) caused the in-sequence stacking of the Menna-Nossana unit (unit 5) to the south, forming in its footwall the small horse of the Val Vedra unit (unit 4). During this stage, the floor thrust of unit 6 was probably deactivated and passively transported southward on top of unit 5.

The N-Grem fault propagated downward at depth between units 3 and 5, splitting unit 5 forming a high-angle lateral ramp which lowered the SE portion of the floor thrust of unit 5, as suggested by the observations carried out along mine tunnels (Rodeghiero and Vailati 1978). Dextral strike-slip motion occurred along the fault plane, sharply cutting the western termination of the Vaccaro syncline. The southward motion of unit 5 produced a regional overturned drag fold in the Ladinian to Carnian succession of the underlying unit 3 (Branchino syncline), which was distorted and rotated clockwise along the N-Grem fault in a transpressional strain regime (Fig. 2.2.8 and Fig. 2.2.11). Vertical tectonic slices consisting of strongly deformed and folded marly limestone of the Gorno Fm. along the northern sector of the fault (Fig. 2.2.5d and e and cross sections in Fig. 2.2.6) suggest the deep involvement of unit 3 during the development of the N-Grem transpressional shear zone.

At the same time, the left-lateral Zuccone fault became active to the west, separating and displacing the western and the central sectors of unit 5. A small overturned syncline formed in the Carnian succession of unit 3 south of Mt. Vetro with a N-dipping axial surface and a general E-NE trend and seems to be

distorted by the Zuccone fault. The fold has the same structural position and similar geometrical characters of the Branchino syncline, suggesting that they were both initially related to southward thrust propagation.

The southward thrusting of units 2 (a and b) can be still related to this second stage of thrusting. These units were stacked following the break-forward thrusting sequence of the upper units, which were passively transported to the south. The presently south-dipping floor and roof thrusts is likely related to the passive tilting of the thrust surfaces due to the emplacement of the Orobic Anticline, as supported by the presence of south-verging asymmetric folds in unit 2. It is worth noting that the N-Grem Fault is restricted to units 3, 5 and 6, as units 2 and 2b extend continuously across the Brembana-Seriana valleys watershed.

According to this reconstruction, the N-Grem fault (and probably also the Zuccone fault) produced a ductile distortion of a thrust-related drag fold, clearly indicating syn-thrust activity (Fig 2.2.11a) and suggesting that the beginning of the tectonic activity in the GVTZ can be referred to the first pre-Adamello compressions.

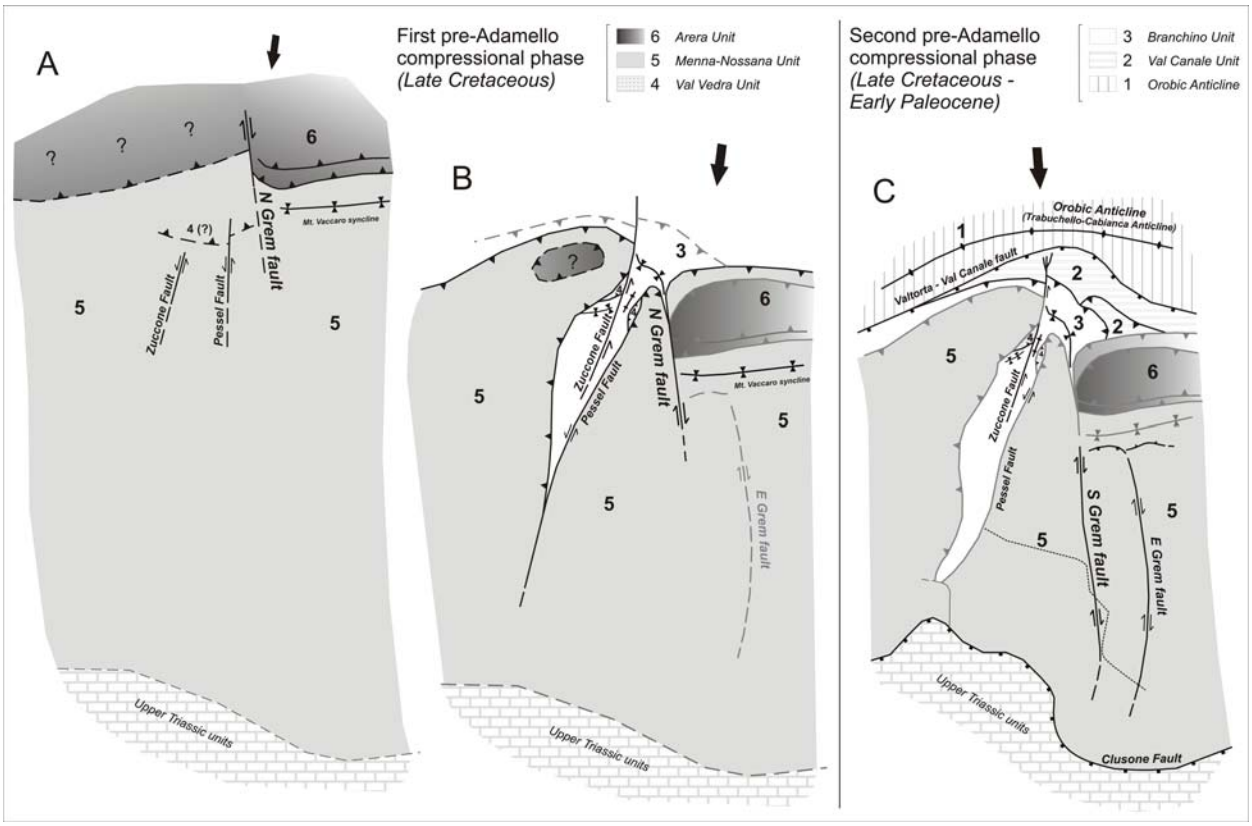

Figure 2.2.10 Reconstructed tectonic evolution of the GVTZ (D'Adda et al. submitted). Stage A: nucleation of the Grem fault on inherited a paleotectonic lineament related to the Mesozoic evolution of the Lombardian basin. Stage B: the growth of the GVTZ. The syn-thrust Corno Branchino syncline is distorted along the GVTZ in a dextral transpression. The indenter of unit 5, bounded by the Zuccone and the N Grem faults, formed during this deformation phase. Stage C: reactivation of the southern termination of the Grem fault propagating southward. The back-thrust of unit 5 on the Mt. Vaccaro syncline is accommodated by dextral and vertical displacement along the S- and E-Grem faults.

Second pre-Adamello compressional stage

A later compressive stage (Fig. 2.2.10c and Fig. 2.2.11c), with a different deformational style, occurred in the study area involving deeper structural levels of the belt. This event has been related with the

southward propagation of the Orobic Anticlines which form triangular fault zones wedged under the previous thrust sheets. The Orobic Anticlines are interpreted as ramp-folds coupled with the propagation of a deep thrust surface (Laubscher 1985; Schönborn 1992). Apparent N-verging back-thrusting and a general tilting of the Middle-Triassic carbonate units occurred during this second stage. Folding is especially evident along the forelimb of the Orobic Anticlines, where the the Valtorta - Val Canale fault steeply dips southward (i.e. cross sections in Fig. 2.2.4). Further south the Clusone fault was probably activated during the same stage (Fig. 2.2.10c and Fig. 2.2.11c), causing back-thrusting of the Upper Triassic units on the Middle Triassic ones (Zanchi et al. 1990a). This second compressive event is older than Middle-Late Eocene, since the westernmost of these three anticlines (Cedegolo Anticline) is clearly intruded by the south-western part of the Adamello batholith (Avio and Re di Castello units, Brack 1981, 1984), dating between 41 and 39 Ma (see Callegari and Brack 2002 for a summary). In the next paragraphs a Late Cretaceous age for this second step of shortening is also postulated (see also D'Adda et al. 2010).

The effects of the emplacement of the Trabuchello-Cabianca Anticline is evident in the northernmost part of the Lower to Middle Triassic thrust pile, which has been steeply uplifted and tilted southward along the Valtorta – Val Canale fault. Regional tilting of thrust planes is also evident southward, as all the main thrust surfaces gently dip to the south all across the study area.

We also suggest that back-thrusting of the Upper Triassic units along the Clusone fault, possibly following in time the formation of the Orobic Anticlines, produced a reactivation of discontinuities in the pre-existent thrust sheets, affecting especially the S-Grem fault and the SE sector of unit 5. Back-thrusting and out-of-sequence thrusting of the eastern portion of unit 5 over the Vaccaro syncline just north of Mt. Grem was probably related to a "buttress effect" given by the rigid mass of the Esino Limestones which forms this part of unit 5. Activation of these E-W trending back-thrust surfaces clearly post-dates the first pre-Adamello stage of thrust emplacement during which the Vaccaro syncline was formed. Deformation was partitioned along the S-Grem and E-Grem faults which propagated southward and may account for the activation of the E-W thrusts occurring just south of Alpe Arera. During this stage the Mt. Grem area was farther uplifted forming a positive structure with respect to the western portion of unit 5

No reactivation phenomena are evident north of Alpe Arera, as most of the displacement was accommodated along the southern branch of the Grem fault and along the E-W structures of Val Parina. This also accounts why the northern branch of the fault still preserves the structural setting achieved during the first deformational event.

2.2.6 Syn-thrust deformations in the GVTZ

The first description of the Grem fault was given by De Sitter and De Sitter-Koomans (1949) who interpreted the structural setting of Val Vedra in terms of horst and graben structures. Schönborn (1992) suggested a continuation of the transverse zone up to the Trabuchello-Cabianca Anticline through the whole Triassic thrust pile, considering the fault system as a post-thrusting feature caused by the north

directed indentation of a rigid wedge, respectively bounded by NW-SE and NE-SW dextral- and left-lateral strike-slip faults. He also interpreted the GVTZ as a transtensional fault system, since most of the faults apparently show normal offsets, as previously suggested by De Sitter and De Sitter-Koomans (1949). Our reconstruction supports a different tectonic scenario. All the analyzed N-S strike-slip faults display reverse motions with dip-slip or oblique components. In addition, N-S trending folds formed within unit 3 along the northern branch of the Grem fault as well as along Val Vedra, between the Zuccone and Pessel faults, indicate that the transverse zone was active during transpressional deformations associated to intensive folding and high-angle reverse motions (Fig. 2.2.2 and cross sections, F-F', G-G', H-H' in Fig. 2.2.6), rather than to a transtensional regime, as suggested by previous authors.

The Grem fault is the main structure of the GVTZ. It forms the lateral ramp of the higher units (unit 6 and eastern sector of unit 5) in the northern sector extending at depth across units 5 and 3 toward the south.

Spectacular transpressional deformations associated with the rotation of the Branchino syncline along the fault zone are exposed north of Alpe Arera along the north segment of the fault zone. South of Mt. Arera the deep ramp formed between units 3 and 5 exposed along the Riso-Parina tunnel is cross-cut by a vertical tear fault now representing the southern continuation of the S-Grem fault at the surface. This fault is associated to back-thrusting of the SE portion of unit 5 over the Vaccaro syncline, resulting in the formation of the Mt. Grem positive structure.

According to our model, the Grem fault progressively propagated from north to south, moving from higher to lower structural levels during the oldest pre-Adamello compressional stages which affect the entire Southern Alps. This demonstrates a close kinematic relationship between the thrust sequence and the GVTZ, indicating that it was a syn-thrust structure.

Our field data show that the N-Grem fault strongly interacted with the Corno Branchino syncline and produced the distortion of its geometry in a transpressional regime. The across-strike deflection of syn-thrust ductile structures, resulting in the alignment of fold elements (axial planes, axes, fold limbs) parallel to the shear direction provide crucial information for understanding the kinematics of the transverse zone. First, it represents the direct evidence that transverse zones are coeval with thrust faults since the ductile distortion of thrust-related folds can be explained only admitting a displacement activity already during the initial stages of thrusting and folding. Secondly, since distorted thrust-related folds can be considered as drag folds, they represent good kinematic indicators to investigate the shear sense of the transverse zone itself.

The second deformational stage is related to the emplacement of the Orobic Anticlines as fault-bend-folds and is testified by a marked tilting of the thrust planes at the base of the Lower to Middle Triassic imbricates, which generally dip southward in the whole area. Back-thrusting along the Clusone fault, which also preceded the emplacement of the andesitic dikes showing the same age of the Adamello pluton (see next paragraphs and D'Adda et al. 2010), was probably responsible for the reactivation, along the S-Grem fault, of the deep ramp between unit 3 and 5 as a superficial tear fault. Uplifting of the SE

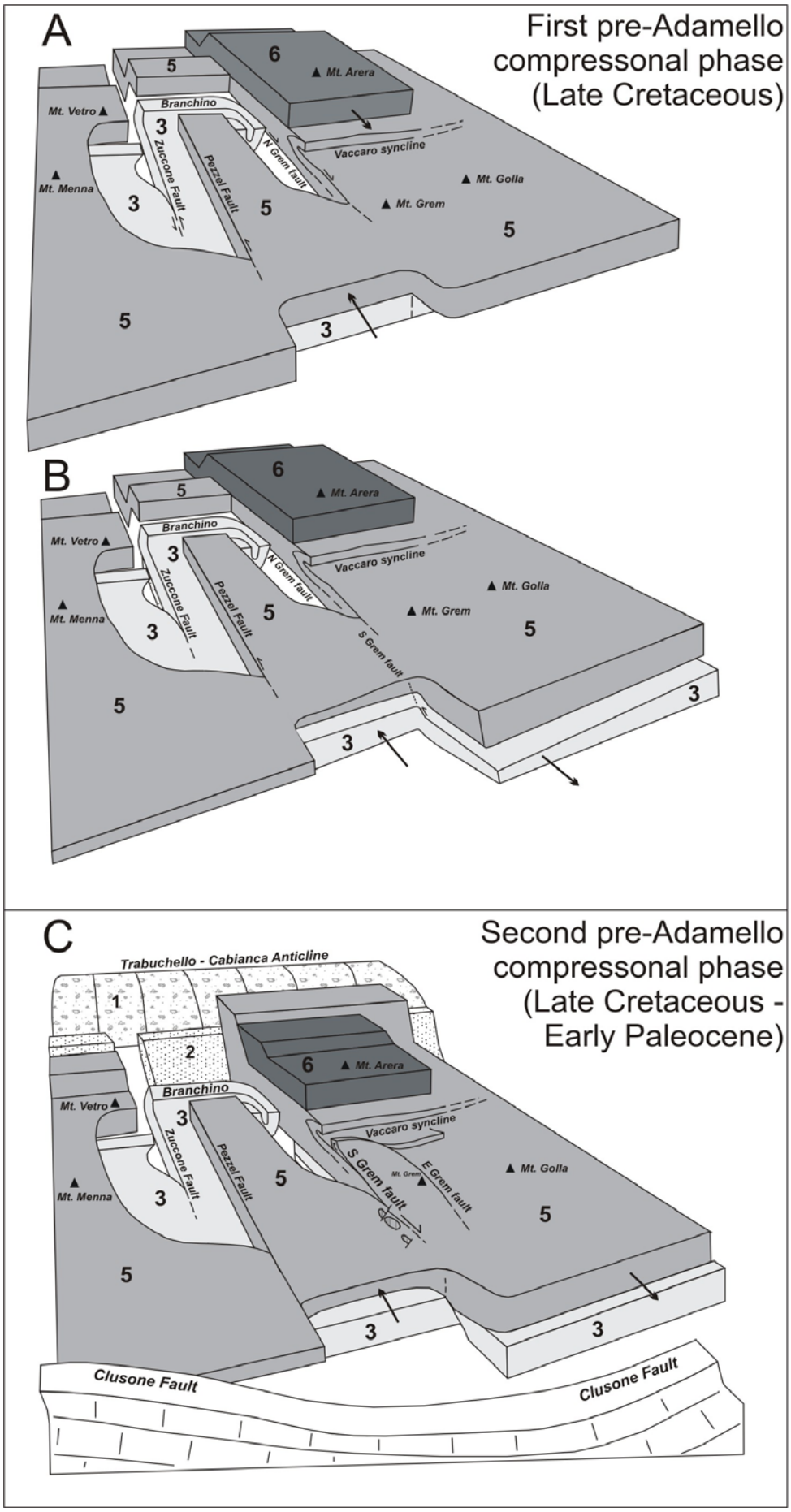

Figure 2.2.11 Block diagram visualization of the GVTZ evolution (D'Adda et al. submitted).

sector of unit 5 was due to oblique motion along the fault and to coeval back- and out-of-sequence thrusting along Val Parina.

Thomas (1990) provides a detailed description of possible controls on the location of transverse zones in thrust belts, such as the presence of deep pre-existing lineaments, pre-thrusting deformation of cover strata above deep faults or variations in mechanical stratigraphy. As the stratigraphy across the GVTZ does not change and considering the Mesozoic stratigraphic evolution of the Southern Alps, the best candidate for controlling the origin of the GVTZ can be identified in the presence of pre-existing lineaments. The Southern Alps have been affected by two major extensional events in the Norian (i.e. Jadoul et al. 1992) and Early Jurassic (i.e. Gaetani 1975, Winterer and Bosellini 1981) both responsible for the development of N-S normal faults which eventually led to the opening of the Alpine Tethys during Middle Jurassic. In the CSA, these faults are highlighted by rapid thickness and facies changes in the Norian and Early Jurassic succession. The vertical throw of these faults was consequently responsible for a displacement also in the underlying older units, which are now exposed in the study area. The presence of Norian and Early Jurassic faults in the younger units at the same longitude suggests that the effect of these faults was likely recorded also at deeper stratigraphic levels. Furthermore, the evidence of pre-compressional normal fault cutting the Ladinian-Carnian succession is observed in Unit 5, where the extensional Mt. Vetro fault (Fig. 2.2.6, section F-F' and G-G'), passively transported above the basal thrust of unit 5, can be referred to an extensional event predating the Cretaceous compression. The possible reactivation of pre-compressional N-S trending normal fault during the N-S compression is supported by the occurrence of Jurassic normal faults marking the western border of the Sebino through along the same longitude of the GVTZ, although at higher structural levels in the thrust stack exposed just south of the Clusone fault (Bersezio et al. 1997; Zanchi et al. 1990b). Faults along Val Seriana have also been deduced from the facies distribution of Lower Jurassic deposits (Zanchi et al. 2009) and through reconstruction of backstripping curves (Berra and Carminati 2010),. The reactivation of these Jurassic faults south of the Clusone fault during the Alpine compressions is also documented by the development of a deep graben in the Norian to Jurassic units along the left side of the lower Val Seriana (Zanchi et al. 1990b).

Observations in the study area coupled with the stratigraphic and tectonic setting of the CSA strongly support the hypothesis that the development of the GVTZ during the first stage of thrust stacking was controlled by the presence of pre-Cretaceous faults that, considering the regional setting were likely related to the Norian or Jurassic extension.

2.3 Relationships between thrusting and dyke emplacement in the Gandino and Presolana areas

2.3.1 Introduction

The Orobic Alps represent a key area to constrain the deformation history of the Southern Alps, thanks to the occurrence of dyke swarms intruding both basement and sedimentary cover units. The age of these dykes is still poorly constrained, due to the strong weathering and hydrothermal alteration. The available K/Ar and $^{40}Ar/^{39}Ar$ ages span between 64 and 35 Ma (Zanchi et al. 1990a; Fantoni et al. 1999).

In this chapter original field data from the Gandino area are combined with data from the Presolana area further north and the structural relationships between tectonic structures and magmatic bodies are described.

New SHRIMP U/Pb ages on zircon and fission track ages on apatite have been obtained from these magmatic rocks and will be presented in chapter 3. They constrain the relationships among tectonic activity, magmatism and exhumation in the Southalpine retro-belt, and provide crucial pinpoints for regional reconstructions during the early orogenic stages.

2.3.2 The Gandino area

Stratigraphic succession

The sedimentary succession of the Gandino area (Fig. 2.3.1) consists of upper Carnian to Late Norian units. The Carnian Castro Fm (Jadoul et al. 1991) consists of a lower member of bedded dolostones and 'carnieules', and an upper member of massive intraformational breccias. The Norian Dolomia Principale is the thickest (up to 1000 m) formation in the area. It consists of a basal unit reflecting lagoonal conditions, followed by inner-platform facies rocks. Intraplatform basinal facies suggest a fault-controlled transition from a Norian high to a basin, filled by 800-1000 m of dark, bedded limestones and dolostones named Dolomie Zonate and Zorzino Limestone (Jadoul et al. 1992; Berra and Jadoul 1996). Abrupt thickness and facies changes reflect extensional syndepositional tectonics (Jadoul et al. 1992; Berra and Carminati 2009), with a structural high in the Pizzo Formico area and coeval more subsiding zones in the Gandino-Endine zone (Berra and Jadoul 1991). Basinal limestones are covered along a sharp contact by the Riva di Solto Shale.

Tectonic units and regional structures

Detailed mapping and structural analysis led to the recognition of three main tectonic units, which are bounded by low-angle thrusts crosscut by high-angle extensional and strike-slip faults.

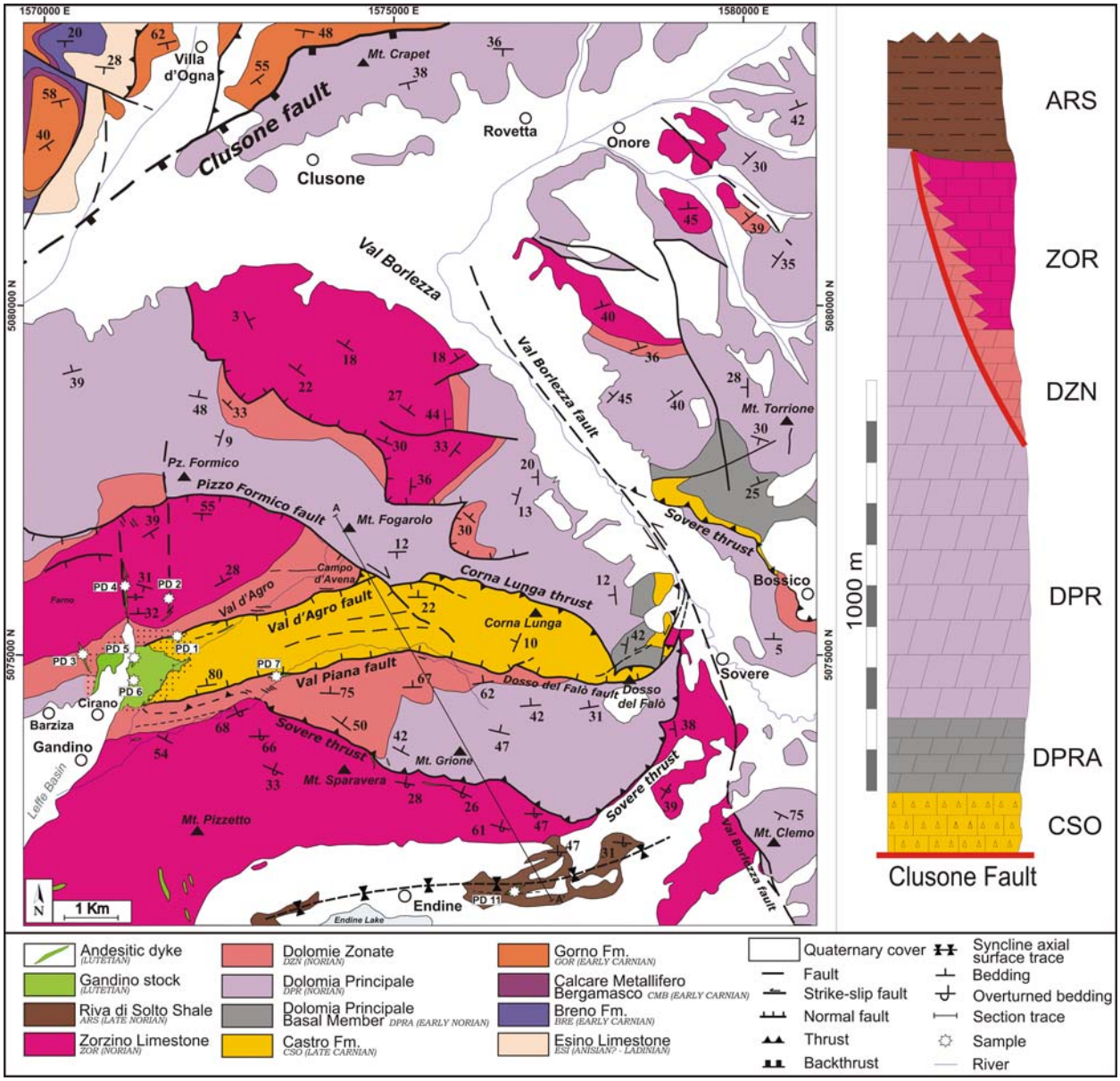

Fig. 2.3.1 Geological and structural map of the Gandino area, Orobic Alps (D'Adda et al. 2010). White stars indicate sampled dykes and subvolcanic bodies. Section trace refers to cross section in Fig. 2.3.3.

The structurally highest thrust sheet is the Corna Lunga unit, which is exposed along an E-W ridge between Gandino and Sovere (Figs. 2.3.1 and Fig. 2.3.2). It entirely consists of Castro Fm. rocks with a preserved thickness between 100 and 200 meters, folded to form an open syncline cut by E-W high-angle faults (Fig. 2.3.3). Well-bedded dolomitic limestones in the lowermost part of the unit indicate that its floor thrust developed below the basal strata of the Castro Fm. Well-bedded to vuggy dark dolomitic limestones are preserved at the base of the succession (lower Castro Fm.). The preserved thickness of this thrust sheet ranges between 100 and 200 meters. The floor thrust is preserved only in the NE sector of the unit (Fig. 2.3.1), and elsewhere it is cut and downthrown by high-angle E-W faults. The basal thrust is marked by a continuous, 50-80 cm thick, cataclastic zone slightly dipping to the south, along which the Corna Lunga unit was thrust onto the Norian succession of the intermediate thrust sheet. The southern boundary of the unit is marked by the ESE-WNW trending Val Piana fault, which joins eastward the

Dosso del Falò fault (Fig. 2.3.1). Both faults dip steeply to the north, and mainly show normal dip-slip movements. The Dosso del Falò fault turns from E-W, to the west, to NE-SW to the east, and displaces, with a left lateral throw, the underlying thrust units (Figs. 2.3.2 and Fig. 2.3.4). To the north, the Corna Lunga unit is bound by the ENE-WSW Val d'Agro fault, a steep south-dipping fault plane marked by discontinuous bands of cataclastic breccias. The eastern tip of the fault is displaced with a right-lateral

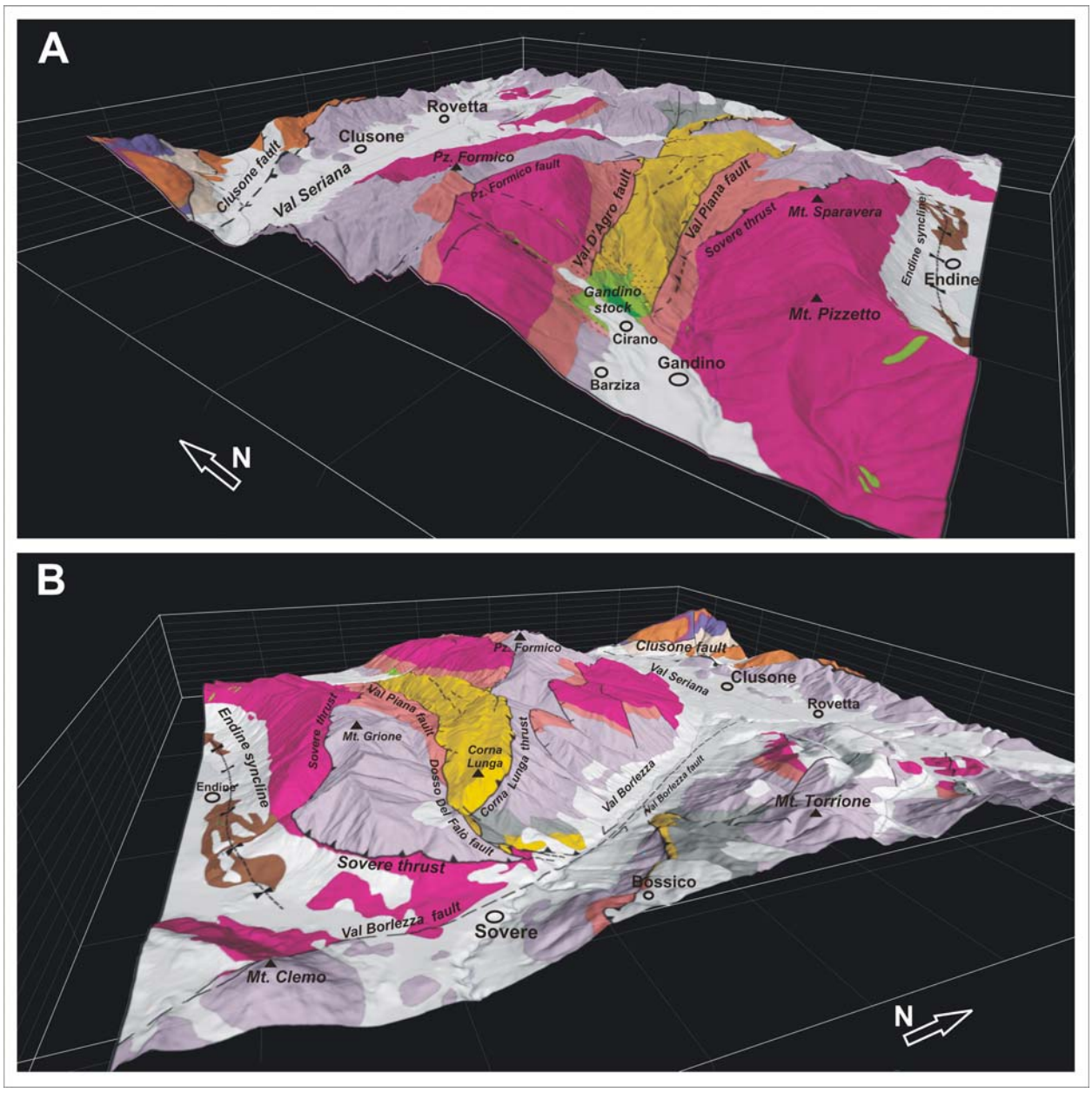

Fig. 2.3.2 3D-geological map of the Gandino area (D'Adda et al. 2010) performed with the 3D modelling software Move2009 (© Midland Valley Exploration). The model has been obtained projecting the geological map in Fig. 2.3.1 on a digital elevation model (DEM) of the topographic surface (re-sampled from the 20 m pixel size Digital Terrain Model of Regione Lombardia). A view from the west (A) of the study area clearly shows that the higher unit (Corna Lunga unit) has been lowered by the normal Val D'Agro and Val Piana faults, while a view from the east (B) highlights that also the Sovere thrust (Pizzo Formico unit) has been cut by normal faulting

offset by the NW-SE Pizzo Formico fault (Fig. 2.3.1).

The intermediate Pizzo Formico unit consists of the Dolomia Principale, Dolomie Zonate and Zorzino Limestone formations. The thickness of the Dolomie Zonate and Zorzino Limestone ranges, in this unit, between 100 m east of Gandino and up to 1000 m in the Pizzo Formico area, reflecting important

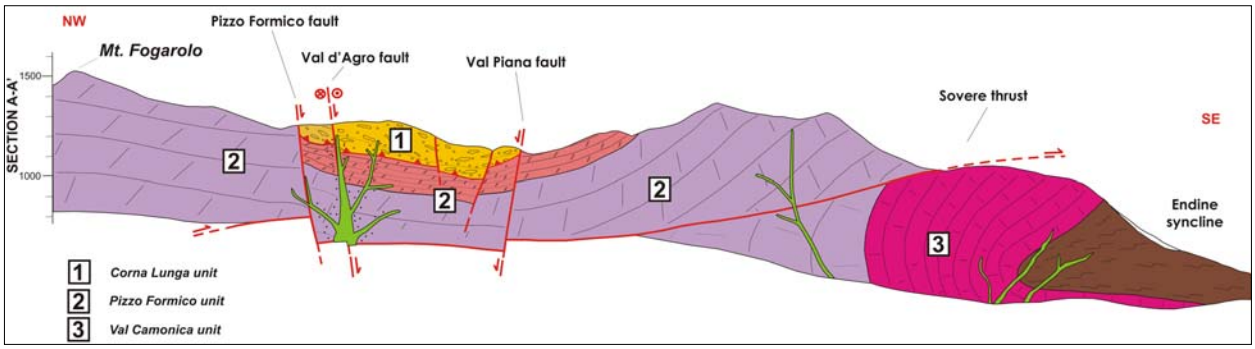

Fig. 2.3.3 NW-SE cross section through the Gandino area (D'Adda et al. 2010) showing the croscutting relationships between tectonic units, normal faults and dykes (section trace on map in Fig. 2.3.1)

differential subsidence during the Norian. This unit is soled by the E-W Sovere thrust (Fig. 2.3.3 and Fig. 2.3.4). This top-to-the-south thrust produced a repetition of the Norian succession, emplacing inner platform and

margin facies of the Dolomia Principale above the basinal units of the Zorzino Limestone and Riva di Solto Shale. North of Sovere, the thrust surface shows a ramp-and-flat configuration, whereas west of Sovere it forms a regular, low-angle north-dipping ramp. It is displaced by the left-lateral Val Borlezza fault, a NNW-SSE structure which also displaces the lowermost thrust sheet, and farther west also by the

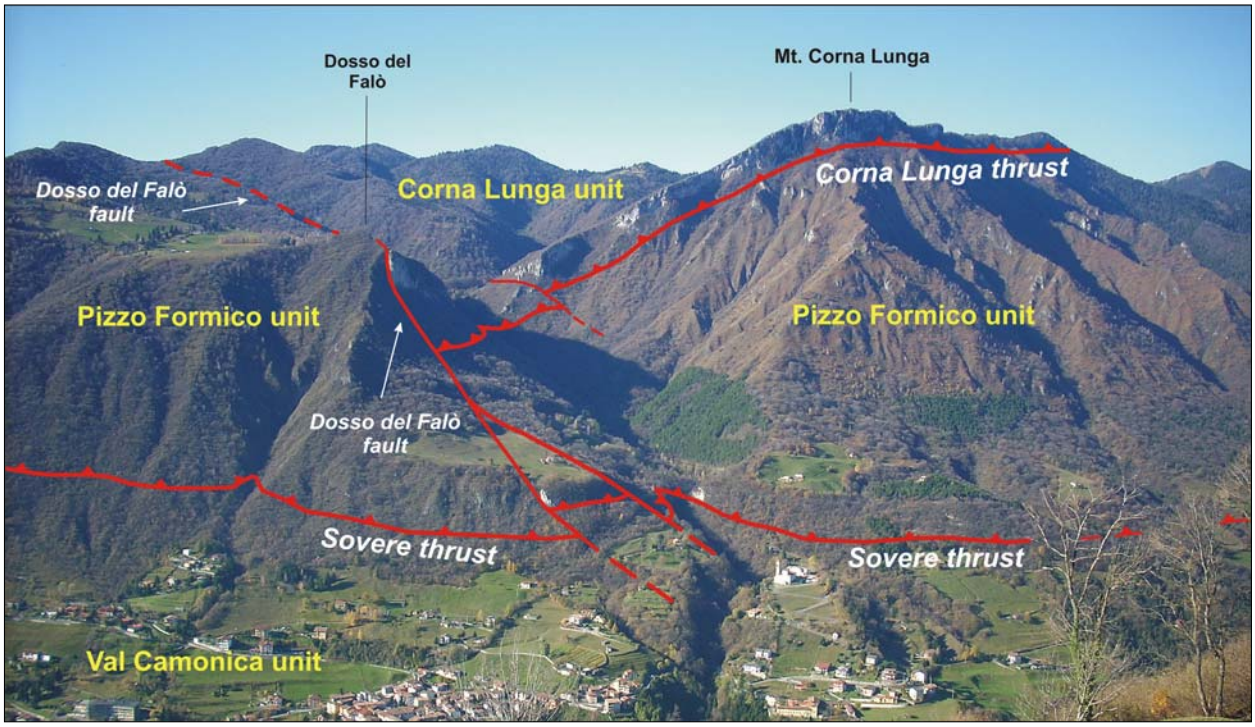

Fig. 2.3.4 Panoramic view of the western side of Val Borlezza near Sovere (D'Adda et al. 2010). The Dosso del Falò fault cuts and lowers the Corna Lunga thrust, also displacing the Sovere thrust.

Dosso del Falò fault (Figs. 2.3.2 and Fig. 2.3.4). The Sovere thrust is exposed eastward, out of the study area, and it acts as a detachment developed at the transition between the San Giovanni Bianco and the Castro Fms. This detachment surface merges with the Clusone fault at Giogo della Presolana (Berra et al. 1991).

The lower Val Camonica unit (corresponding to the "Parautoctono" of Gaetani and Jadoul 1979) forms the footwall of the Sovere thrust and includes, in our area, an Upper Triassic succession. East of the study

area, it is in stratigraphic continuity with the Permian to Middle Triassic succession exposed in the nearby Val Camonica (Berra et al. 1991). Within this unit, the E-W trending, overturned Endine syncline developed below the ramp of the Sovere thrust during the emplacement of the intermediate unit, attesting the southward movement of the hanging wall (Fig. 2.3.3). Cleaved Riva di Solto shales are exposed in the core of this fold near Endine. To the east this regional syncline is cut and partially dragged by the Val Borlezza fault.

Magmatic bodies

Several sets of dykes and a small hypabyssal, magmatic body intruded in the Gandino area. The Gandino stock (De Michele and Zezza 1973, 1978; Beccaluva et al. 1985) discontinuously crops out beneath the Pliocene-Quaternary deposits of the Leffe Basin (Ravazzi and Moscariello 1998), over an area of about

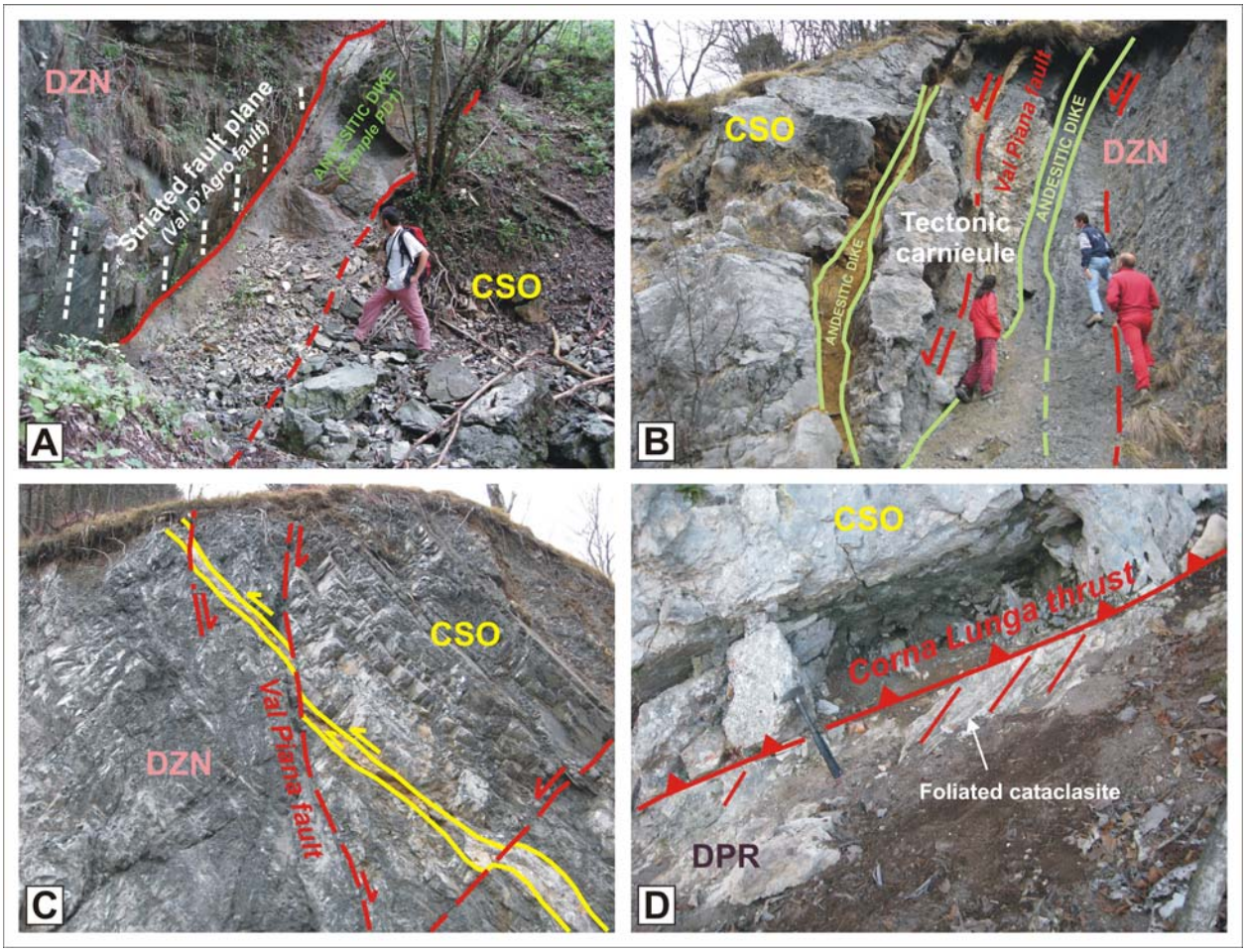

Fig. 2.3.5 Gandino area. (A) Striated fault plane of the normal Val D'Agro fault, parallel to a 2 meters thick andesitic dyke (Sample PD1, Fig. 2.3.1). The dyke appears to be essentially undisturbed, suggesting that the intrusion occurred towards the end of normal faulting. (B) Damaged zone along the Val Piana fault, east of Gandino. Dip slip indicators point to a normal faulting for this structure and the occurrence of undisturbed andesitic dikes along the fault indicates syn-fault magmatic activity under a local extensional regime. (C) Conjugate normal planes along the Val Piana fault crosscutting a duplex system. Reverse faults may be related to the western part of the old Corna Lunga thrust. (D) Corna Lunga thrust surface observed west of Sovere. The fault plane is marked by foliated cataclasite. Abbreviations: *CSO*, Castro Formation (late Carnian); *DPR*, Dolomia Principale (Norian); *DZN*, Dolomie Zonate (Norian). (D'Adda et al. 2010).

1,5 km^2 north-east of Gandino (Fig. 2.3.1). The inner part of the stock consists of holocrystalline quartz-andesite and gradually shows finer-grained porphyritic textures toward its rim, suggesting a shallow depth of emplacement. A 100 to 500 metres wide contact aureole, consisting of marbles, developed around the

stock (De Michele and Zezza 1978). This metamorphic overprint affects all the three tectonic units, testifying that they were already stacked at the time of the intrusion.

Several small andesitic dykes associated with the Gandino stock intruded the whole stack of thrusts (Fig. 2.3.1 and 2.3.3). They preferentially follow a ENE-WSW trend and are usually located along the main faults, pointing to a close relationship with them (Fig. 2.3.5A-B). These dykes have a thickness ranging from a few decimetres up to 4-5 metres, and commonly have a vertical attitude. They are generally undeformed, apart from minor reactivations of their margins with centimetric offset. They were thus emplaced during the final stages of activity of the normal faults that cut the imbricates. Other andesitic dykes north-east of Gandino define instead a radial pattern, probably related to the local stress field generated by the intrusion of the stock. One of them crosscuts, and thus post-dates, the core of the Endine syncline. Most of magmatic bodies in the Gandino area show a subsequent hydrothermal alteration.

Mesostructural analysis

A polyphase deformation history is documented by crosscutting relationships among thrusts, normal faults and magmatic bodies.

Mesostructural analyses were performed along the major normal faults of the Gandino area. Most of the measurement stations are located along the Val Piana and Val d'Agro faults, in order to define the kinematics of these structures, focusing on their relationship with the main thrust faults and magmatic bodies. Analyzed tectonic structures include striated and not striated faults, folds and axial-plane cleavage (Fig. 2.3.6). Crosscutting relationships among fault planes and/or striations allowed to define a relative chronology for the polyphase movements. In each site, the fault populations were tested for kinematic compatibility, in order to distinguish between fault associations in areas of complex deformation. Fault-slip data have been processed following the direct inversion INVD method (Angelier 1990) and iteration R4DT method (Angelier 1984). These methods assume that the shear stress applied to the fault plane is parallel to the slickenlines, allowing to determine the directions of principal stress axes ($\sigma_1 \geq \sigma_2 \geq \sigma_3$) as well as the magnitudes of principal stresses related to the reduced stress tensor. Between direct inversion and iteration method, the solution that minimized average and maximum values of ANG and RUP was chosen for each site. The results are summarized in Table 2.3.1.

The Val d'Agro fault runs from the Gandino stock to Campo d'Avena (Fig. 2.3.1). Its hanging wall, which consists of Castro Fm limestones belonging to the Corna Lunga (upper) unit, is lowered and brought into contact with the Carnian to Rhaetian succession of the underlying Pizzo Formico (intermediate) unit (Fig. 2.3.3 and Fig. 2.3.6). Several ENE-WSW striated fault planes have been measured along the fault zone (S1, S2, S3; Fig. 2.3.6A). Most of them show dip-slip or slightly oblique striations and frequently form conjugate systems of normal faults. Paleostress tensors obtained for these fault populations suggest an extensional regime, with subvertical σ_1 and subhorizontal NW-SE $\sigma 3$. Minor left-lateral reactivations were observed on the fault planes. The Val D'Agro fault is cut by the Gandino stock. Near its western tip, a small dyke intruded the fault plane (sample PD1, Fig. 2.3.1 and Fig.

2.3.5A). Except for minor normal or strike-slip reactivations along its margin, the dyke is undisturbed suggesting that it was emplaced during the final faulting stages. The Val Piana fault follows an ESE-

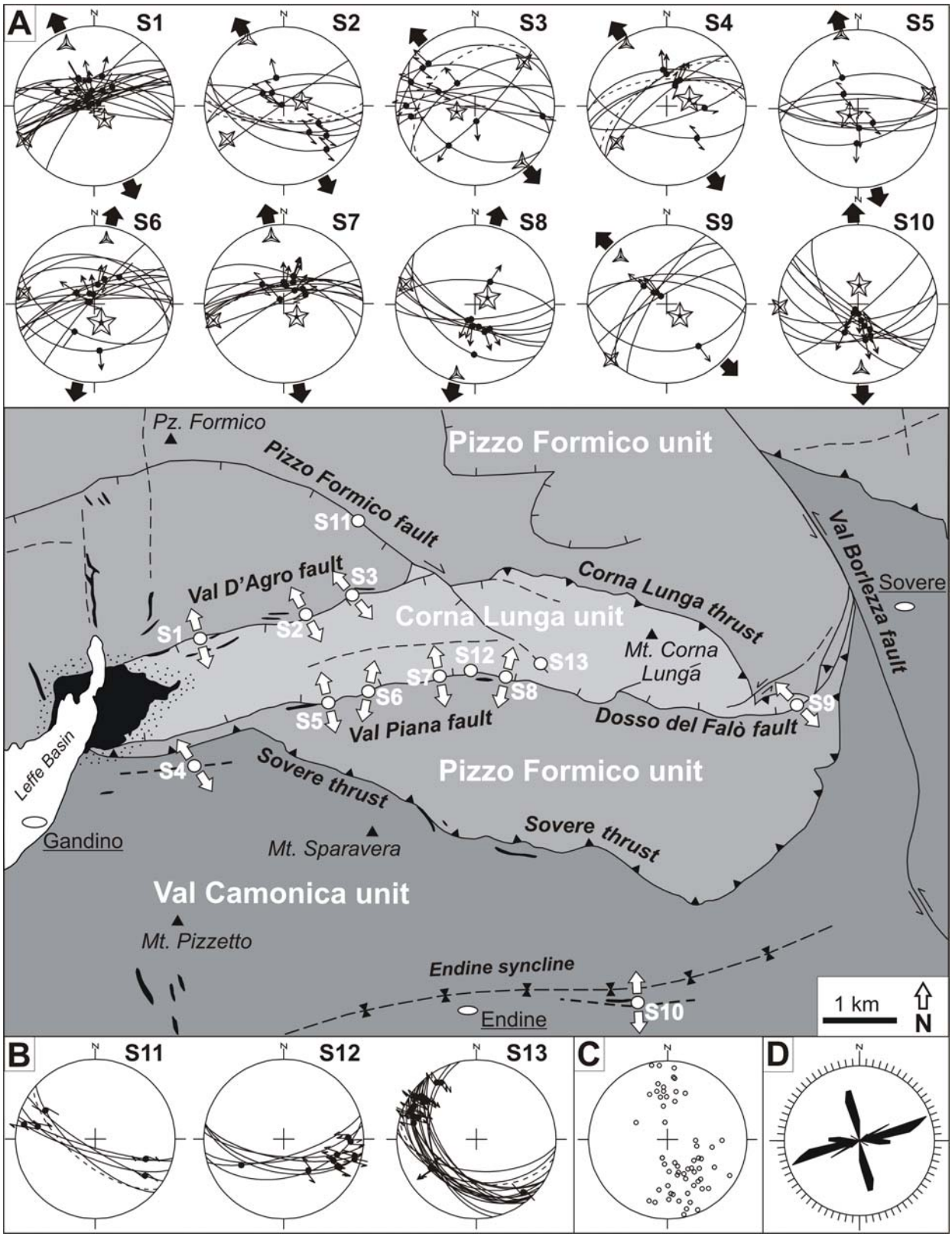

Fig. 2.3.6 Stereographic projections of faults planes and kinematic indicators measured in the Gandino area (D'Adda et al. 2010). Schmidt's projection lower hemisphere. (A) Paleostress analysis performed in 10 measuring stations allowed to calculate the directions of the main stress axes (see Tab. 2.3.1). σ_3 is always sub-horizontal with directions ranging from NNW to NNE, suggesting a N-S local extensional regime for the activation of Val D'Agro, Val Piana and Dosso del Falò normal faults. (B) Subsequent minor strike-slip reactivations occurred along these faults. They may be related to more recent compressional events which mainly affected the southern part of the Orobic sector. (C) Poles to axial plane cleavage measured west of Endine through Riva di Solto Shales, forming the core of the Endine syncline. (D) Rose diagram showing the main trends of andesitic dykes in the Gandino area

WNW trend from the Gandino stock to the Dosso del Falò fault (Fig. 2.3.1 and Fig. 2.3.6). Mesostructural analyses allow us to recognize different faults populations related to different tectonic events. Normal faults, with dip-slip to slightly oblique striations, often form conjugate systems. Locally, these faults displace mesoscale reverse faults related to early thrusting (Fig. 2.3.5C).

Paleostress tensors also suggest an extensional regime along the Val Piana fault, yielding a vertical σ_1 and a horizontal, N-NW directed σ_3 (S5, S6, S7, S8; Fig. 2.3.6A).The fault also presents later strike-slip reactivations (i.e. S12; Fig. 2.3.6B). The Val Piana fault is cut by the Gandino stock, and andesitic dykes were emplaced along the fault plane (Fig. 2.3.5B). Locally, dykes are cut by small normal faults parallel to the main extensional structures showing centimetre-scale offsets.

The Dosso del Falò fault is exposed between Val Borlezza and the Dosso del Falò. The fault plane dips about 70°-80° to the north, and separates the Corna Lunga (upper) unit from the Pizzo Formico (intermediate) unit. A few striations show dip-slip movements. Paleostress analyses indicate vertical σ_1 and NW-directed, horizontal σ_3 (S9, Fig. 2.3.6A).

The Pizzo Formico fault is exposed between Campo D'Avena and Pizzo Formico. This steep plane acted as a normal fault, and juxtaposes, within the Pizzo Formico unit, the Dolomia Principale and the basinal succession of Dolomie Zonate and Zorzino Limestone, which has been lowered to the south. Late dextral reactivation along this fault displaced the Val d'Agro fault (S11, Fig. 2.3.6B). Because it separates a Norian high to the north from a basinal area to the south, it can be interpreted as a reactivation of a Norian extensional fault.

Table 2.3.1 - Information on stress tensor determinations along normal faults in the Gandino area

Site	Method	N° of data	σ_1	σ_2	σ_3	Ratio	ANG		RUP		Fm.
			plunge/dip	plunge/dip	plunge/dip	φ	av(°)	M(°)	av(%)	M(%)	
S1	R	17	143/73	245/03	336/17	0,442	10	21	-	-	Castro Fm.
S2	R	8	107/73	225/08	317/14	0,275	11	21	-	-	Dolomie Zonate
S3	R	9	252/70	048/18	141/08	0,575	11	19	-	-	Dolomie Zonate
S4	I	7	074/65	232/23	326/08	0,265	8	16	33	53	Dolomie Zonate
S5	R	5	230/79	078/10	347/05	0,209	2	4	-	-	Dolomie Zonate
S6	I	10	160/69	278/10	012/18	0,045	10	24	29	54	Castro Fm.
S7	R	10	136/71	257/10	349/16	0,359	10	23	-	-	Castro Fm.
S8	I	7	062/74	286/11	194/11	0,356	8	16	27	48	Castro Fm.
S9	I	7	132/73	224/01	314/17	0,199	3	6	12	24	Castro Fm.
S10	I	10	003/71	268/02	177/19	0,281	8	17	23	43	Riva di Solto Shale

The following indications are reported: name of site (location in Fig. 8); inversion method: I (INVD), R (R4DT); number of data used for tensor calculation; plunge/dip of the main stress axes σ_1, σ_2, σ_3 ($\sigma_1>\sigma_2>\sigma_3$); ratio φ: $(\sigma_2-\sigma_3)/(\sigma_1-\sigma_3)$; average value av (°) and maximum value M(°) of ANG; average value av(%) and maximum value M(%) of RUP for solutions obteined with INVD; name of the formation (Fm). Numerical solutions have been accepted for average and maximum value of ANG respectively lower than 10-12° and 22-24°, and average and maximum value of RUP respectively lower than 35 and 55.

2.3.3 The Presolana area

Tectonic units and regional structures

The antiformal stack exposed in the Presolana area, between the eastern prolongation of the Val Canale fault to the north and the Clusone fault to the south, consists of three main tectonic units overlain by small klippen (Forcella 1988; Zanchi et al. 1990a). They include Olenekian to Carnian formations, consisting of thick shallow-water carbonate units interbedded with subordinate terrigenous deposits, basinal limestones and marls (Fig. 2.3.7).

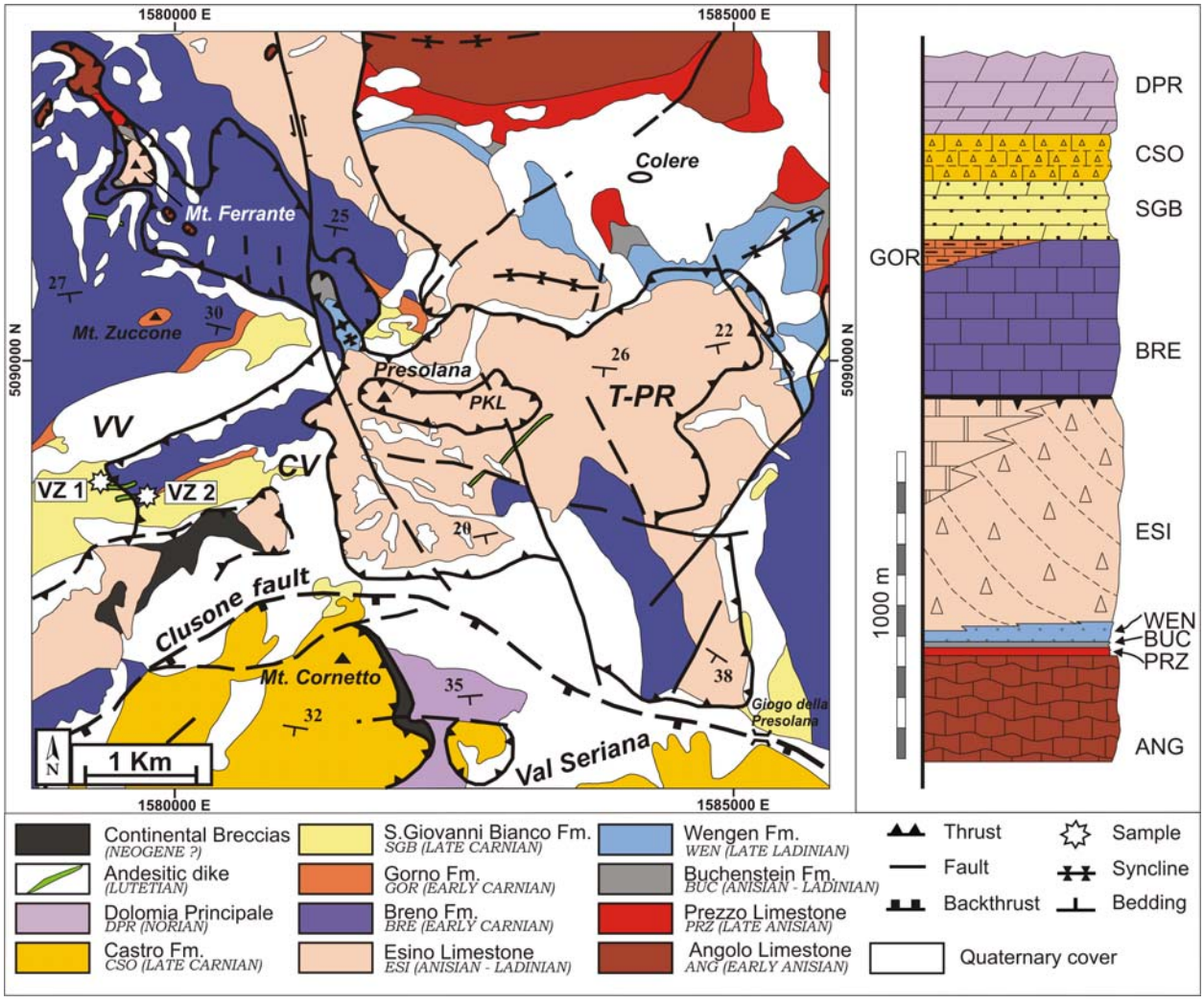

Fig. 2.3.7 Sketch map of the Presolana antiformal stack, Orobic Alps (D'Adda et al. 2010). The main thrust sheets of the stack are indicated: *PKL*, Presolana klippe; *T-PR*, Timogno-Presolana unit; *CV*, Creste di Valzurio unit; *VV*, Vigna Vaga unit. White stars indicate sampled andesitic dykes crosscutting the main thrust surfaces

The uppermost Timogno-Presolana unit consists of Anisian to lower Carnian rocks. Thin tectonic slices locally preserved on its top as klippen, at Mt. Presolana, Mt. Ferrante and Mt. Cavallo, are interpreted as tectonic doubling of this unit. The intermediate Creste di Valzurio unit consists of pervasively folded limestones of the Breno Fm (early Carnian) and also includes, west of Mt. Presolana, the Gorno and San Giovanni Bianco Fms (Carnian). The lower Vigna Vaga unit is made of a south-dipping succession spanning from the Olenekian Carniola di Bovegno to the lower Carnian San Giovanni Bianco Fm.

Kinematic indicators along thrust surfaces, as well as the overturned asymmetric folds in their footwall,

suggest southward imbrication of these thrust sheets, as also confirmed by the up-section propagation of the thrust surfaces (see Forcella 1988, Zanchi et al. 1990a or Forcella and Jadoul 2000 for further details). Close to the Clusone fault, thrusts dip to the south and the whole stack is underthrust below the Upper Triassic thrust sheets exposed south of this structure (Zanchi et al. 1990a). Axial plane cleavage and widespread calc-mylonites, which formed from Esino Limestone and Breno Fm, occur along the main thrust surfaces.

Magmatic bodies

The southern portion of the Presolana thrust stack is intruded by a swarm of E-W to ENE-WSE trending dykes. They have a thickness ranging from a few decimetres up to 2 metres, and are subvertical.

In the upper Valzurio Valley, dykes crosscut the folded thrust surface between the Creste di Valzurio (intermediate) and the Vigna Vaga (lower) units (Fig. 2.3.7 and 2.3.8). E-W normal faults cut such intrusions displacing them with metric offsets (Fig. 2.3.8). These minor structures were probably associated with the same stress regime responsible for dyke emplacement.

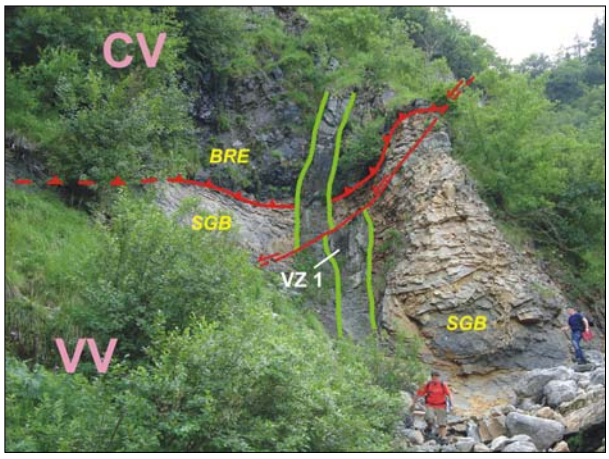

Fig. 2.3.8 Presolana area. Subvertical dyke crosscutting the thrust surface between Vigna Vaga and Creste di Valzurio units (Sample VZ1; see also Fig. 2.3.7). Both thrust surface and dyke are slightly displaced by a minor normal fault. Abbreviations: *BRE*, Breno Formation (early Carnian); *SGB*, San Giovanni Bianco Formation (late Carnian); VV, Vigna Vaga unit; CV, Creste di Valzurio unit. (D'Adda et al. 2010).

2.3.4 Petrography and geochemistry of magmatic bodies

The core of the Gandino stock has a medium-grained granular texture grading into porphyritic towards the margins. The dykes and the marginal parts of the stock are fine-grained and show a magmatic foliation marked by the shape preferred orientation of amphibole and plagioclase. Foliation in dykes is typically parallel to the dyke margins and to fault planes, which represented the preferential ways for magma ascent. The original magmatic assemblage, when preserved from hydrothermal alteration, consists of plagioclase, green to pale green amphibole and rare biotite phenocrysts. Quartz phenocrysts, mainly in polycrystalline aggregates, occur in some samples. The groundmass is formed by microcrystalline plagioclase and quartz. Plagioclase phenocrysts are euhedral in shape and show albite twinning and normal zoning (30-20 An%). The plagioclase in the matrix and the rims of phenocrysts have a similar composition. Some amphiboles show preserved brown cores, and are surrounded by thin biotite rims. Accessory minerals are apatite, zircon and various sulphides and oxides.

The mineralogical composition of the Presolana dykes is quite different from the Gandino ones. Quartz and biotite are lacking, and the magmatic foliation is less apparent. The magmatic assemblage consists of

Table 2.3.2 - Whole rock geochemical data

	PD1	PD6	PD7	PD11	VZ1	VZ2
SiO_2	58,85	58,41	57,67	56,45	51,78	53,28
Al_2O_3	17,93	18,61	19,38	18,29	17,23	17,08
Fe_2O_3	5,21	5,39	5,50	5,63	7,03	6,30
FeO*	4,69	4,85	4,95	5,07	6,33	5,67
MgO	2,48	2,94	2,49	3,55	5,74	5,32
CaO	6,68	7,43	7,56	6,44	5,36	6,20
Na_2O	2,78	3,23	3,07	3,55	3,56	3,72
K_2O	0,53	0,94	0,52	0,22	2,22	1,82
TiO_2	0,45	0,46	0,47	0,47	0,80	0,75
P_2O_5	0,16	0,12	0,14	0,14	0,13	0,15
MnO	0,15	0,14	0,15	0,14	0,11	0,11
LOI	4,7	2,2	2,9	4,9	5,8	5,0
ASI	1,04	0,94	1,00	1,03	0,96	0,88
Ba	175	213	151	91	242	296
Rb	9,2	22,5	6,8	5,2	48,7	37,9
Sr	401,7	448,5	456,3	596,7	700,1	623,8
Sc	15	20	19	25	33	28
Cs	0,3	0,4	0,1	0,4	2,3	1,8
Ga	16,9	17,8	17,6	16,6	17,0	16,6
Zr	75,6	81,9	62,1	58,4	67,2	68,4
Hf	2,2	2,1	2,0	2,1	1,8	2,1
Y	14,4	13,9	15,8	13,8	15,5	14,2
Nb	3,9	3,4	3,1	2,4	7,3	8,3
Ta	0,2	0,2	0,1	0,2	0,5	0,6
V	131	139	149	171	251	204
Co	9,2	13,0	9,9	13,1	23,3	20,9
Ni	2,2	5,1	3,1	5,7	26,3	23,9
U	1,3	0,7	0,9	0,4	2,2	2,6
Th	3,5	3,5	4,9	2,5	7,8	9,1
Pb	0,9	1,2	1,3	2,4	1,0	1,3
La	11,4	12,0	13,8	7,7	20,1	23,1
Ce	22,7	23,0	24,4	17,6	35,6	38,1
Pr	2,85	2,83	2,83	2,17	4,01	3,98
Nd	11,7	11,4	11,3	8,9	15,1	15,1
Sm	2,29	2,29	2,18	1,97	2,94	2,65
Eu	0,69	0,73	0,71	0,67	0,92	0,83
Gd	2,14	2,25	2,15	2,09	2,75	2,55
Tb	0,37	0,39	0,39	0,37	0,47	0,42
Dy	2,19	2,22	2,43	2,12	2,71	2,38
Ho	0,48	0,45	0,52	0,46	0,54	0,49
Er	1,50	1,36	1,56	1,44	1,60	1,41
Tm	0,24	0,23	0,27	0,18	0,25	0,22
Yb	1,63	1,47	1,77	1,48	1,56	1,41
Lu	0,26	0,23	0,28	0,24	0,23	0,21
Eu/Eu*	0,95	0,98	1,00	1,01	0,99	0,97

Notes: Major and minor elements in wt%, whereas trace in ppm; FeO*=Fe_2O_3x0.8998; Eu/Eu*=$Eu_N/\sqrt{(Sm_N+Gd_N)}$; LOI = Loss on Ignition; ASI = Alumina Saturation Index

plagioclase, clinopyroxene and brown to deep-green amphibole as phenocrysts. Small titanite crystals occur in the groundmass.

Dyke rocks were affected to varying degree by secondary processes that modified their chemical composition. Most of the samples yielded elevated Loss On Ignition (LOI) values (Table 2.3.2). Because of the correlation between LOI and major "mobile" elements, which suggests a general alteration, our discussion is largely based on the least mobile trace elements. The Gandino samples range in composition from quartz-andesite to dacite/rhyodacite (Fig. 2.3.9A) with a low to medium-K calc-alkaline affinity, and 0.9 to 1.04 ASI (Alumina Saturation Index) values (Table 2.3.2).

The dykes from the Presolana area are less differentiated than the Gandino dykes, and are mainly metaluminous basalts or andesitic basalts (ASI = 0.88-0.96) (Fig. 2.3.9A). They differ from the Gandino samples also in their higher K_2O content, which points to high-K calc-alkaline affinity. In the multi-element spider diagram normalized to primitive mantle (Fig. 2.3.9B; McDonough and Sun 1995), all samples display similar patterns characterized by an enrichment in Th, U, Pb and LREE (La, Ce, Nd) relative to Nb and Ta negative spikes, Ti depletion relative to Zr, slight positive Zr-Hf anomalies and flat HREE patterns. These geochemical features are typical of calc-alkaline volcanic rocks. Compared to primitive mantle, the Gandino samples are more depleted in Th, U, La, Ce, Ta, Nb and Ti than the Presolana ones.

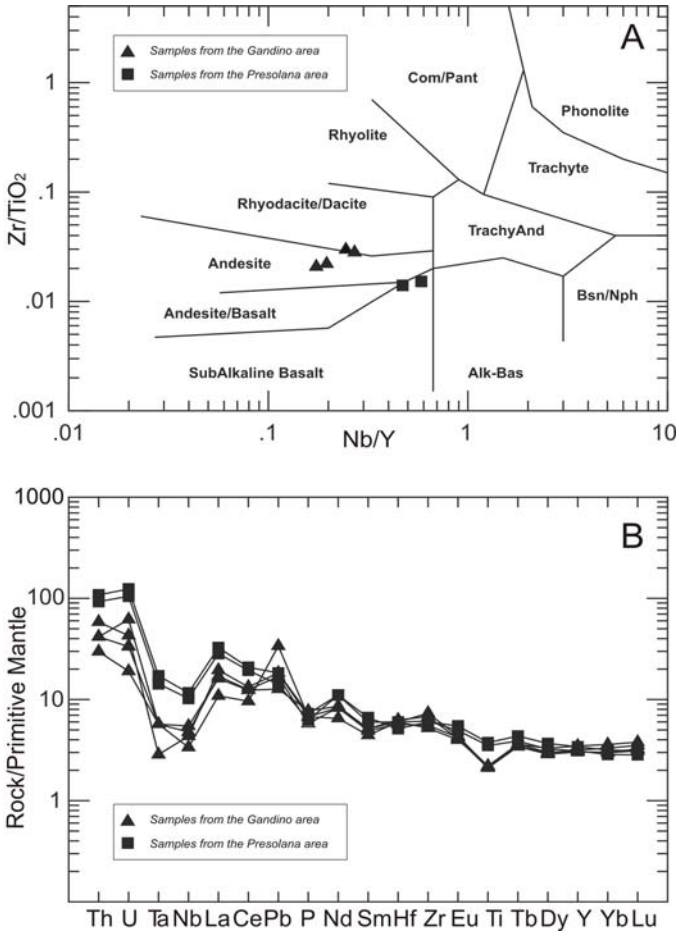

Fig. 2.3.9 (A) Zr/TiO_2 vs Nb/Y classification diagram (Winchester and Floyd 1977) for the investigated samples from Gandino and Presolana areas. (B) Primitive mantle-normalized incompatible element diagram (McDonough and Sun 1995) for samples from the Gandino and Presolana areas. (D'Adda et al. 2010).

2.3.5 Relative chronology between thrusting, faults and dykes

In the Gandino area, the upper Carnian to Rhaetian succession is stacked into three main tectonic units (Corna Lunga, Pizzo Formico and Valcamonica units from top to bottom) bound by south-verging low-angle thrust faults (Corna Lunga and Sovere thrusts), which are in turn crosscut by high-angle extensional and strike-slip faults.

Field relationships and mesostructural analysis allowed the recognition of a relative chronology for the thrust stack evolution. During the first thrusting event, the Corna Lunga unit, mainly consisting of now preserved Carnian Castro Fm. (Jadoul et al. 1991), was thrust onto the Norian succession of the Pizzo

Formico unit. These units were later displaced together southward onto the Upper Triassic succession of the Val Camonica unit. Deformation was strongly partitioned in the footwall during this second thrusting stage, leading to the formation of the overturned Endine syncline. Local extension after thrust stacking caused the activation of high-angle extensional faults (e.g. Val d'Agro and Val Piana faults), which crosscut and partly reactivated the original thrust contacts (Fig. 2.3.10). Later shortening caused minor strike slip reactivations along these high-angle surfaces together with the activation of secondary reverse faults characterized by small throws. In our interpretation, the Corna Lunga unit represents a klippe of the structurally highest thrust sheet of the belt, so far considered almost completely eroded in the Orobic Alps south of the Clusone fault (Schönborn 1992; Forcella and Jadoul 2000).

In the Presolana area, the south-verging thrust stack consists of three tectonic units: the Timogno-Presolana (upper) unit (Anisian to lower Carnian formations), the Creste di Valzurio (intermediate) unit (Carnian formations) and the lowermost Vigna Vaga unit (Olenekian to lower Carnian formations). Several small klippen representing tectonic doublings of the Timogno-Presolana units are preserved on its

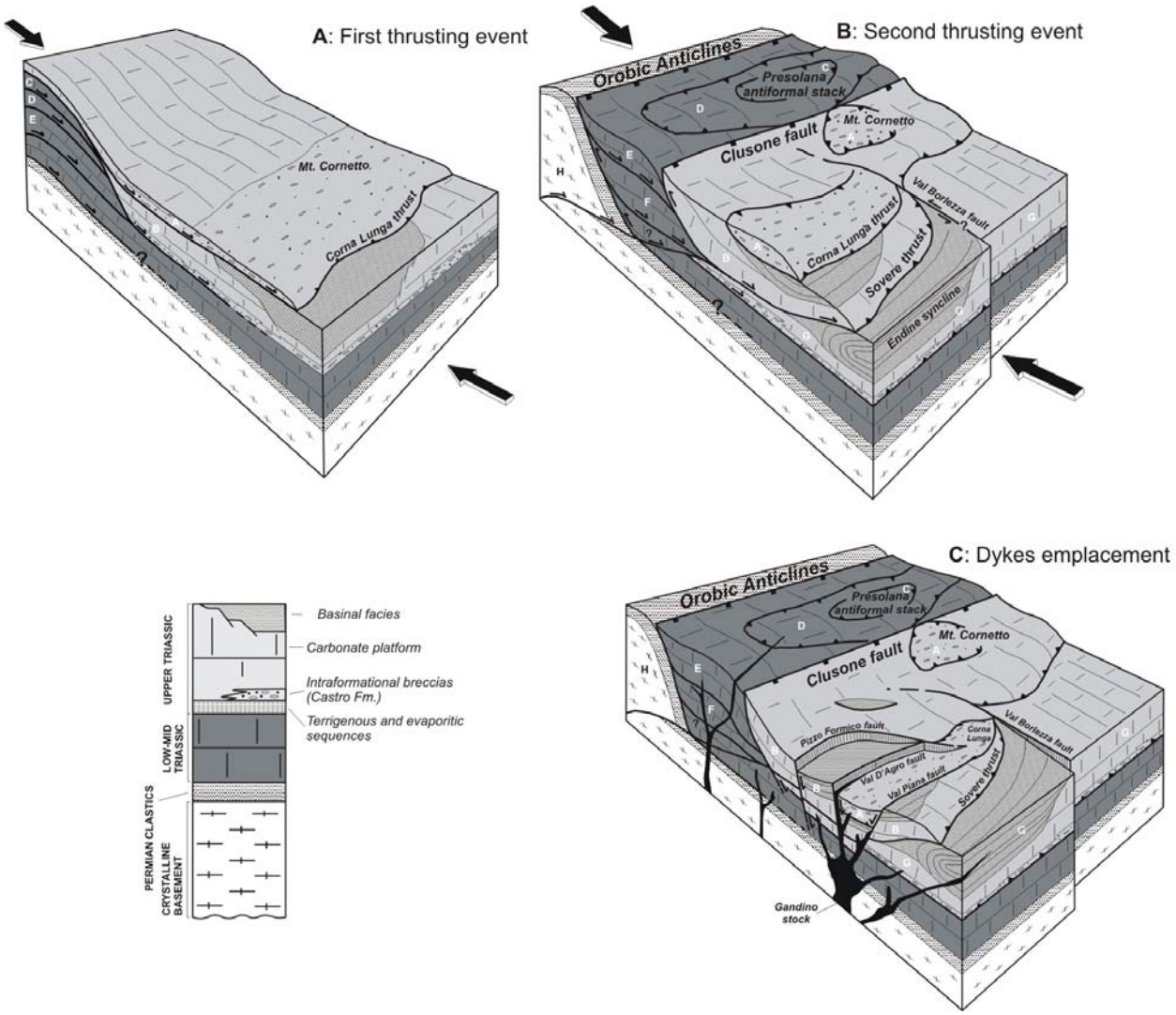

Fig. 2.3.10 Simplified reconstruction of the evolution of Gandino and Presolana areas during pre-Adamello compressional stages of Alpine tectonics (modified from D'Adda et al. 2010): *A*, Corna Lunga unit; *B*: Pizzo Formico unit; *C*: Presolana klippe; *D*: Timogno-Presolana unit; *E*: Creste di Valzurio unit; *F*: Vigna Vaga unit; *G*: Val Camonica unit; *H*: Orobic Anticlines system.

top. Like in the Gandino area, structural analyses document a polyphase in-sequence south-verging thrust propagation (Forcella et al. 1988; Zanchi et al. 1990a; Forcella and Jadoul 2000).

The relative chronology established for the evolution of the Gandino and Presolana thrust stacks is in agreement with the general model of Schönborn (1992), who proposed the occurrence of two separate thrust systems in this sector of the CSA. According to our model, the first compressive event was characterized by large horizontal displacements and significant crustal shortening and thickening. This event corresponds to the emplacement of the Orobic thrust sheet ("thrust sheet 1" in Schönborn 1992), and gave origin to the upper units of the south-verging thrust stacks exposed north of the Clusone fault. Our interpretation of the Corna Lunga unit implies that tectonic slices belonging to the Orobic thrust sheet are still preserved south of the Clusone fault (Fig. 2.3.10A). The second thrusting phase is instead related to the out-of-sequence southward propagation of the Orobic Anticlines system, which occurred along deep-seated thrusts located beneath the older stacks. During this second phase, the Corna Lunga-Pizzo Formico imbricate was thrust onto the Val Camonica unit. In the Presolana area, the upper and intermediate units were initially thrust onto the lowermost Vigna Vaga unit, and the entire thrust stack was then folded and underthrust below the Clusone fault. Back-thrusting along the Clusone fault concurrently occurred with southward stacking of thick slices of Upper Triassic units along the Sovere thrust system, which represents the southern continuation of the same detachment surface (Fig.2.3.10B).

Chapter 3

GEOCHRONOLOGICAL CONSTRAINTS FOR ALPINE TECTONICS IN THE CENTRAL SOUTHERN ALPS

3.1 $^{40}Ar/^{39}Ar$ dating of fault-related pseudotachylytes along the Orobic and Porcile thrusts

3.1.1 The $^{40}Ar/^{39}Ar$ method applied to pseudotachylytes: assumptions and problems

Coseismic slip along fault planes releases frictional heat which could trigger melting of the host rock across a few millimetres to some centimetres wide zone adjacent to the slip surface. Since minerals have different melting points and mechanical strength, they can react to frictional heating with different behaviours (Spray 1992). Hydrous minerals as amphiboles and micas have a lower melting temperature and yield strength with respect to quartz and feldspars and are therefore preferentially consumed during frictional melting (Spray 1992). The melt origin implies that they are generated in a high temperature process, that is able to re-equilibrate the isotopic system.

Isotope dating techniques applied on pseudotachylytes relate on Rb-Sr (Müller et al. 2002; Petermann et al. 1989) and $^{40}Ar/^{39}Ar$ systems (Kelley and Spray 1997; Magloughlin et al. 2001; Pennacchioni et al. 2006; Sherlock et al. 2009). The K-Ar isotopic system is the most suited to attempt isotopic dating of pseudotachylytes if K-bearing minerals (i.e. micas and amphiboles) are involved in the melting process (Müller et al. 2002).

Two major problems are related to $^{40}Ar/^{39}Ar$ dating of pseudotachylytes. The first crucial assumption is that all the radiogenic Ar contained in the melting minerals escapes the system and that accumulation of "new" radiogenic Ar starts just after quenching. Since melting and subsequent cooling last 10^1 to 10^3 s (Spray 1987), $^{40}Ar/^{39}Ar$ ages are considered to reflect the crystallisation age of pseudotachylytic melts. However, not all the inherited ^{40}Ar can escape the melt, since the melting-cooling process has a too short duration, and this made difficult the dating of pseudotachylytes (Sherlock et al. 2009).

The second problem related to pseudotachylyte dating is the common occurrence within pseudotachylyte veins of a variable amount of inherited clasts/minerals older than the pseudotachylyte itself. The occurrence of undetected mixed mineral generations would lead to systematic inaccuracies in dating (Müller et al. 2002; Vance et al. 2003). To overcome this problem and interpret the complex interplay of alteration phases, matrix, and clasts, it is necessary and sufficient to identify mixing end-members by chemical correlation diagrams and relate the inferred end-members to chemical analyses (Müller et al. 2002). The recognition of the distinct chemical reservoirs activated during stepwise heating experiments is made possible with the correlation between Ca/K and Cl/K ratios derived from Ar mass spectrometry and EMPA (Electron Microprobe analysis) analyses. In this way each gas release step related to alteration phases, pseudotachylyte matrix and microlites, and inherited clasts can be recognized (Müller et al. 2002).

3.1.2 $^{40}Ar/^{39}Ar$ results

For all samples the Ar isotopic data can be interpreted as gas release from different mineral reservoirs and from their mixtures (Müller et al. 2002; Vance et al. 2003; Villa et al. 2000) as suggested by the comparison between the Ca/K release patterns, calculated from the $^{37}Ar/^{39}Ar$ ratios, and the apparent age

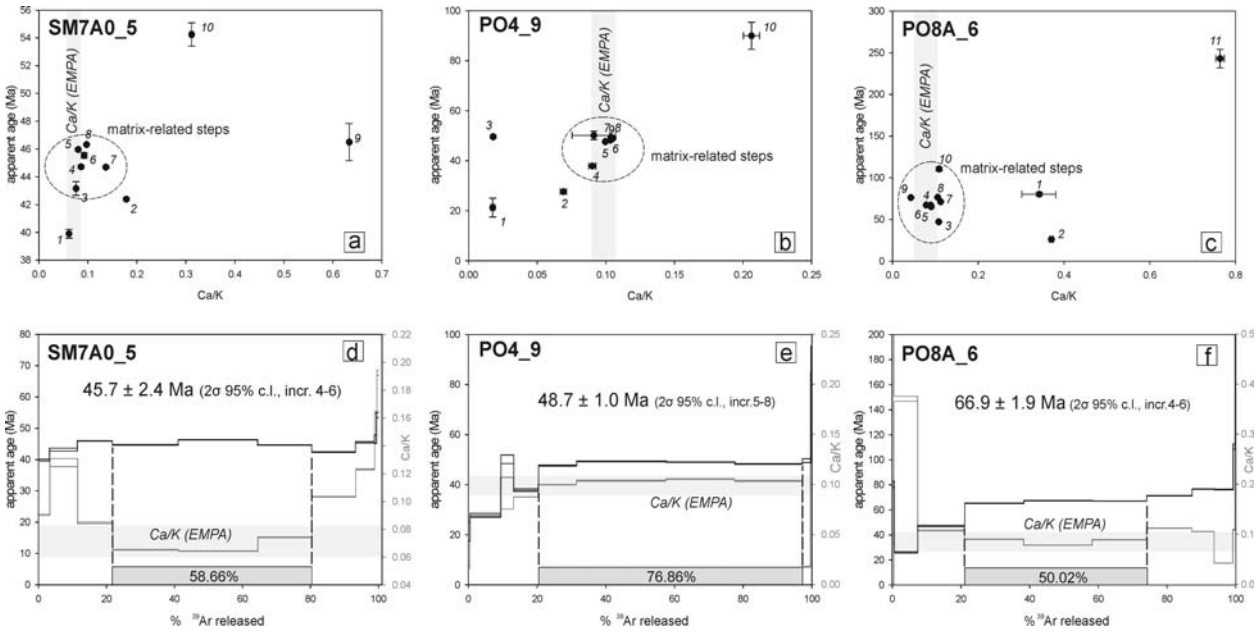

Fig. 3.1.1 $^{40}Ar/^{39}Ar$ stepwise heating experiments results of three representative pseudotachylyte samples (Zanchetta et al. 2010). The correlation between age and Ca/K ratios identifies several steps as matrix degassing, mainly on the base of the similarity between the Ca/K ratio determined by $^{37}Ar/^{39}Ar$ and the EMP measured Ca/K values. Low ^{39}Ar amounts released at high temperature steps indicate that the importance of clasts is subordinate. This is a positive result of our microCT screening. Analytical data and additional Ca/K versus apparent age diagrams are reported in Table 3.1.3 and Fig. 3.1.3.

spectrums (Fig. 3.1.1, Fig. 3.1.2 and Fig. 3.1.3).

All the gas release pattern display similar features. Low temperature steps (1 to 3) have isotopic Ca/K values that differ from Ca/K values of EMPA analyses. These devious Ca/K values can be correlated to the presence of secondary or alteration mineral phases, such as chlorite, calcite and clay minerals, also observed in thin section. Therefore their ages are geologically meaningless.

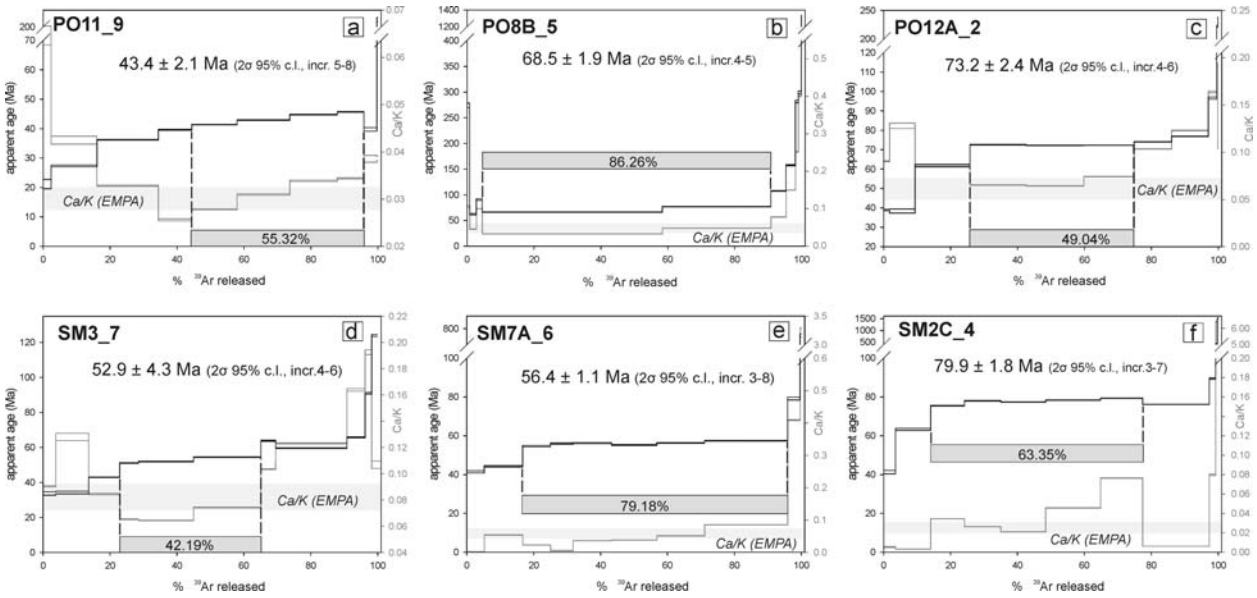

Fig. 3.1.2 Age spectra of remaining six samples (Zanchetta et al. 2010).

At intermediate temperatures, age spectra show a flat trend which generally corresponds to homogeneous Ca/K values (within the analytical errors) within or very close to the chemical composition of the pseudotachylyte matrix determined by EMPA analyses. Exceptions are represented by samples PO11_9, SM7A_6 and SM2C_4 (Fig. 3.1.2a-e-f and Fig. 3.1.3), which display different and inhomogeneous Ca/K ratios for matrix-related steps. This feature is probably due not only to analytical errors, as a chemical heterogeneity of the matrix should also be considered.

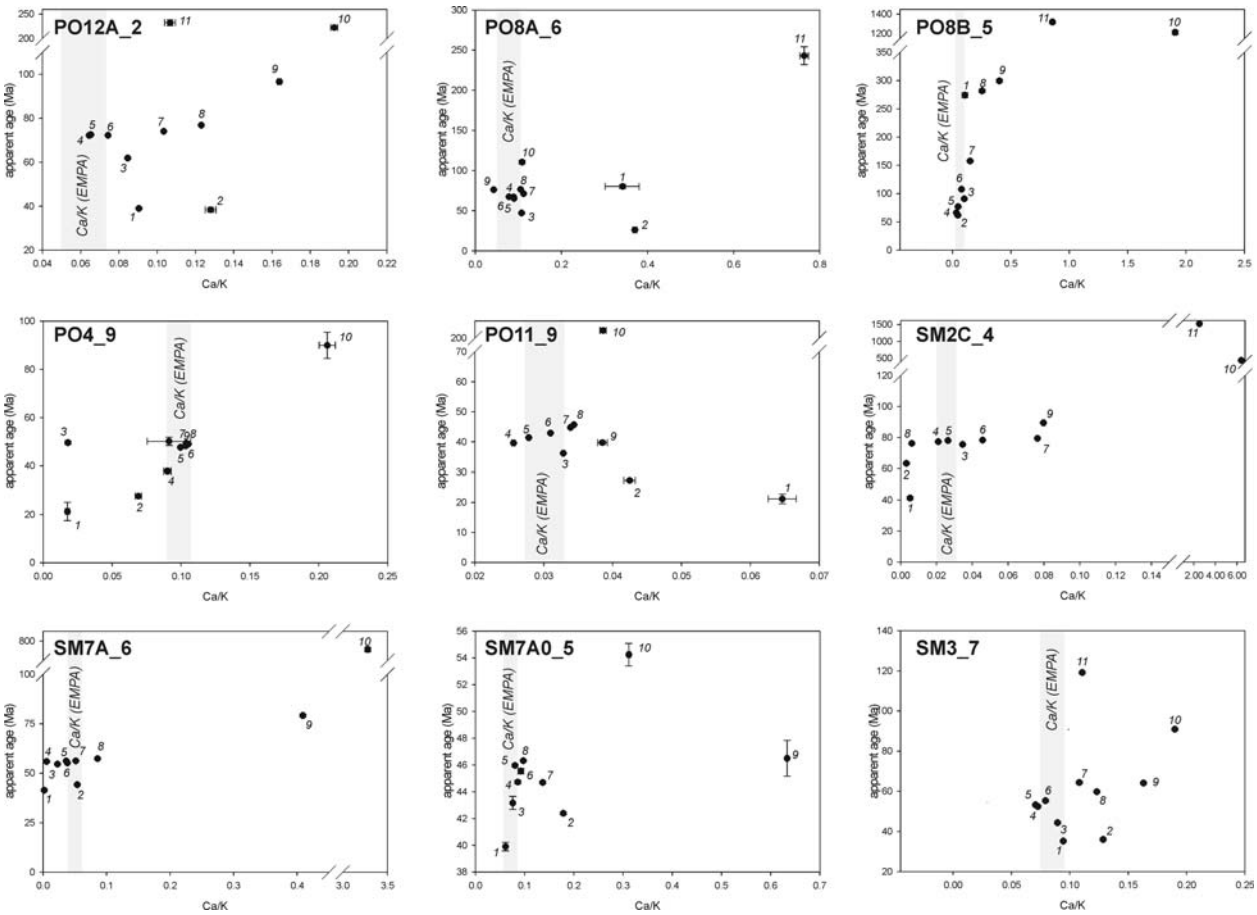

Fig. 3.1.3 Ca/K and age correlation diagrams (Zanchetta et al. 2010). The correlation between isotopic Ca/K measured during experiments, age of each temperature step and the matrix chemical composition determined by EMPA is well defined in these diagrams. The incremental steps used for the calculation of the weighted mean plateau age were selected among intermediate temperature steps matching the EMP chemical data on matrix composition.

The oldest ages are given by high temperature steps (above 800-900°C, depending on sample). Ca/K values are generally higher than matrix-related steps and EMPA values, with a few exceptions (PO8A_6 and SM2C_4, Fig. 3.1.1f and Fig. 3.1.2f). High temperature steps and associated older apparent ages can be related to the degassing of inherited clasts, mainly consisting of plagioclase and quartz.

The contamination by inherited clasts in our samples is much lower than that found in other studies (Müller et al. 2002), as testified by the amount of gas released at high temperature which is, for all samples, less than 10% and usually less than 5% of the total released ^{39}Ar.

This is a positive effect related to the new technique used in this study for the selection of micro-cores with the lowest clast/matrix ratios through MicroCT screening. Reducing the amount of inherited Ar increases the reliability and the precision of the matrix ages. These low amounts of Ar related to inherited

Table 3.1.1 Summary of pseudotachylyte ages

Sample	age (Ma)	error (2σ, 95% c.l.)
PO12A_2	73,2	2,4
PO8A_6	66,9	1,9
PO8B_5	68,5	1,9
PO4_9	48,7	1
PO11_9	43,4	2,1
SM2C_4	79,9	1,8
SM3_7	52,9	4,3
SM7A_6	56,4	1,1
SM7A0_5	45,4	1,2

components result in much more gas deriving from the breakdown of pseudotachylyte matrix, indirectly increasing the potential precision of analyses.

The efficacy of a 3D evaluation of the clast abundance with respect to 2D techniques (such as point counting or image analyses techniques, performed on polished thin sections by optical microscope or SEM) is indirectly confirmed by the very low amounts of inherited Ar in the obtained age spectra.

The obtained data show how the stepwise heating experiments relate to multiphase samples. The selection of the steps showing the matrix-related Ar release, is fundamental for a correct formation/cooling age determination of pseudotachylyte samples (Müller et al. 2002; Meier 2003). Table 3.1.1 reports a summary of the ages obtained for the 9 analysed sample.

Table 3.1.2 EMP analyses of pseudotachylyte matrix.

Sample	Element det. lim. nr	K	*sd*	Ca	*sd*	Cl	*sd*	Na	Ti	Mn	Mg	Cr	Fe	Al	Si	O	Total	Ca/K	*sd*	Cl/K
		0,02		0,01		0,01		0,02	0,02	0,03	0,01	0,01	0,04	0,02	0,02					
PO4	12	3,680	*1,012*	0,345	*0,076*	0,012	*0,008*	0,472	0,256	0,022	1,730	0,058	3,880	13,490	27,723	47,781	95,4116	0,094	*0,023*	0,003
PO8A	15	4,720	*1,156*	0,410	*0,056*	0,010	*0,005*	0,050	0,230	0,000	2,170	0,020	2,480	12,451	31,340	45,490	94,231	0,087	*0,014*	0,002
PO8B	12	5,410	*0,078*	0,270	*0,082*	0,020	*0,008*	0,110	0,210	0,000	2,090	0,010	2,330	14,263	28,512	48,715	96,24	0,050	*0,009*	0,004
PO11	7	5,070	*1,030*	0,180	*0,042*	0,030	*0,012*	0,050	0,950	0,080	6,130	0,020	9,350	11,345	24,673	46,430	99,028	0,036	*0,018*	0,006
PO12A	16	1,590	*1,218*	0,098	*0,050*	0,003	*0,009*	0,092	0,130	0,000	0,639	0,030	1,078	14,561	31,812	45,456	93,7978	0,062	*0,012*	0,002
SM2C	11	5,070	*0,973*	0,130	*0,092*	0,010	*0,005*	0,030	0,250	0,030	2,220	0,010	2,200	12,783	29,736	47,873	95,132	0,026	*0,009*	0,002
SM3	8	5,390	*1,532*	0,457	*0,043*	0,011	*0,004*	0,102	0,655	0,076	3,730	0,046	8,020	11,860	27,274	46,153	97,9152	0,085	*0,021*	0,002
SM7A	15	5,760	*1,039*	0,248	*0,027*	0,015	*0,005*	0,089	0,471	0,064	2,460	0,000	6,660	14,024	28,003	47,110	98,8803	0,043	*0,013*	0,003
SM7A0	21	5,290	*1,045*	0,373	*0,098*	0,024	*0,005*	0,115	0,605	0,057	2,990	0,050	7,170	11,042	29,302	47,348	98,679	0,070	*0,017*	0,005

Number of analyses (nr.) and standard deviation (sd) are reported. Element abundance is in atomic weight %

Table 3.1.3 $^{40}Ar/^{39}Ar$ analytical data from stepwise-heating experiment

incr. nr.	T °C	^{39}Ar %	^{40}Ar ml	$1\sigma_{40Ar}$ ml	^{39}Ar ml	$1\sigma_{39Ar}$ ml	^{37}Ar ml	$1\sigma_{37Ar}$ ml	^{36}Ar ml	$1\sigma_{36Ar}$ ml	Ca/K	$1\sigma_{Ca/K}$	Age Ma	$1\sigma_{Age}$ Ma
PO4_9														
1	551	0,497510357	3,92469E-09	2,54814E-12	1,86516E-11	2,05517E-13	1,63716E-13	1,33687E-14	1,17046E-11	2,81832E-13	0,017555304	0,001433527	21,28388294	3,788654133
2	646	8,97379489	2,17432E-08	1,90495E-10	3,36426E-10	2,90812E-12	1,16194E-11	3,97474E-13	3,65952E-11	4,01476E-13	0,069076764	0,002362974	27,62904791	0,449922481
3	727	3,732698388	8,336E-09	1,79368E-10	1,39938E-10	2,78043E-12	6,38494E-12	1,10821E-12	1,16187E-13	5,0263E-13	0,091256312	0,015838989	50,1379848	1,690590055
4	767	7,180233822	2,08796E-08	9,79106E-11	2,69186E-10	2,03915E-12	1,21281E-11	3,64194E-13	2,99399E-11	2,69222E-13	0,09011236	0,002705973	37,90711016	0,416149133
5	803	11,14269998	3,94006E-08	3,22698E-11	4,17738E-10	4,18125E-13	2,08111E-11	6,16914E-14	5,36935E-11	2,96E-13	0,099640134	0,000295369	47,64745554	0,18502158
6	843	26,09369601	7,12127E-08	1,00013E-10	9,78249E-10	1,50462E-12	5,07111E-11	2,11143E-13	4,79629E-11	2,96493E-13	0,103680938	0,000431691	49,29169083	0,125822014
7	897	19,92893455	5,53929E-08	2,33272E-11	7,47133E-10	8,25365E-13	3,93233E-11	1,18014E-13	4,08501E-11	3,10375E-13	0,105268206	0,000315924	49,02155761	0,117240449
8	990	19,68806304	5,9183E-08	4,02952E-11	7,38103E-10	8,75673E-13	3,81437E-11	1,89923E-13	5,76706E-11	3,15828E-13	0,103359653	0,000514642	48,27924001	0,123983193
9	1085	2,465811962	1,4997E-08	1,78721E-11	9,2443E-11	1,37733E-13	8,25187E-13	2,35038E-14	3,23864E-11	2,80084E-13	0,017852991	0,000508507	49,61834159	0,752226477
10	1386	0,296556994	8,17323E-09	5,13439E-12	1,11179E-11	1,20953E-13	1,14601E-12	3,28866E-14	2,36079E-11	2,4655E-13	0,206171103	0,005916393	89,99845475	5,427526028
total			3,03243E-07		3,74899E-09		1,81257E-10		3,34527E-10					
conc (ml/g)			5,25551E-06		3,24869E-08		1,57068E-09		2,89885E-09					
K(g/g)					0,009780264									
incr.				*Age (Ma)*	95% c.l.		*sample mass (g)*			*exp. nr.*		*J*		
5-8	*weighted mean plateau age*			48,7	1		0,1154			BEP14-E		0,000475		
PO8A_6														
1	536	0,57880343	1,01723E-08	5,81892E-11	2,77407E-11	1,48166E-13	4,74708E-12	7,31417E-11	2,54335E-11	2,65937E-13	0,342286419	5,273852045	80,27625914	2,412156054
2	634	6,852164544	2,75769E-08	2,17592E-10	3,28408E-10	4,15968E-12	6,08525E-11	7,87373E-13	5,92637E-11	4,79398E-13	0,370636831	0,004795688	26,08748024	0,53112069
3	718	13,67773546	7,32241E-08	5,60126E-10	6,55541E-10	4,62782E-12	3,52652E-11	3,3663E-13	1,23973E-10	6,37683E-13	0,107595002	0,001027067	47,21320137	0,541181785
4	758	17,2034302	1,09788E-07	8,33525E-11	8,24519E-10	1,48322E-12	3,71291E-11	1,3933E-13	1,54985E-10	6,46095E-13	0,090065017	0,000337977	65,31386115	0,228709215
5	801	19,94533021	1,00952E-07	5,29759E-11	9,55932E-10	1,13436E-12	3,74175E-11	1,12474E-13	8,27308E-11	3,68407E-13	0,078286854	0,000235324	67,31455205	0,127229696
6	835	15,85388153	7,31219E-08	5,06771E-11	7,59839E-10	7,21407E-13	3,38204E-11	9,5776E-14	4,25156E-11	2,98604E-13	0,089022721	0,000252103	67,04086652	0,123185256
7	889	13,20538596	6,59924E-08	2,70064E-11	6,32903E-10	6,61783E-13	3,55116E-11	1,16863E-13	4,15743E-11	2,72248E-13	0,11222251	0,000369305	71,29720166	0,130846808
8	984	6,478426709	3,90642E-08	2,33195E-11	3,10496E-10	3,59334E-13	1,63656E-11	5,49809E-14	3,6222E-11	3,04296E-13	0,105419732	0,000354162	76,62798742	0,257112958
9	1077	5,460562565	3,60283E-08	4,93949E-11	2,61712E-10	4,5759E-13	5,57298E-12	2,07695E-14	4,14784E-11	2,70105E-13	0,04258933	0,000158723	76,20617487	0,300422406
10	1197	0,639980289	1,2962E-08	5,34613E-12	3,06727E-11	1,55708E-13	1,66715E-12	2,01765E-14	3,00616E-11	2,76515E-13	0,108709715	0,00131565	110,5062367	2,215555657
11	1382	0,104299101	6,35801E-09	6,13656E-12	4,99881E-12	6,18915E-14	1,90866E-12	2,48052E-14	1,63818E-11	2,43495E-13	0,763840398	0,009926977	243,0491957	11,14611957
total			5,55239E-07		4,79276E-09		2,70258E-10		6,5462E-10					
conc (ml/g)			6,32103E-06		5,45624E-08		3,0767E-09		7,45241E-09					
K(g/g)					0,016426155									
incr.				*Age (Ma)*	95% c.l.		*sample mass (g)*			*exp. nr.*		*J*		
4-6	*weighted mean plateau age*			66,9	1,9		0,08784			BEP-14F		0,000475		
PO8B_5														
1	404	0,754679492	3,45792E-08	5,40264E-11	2,37239E-11	1,70393E-13	1,25749E-12	2,54738E-14	8,928E-11	4,37679E-13	0,106013669	0,002147593	274,1688992	4,427288278
2	538	2,021746509	2,40345E-08	6,53428E-11	6,35551E-11	6,51789E-13	1,44736E-12	1,63511E-14	6,55418E-11	3,27904E-13	0,045547152	0,000514558	61,85522852	1,417744818
3	638	1,749362342	2,69549E-08	3,90662E-12	5,49925E-11	5,10083E-14	2,75238E-12	8,39624E-15	7,09824E-11	3,3825E-13	0,100103644	0,000305369	90,858452	1,483412585

4	808	53,79805975	1,73698E-07	4,91753E-10	1,69118E-09	4,6377E-12	2,76347E-11	1,05487E-13	1,3657E-10	7,50596E-13	0,032681246	0,000124751	66,3326479	0,278620297
5	840	32,46526482	1,28502E-07	7,10263E-10	1,02057E-09	4,23895E-12	2,44008E-11	1,50821E-13	1,17928E-10	7,62645E-13	0,047818691	0,000295567	76,97490396	0,551654148
6	862	4,523603937	3,92835E-08	7,77674E-12	1,42203E-10	1,65872E-13	5,50538E-12	2,67451E-14	7,06275E-11	3,35147E-13	0,077431863	0,000376164	107,6863675	0,575670594
7	922	2,783907417	4,32097E-08	6,63797E-12	8,75143E-11	8,17549E-14	6,55017E-12	1,86564E-14	8,92729E-11	3,87217E-13	0,149701299	0,000426383	157,7090533	1,036576572
8	1001	0,874570351	2,91074E-08	1,10597E-11	2,74928E-11	4,82811E-14	3,46727E-12	2,07646E-14	6,53954E-11	3,24375E-13	0,252252842	0,00151068	281,7705378	2,598476361
9	1080	0,877641683	3,03601E-08	9,81955E-12	2,75893E-11	3,38075E-14	5,52845E-12	1,70383E-14	6,72691E-11	3,28816E-13	0,400820942	0,0012353	299,3644274	2,580612572
10	1192	0,097666565	2,60251E-08	8,26475E-12	3,07022E-12	3,06673E-14	1,31264E-12	1,39259E-14	6,44996E-11	3,27996E-13	0,855321953	0,009074173	1319,477091	16,03305909
11	1400	0,053497135	1,45774E-08	2,43563E-12	1,68172E-12	7,53904E-15	1,60205E-12	9,19286E-15	3,785E-11	2,61765E-13	1,90647009	0,010939651	1213,051159	20,51957591
total			5,70332E-07		3,14358E-09		8,14587E-11		8,75216E-10					
conc (ml/g)			6,58429E-06		3,62916E-08		9,40414E-10		1,01041E-08					
K(g/g)					0,010925675									

incr.		*Age (Ma)*	95% c.l.	*sample mass (g)*	*exp. nr.*	*J*
4-5	*weighted mean plateau age*	68,5	1,9	0,08662	BEP14-G	0,000475

PO11_9														
1	554	2,381817865	8,83202E-09	5,18776E-11	7,42626E-11	1,01289E-12	2,39965E-12	7,51812E-14	2,36469E-11	4,54999E-13	0,064627353	0,002024784	21,16060599	1,564883518
2	644	13,68972839	2,2538E-08	1,17836E-10	4,26832E-10	2,71193E-12	9,06411E-12	1,77835E-13	2,98534E-11	3,00353E-13	0,042472187	0,000833292	27,33143604	0,283929145
3	724	18,33131195	3,59662E-08	3,47594E-11	5,71551E-10	7,03817E-13	9,38733E-12	3,76822E-14	3,91577E-11	1,66113E-13	0,032848971	0,000131861	36,2116374	0,091390242
4	766	10,00090277	2,52788E-08	5,38098E-11	3,11818E-10	4,10195E-13	3,99335E-12	3,33555E-14	3,6241E-11	1,33215E-13	0,025613551	0,000213944	39,60335739	0,144251852
5	807	13,56305111	3,00414E-08	1,12598E-11	4,22882E-10	4,09402E-13	5,88412E-12	2,55285E-14	3,17415E-11	1,46981E-13	0,027828906	0,000120737	41,39222687	0,095932728
6	843	15,74166669	3,60379E-08	1,10635E-11	4,90809E-10	4,68425E-13	7,60409E-12	3,44269E-14	3,77774E-11	1,34627E-13	0,03098626	0,000140288	42,91724452	0,080048915
7	896	14,16525407	3,2901E-08	2,77003E-12	4,41658E-10	5,05171E-13	7,48233E-12	3,27976E-14	3,22677E-11	1,18997E-13	0,033883314	0,000148522	44,77748724	0,083677263
8	991	7,965513749	2,39962E-08	5,69263E-12	2,48357E-10	2,32209E-13	4,26842E-12	1,60872E-14	3,58135E-11	1,4416E-13	0,034373733	0,000129551	45,69954699	0,149771172
9	1087	3,883412056	2,79368E-08	6,7588E-12	1,21081E-10	1,68024E-13	2,33246E-12	4,33503E-14	7,53288E-11	2,9526E-13	0,038527779	0,000716065	39,73996896	0,606579025
10	1401	0,277341357	9,93031E-09	4,07911E-12	8,64722E-12	9,32569E-14	1,66981E-13	1,95386E-15	2,57101E-11	1,56711E-13	0,03862136	0,000451911	217,5414071	4,630269352
total			2,53459E-07		3,1179E-09		5,25828E-11		3,67538E-10					
conc (ml/g)			2,19065E-06		2,69481E-08		4,54476E-10		3,17665E-09					
K(g/g)					0,008112801									

incr.		*Age (Ma)*	*sample mass (g)*	*exp. nr.*	*J*
5-8	*weighted mean plateau age*	43,4	0,1157	BEP14-H	0,000475

PO12A_2														
1	532	1,752145811	9,5165E-09	2,46843E-11	6,26302E-11	2,0979E-13	2,83165E-12	1,25511E-14	2,24575E-11	9,01486E-14	0,090427215	0,000400814	38,98970227	0,392342378
2	628	7,61329678	2,6308E-08	2,85265E-10	2,72136E-10	4,92902E-12	1,741E-11	3,84011E-13	4,73497E-11	7,40846E-13	0,127956172	0,002822317	38,37735218	1,047821306
3	718	16,41474427	5,96702E-08	3,34803E-10	5,86742E-10	3,07547E-12	2,48066E-11	1,59663E-13	5,6042E-11	5,15605E-13	0,084559306	0,000544252	61,89239498	0,514269861
4	758	16,77930916	7,03303E-08	1,34263E-10	5,99774E-10	1,1566E-12	1,95769E-11	7,99547E-14	6,27161E-11	2,24054E-13	0,065282482	0,000266622	72,53270838	0,213241156
5	797	17,23970342	6,73992E-08	2,08789E-11	6,1623E-10	5,54356E-13	1,984E-11	5,56921E-14	4,88115E-11	2,15764E-13	0,064392817	0,000180755	72,207275	0,108583442
6	835	15,02525667	5,55794E-08	2,26814E-11	5,37075E-10	5,10401E-13	1,99499E-11	5,7607E-14	3,17107E-11	1,18998E-13	0,074292594	0,000214526	72,26647268	0,090952734
7	893	11,20913963	4,21757E-08	9,46107E-12	4,00669E-10	3,55413E-13	2,07089E-11	5,80201E-14	2,30901E-11	1,06787E-13	0,103375412	0,000289626	74,07513828	0,092756224
8	983	10,9768901	4,58178E-08	2,55429E-11	3,92367E-10	3,78046E-13	2,41396E-11	7,59935E-14	3,33928E-11	1,29599E-13	0,123051004	0,000387375	76,86229657	0,115925263
9	1080	2,531643638	1,88191E-08	1,17483E-11	9,04932E-11	4,37817E-13	7,41213E-12	4,18852E-14	2,82225E-11	1,20625E-13	0,163825375	0,00092576	96,61235712	0,559418396
10	1193	0,295862143	7,69963E-09	3,56948E-12	1,05755E-11	2,88495E-14	1,01801E-12	9,56674E-15	1,61693E-11	7,89549E-14	0,192534296	0,001809336	222,4621194	1,768778364
11	1382	0,162008377	4,4154E-09	1,34538E-12	5,79096E-12	1,50844E-13	3,08962E-13	8,09736E-15	9,26805E-12	3,85259E-14	0,106708526	0,002796649	232,4824163	5,872025046

total			4,07731E-07		3,57448E-09		1,58003E-10		3,7923E-10					
conc (ml/g)			5,00898E-06		4,39126E-08		1,94106E-09		4,65885E-09					
K(g/g)					0,013219997									
incr.				*Age (Ma)*	95% c.l.		*sample mass (g)*			*exp. nr.*		*J*		
4-6	*weighted mean plateau age*			73,2	2,4		0,0814			BEP14-I		0,000475		
SM2C_4														
1	539	3,547134389	1,31262E-08	1,46181E-10	2,02266E-10	3,21117E-12	5,34294E-13	5,3774E-14	1,10842E-11	3,68255E-13	0,005283081	0,000531715	41,25973893	0,910383804
2	633	10,52236182	6,17796E-08	3,48216E-10	6,00011E-10	4,1709E-12	9,5317E-13	3,03381E-14	5,6344E-11	2,06659E-13	0,003177178	0,000101125	63,33014404	0,563260955
3	719	10,1051177	6,09376E-08	2,688E-11	5,76219E-10	7,05701E-13	9,96706E-12	4,53891E-14	3,08375E-11	1,88211E-13	0,034595092	0,000157543	75,47391338	0,124696942
4	760	10,85160073	7,05036E-08	8,3171E-11	6,18785E-10	7,9986E-13	8,16641E-12	2,64187E-14	4,37331E-11	1,64267E-13	0,026395204	8,53897E-05	78,03085956	0,148339567
5	801	13,39568597	9,52636E-08	1,80511E-11	7,63855E-10	6,9227E-13	8,01447E-12	4,33195E-14	8,41083E-11	3,0853E-13	0,020984402	0,000113424	77,3102925	0,120462494
6	836	16,43570718	1,07968E-07	3,50202E-11	9,37205E-10	9,78039E-13	2,14429E-11	6,26497E-14	6,91161E-11	2,50533E-13	0,04575991	0,000133697	78,32417047	0,105909013
7	888	12,56544248	7,82246E-08	3,27037E-11	7,16513E-10	6,93096E-13	2,73621E-11	7,84251E-14	3,50689E-11	1,93662E-13	0,076377746	0,000218913	79,39312764	0,104822139
8	987	19,92800503	1,15198E-07	9,01864E-12	1,13634E-09	1,00054E-12	3,56146E-12	2,19703E-14	4,0558E-11	1,4767E-13	0,006268295	3,86685E-05	76,20306516	0,073113094
9	1047	1,863194471	2,02332E-08	1,59707E-11	1,06244E-10	2,28254E-13	4,23415E-12	4,07744E-14	2,9979E-11	1,25633E-13	0,079708302	0,000767582	89,49157491	0,348031257
10	1196	0,55093471	2,90204E-08	4,79078E-12	3,14157E-11	2,97792E-14	1,00362E-10	3,02249E-13	3,62858E-11	1,48988E-13	6,403019035	0,019283189	441,6433957	1,014224334
11	1385	0,234815501	4,56955E-08	1,75932E-10	1,33898E-11	1,36512E-13	1,67965E-11	1,77404E-13	2,81834E-11	1,6993E-13	2,51096508	0,026520705	1523,501687	11,29586019
total			6,97951E-07		5,70225E-09		2,01395E-10		4,65298E-10					
conc (ml/g)			#VALORE!		#VALORE!		#VALORE!		#VALORE!					
K(g/g)					#VALORE!									
incr.				*Age (Ma)*	95% c.l.		*sample mass (g)*			*exp. nr.*		*J*		
3-7	*weighted mean plateau age*			79,9	1,8		0.09708			BEP14-A		0,000475		
SM3_7														
1	545	3,798566009	7,81305E-09	6,83573E-11	1,05379E-10	1,8542E-12	6,66441E-13	4,57533E-14	1,22708E-11	3,19137E-13	0,012648557	0,000868364	33,73199923	0,99888462
2	640	9,828926789	2,90295E-08	2,48816E-10	2,72671E-10	4,20908E-12	8,05332E-13	1,40946E-13	6,10077E-11	4,75116E-13	0,005906994	0,00103382	34,24868178	0,739079456
3	725	9,294691991	2,6647E-08	2,00004E-11	2,57851E-10	3,28629E-13	1,74666E-11	7,09002E-14	4,58951E-11	1,624E-13	0,135484935	0,000549957	42,97669797	0,167915759
4	767	5,606095035	2,65135E-08	4,51715E-12	1,55523E-10	1,75577E-13	1,0452E-11	3,98417E-14	5,78988E-11	2,07045E-13	0,134417672	0,000512383	51,09502634	0,33270997
5	803	16,4214472	4,83909E-08	9,76586E-12	4,55559E-10	4,47036E-13	3,21496E-11	1,02053E-13	6,90373E-11	3,37707E-13	0,141150457	0,000448056	51,90498044	0,189445954
6	841	20,15636261	6,96019E-08	5,65774E-11	5,59172E-10	6,10632E-13	8,20249E-12	7,90664E-14	1,13387E-10	3,99986E-13	0,029338296	0,000282801	54,48781679	0,190330418
7	893	4,400320583	1,43033E-08	1,04589E-11	1,22072E-10	2,37421E-13	1,0234E-11	3,67131E-14	1,70763E-11	1,26788E-13	0,167680577	0,000601532	63,850713	0,285348917
8	985	21,27935655	7,13408E-08	8,44352E-11	5,90325E-10	6,69489E-13	4,97483E-11	1,66034E-13	9,99508E-11	4,02508E-13	0,168554857	0,000562549	59,69624472	0,192776395
9	1075	5,454064482	2,21489E-08	2,07633E-11	1,51305E-10	1,56806E-13	1,79831E-12	8,21587E-14	3,4899E-11	1,31299E-13	0,023770915	0,001086009	65,82221901	0,230318299
10	1190	1,97443376	1,34504E-08	4,20098E-12	5,47741E-11	4,80706E-14	2,6987E-12	1,51401E-14	2,5369E-11	1,09082E-13	0,098542604	0,000552836	90,82801293	0,48658409
11	1380	1,785734994	1,34159E-08	1,92779E-11	4,95393E-11	1,03392E-13	4,75831E-12	1,66347E-14	2,02913E-11	9,24197E-14	0,19211478	0,000671618	124,0020102	0,535459463
total			3,42655E-07		2,77417E-09		1,3898E-10		5,57083E-10					
conc (ml/g)			#VALORE!		#VALORE!		#VALORE!		#VALORE!					
K(g/g)					#VALORE!									
incr.				*Age (Ma)*	95% c.l.		*sample mass (g)*			*exp. nr.*		*J*		
4-6	*weighted mean plateau age*			52,9	4,3		0.07296			BEP14-B		0,000475		
SM7A0_5														

1	628	3,240840833	5,82115E-09	2,3252E-11	8,89764E-11	5,04812E-13	2,72645E-12	1,95218E-14	5,52259E-12	5,66446E-14	0,061285924	0,000438818	39,90486361	0,315989364
2	715	8,158648315	1,46226E-08	8,66557E-11	2,23994E-10	1,95302E-12	8,49703E-12	8,81418E-14	1,08466E-11	1,63434E-13	0,075870404	0,000787023	43,16306188	0,484466282
3	758	10,30891425	1,89323E-08	2,23082E-11	2,83029E-10	3,29757E-13	1,13667E-11	3,41222E-14	1,20309E-11	4,75795E-14	0,080323769	0,000241129	45,97110282	0,085899114
4	801	19,36319475	3,52983E-08	1,94865E-11	5,31611E-10	4,79323E-13	2,28786E-11	6,68553E-14	2,43975E-11	2,21376E-13	0,086074952	0,000251527	44,72323323	0,1129521
5	832	23,36642954	4,03168E-08	9,00224E-12	6,41519E-10	5,66674E-13	3,1208E-11	9,28441E-14	1,75884E-11	7,23026E-14	0,097297302	0,00028946	46,3172107	0,050089195
6	885	15,9286338	2,85816E-08	2,09631E-11	4,37317E-10	5,49321E-13	2,98971E-11	9,18296E-14	1,85858E-11	8,62565E-14	0,136735877	0,000419988	44,69286794	0,080593279
7	983	12,82096547	2,14248E-08	1,91949E-11	3,51996E-10	4,17385E-13	3,14115E-11	9,61948E-14	1,28955E-11	1,22713E-13	0,17848685	0,0005466	42,38822089	0,106318817
8	1078	5,578160809	1,20829E-08	2,02823E-11	1,53147E-10	1,45974E-13	7,06659E-12	3,08668E-14	1,29978E-11	1,08727E-13	0,092287909	0,000403113	45,543505	0,195598488
9	1196	0,626386775	3,84236E-09	5,42954E-12	1,71973E-11	3,71343E-14	5,44488E-12	1,92467E-14	9,80602E-12	9,28949E-14	0,633360223	0,002238812	46,49943843	1,338390594
10	1388	0,607825455	4,22541E-09	7,19233E-12	1,66877E-11	1,66852E-13	2,6006E-12	2,78613E-14	1,06712E-11	4,36356E-14	0,311710876	0,003339494	54,24494365	0,840609931
total			1,85148E-07		2,74547E-09		1,53097E-10		1,35342E-10					
conc (ml/g)			1,89178E-06		2,80523E-08		1,56429E-09		1,38288E-09					
K(g/g)					0,008445205									
incr.				*Age (Ma)*	95% c.l.		*sample mass (g)*			*exp. nr.*		*J*		
4-6	*weighted mean plateau age*			45,7	2,4		0,09787			BEP14-C		0,000475		
SM7A_6														
1	550	5,247333436	8,99363E-09	7,99033E-12	1,22897E-10	1,81704E-13	1,10981E-13	3,02471E-14	1,00959E-11	2,74024E-13	0,001806085	0,000492236	41,42954568	0,556303031
2	645	11,45430604	2,15183E-08	1,34366E-10	2,68269E-10	2,47216E-13	7,21505E-12	7,68842E-14	2,53541E-11	2,42689E-13	0,053790742	0,000573198	44,25931576	0,355125715
3	728	8,285247713	2,11243E-08	1,12296E-11	1,94047E-10	2,38248E-13	2,20765E-12	2,51217E-14	2,89962E-11	2,67141E-13	0,022753942	0,000258926	54,61482491	0,345784332
4	769	6,749611947	1,6918E-08	1,28962E-11	1,58081E-10	1,66713E-13	4,43999E-13	3,11107E-14	2,1773E-11	2,47371E-13	0,005617363	0,000393605	55,95626784	0,390785484
5	807	11,50015355	2,83276E-08	2,72473E-11	2,69342E-10	3,12241E-13	4,90078E-12	5,31441E-14	3,51276E-11	2,96788E-13	0,036391163	0,000394626	56,21814517	0,283021449
6	842	13,54804244	2,97883E-08	1,13166E-11	3,17306E-10	4,13248E-13	6,05958E-12	5,40353E-14	3,05378E-11	2,82863E-13	0,038194467	0,000340593	55,22560837	0,231024524
7	894	14,28405472	3,0101E-08	2,02434E-11	3,34543E-10	4,37243E-13	8,61249E-12	7,03008E-14	2,6357E-11	2,69307E-13	0,051488927	0,000420286	56,26954169	0,213696068
8	990	24,81405275	4,83942E-08	3,84091E-11	5,81164E-10	8,86257E-13	2,48995E-11	8,41861E-14	2,98828E-11	2,85695E-13	0,085690779	0,000289724	57,41855568	0,154836652
9	1088	3,713494243	1,54194E-08	1,06128E-11	8,69729E-11	1,63967E-13	1,77783E-11	6,95615E-14	2,43995E-11	2,5876E-13	0,408879178	0,001599833	79,14811735	0,73757568
10	1391	0,403703156	1,78579E-08	2,1363E-11	9,45504E-12	3,10727E-14	1,54841E-11	8,71578E-14	2,41315E-11	2,7308E-13	3,278908256	0,018456512	778,4435823	5,243935199
total			2,38443E-07		2,34208E-09		8,77124E-11		2,56655E-10					
conc (ml/g)			3,0468E-06		2,99269E-08		1,12078E-09		3,27952E-09					
K(g/g)					0,009009562									
incr.				*Age (Ma)*	95% c.l.		*sample mass (g)*			*exp. nr.*		*J*		
3-8	*weighted mean plateau age*			56,4	1,1		0,07826			BEP14-D		0,000475		

3.2 SHRIMP U-Th-Pb dating of magmatic bodies: results from the Gandino and the Presolana areas

Samples for SHRIMP U-Th-Pb zircon dating were collected both in the Gandino and Presolana areas. SHRIMP U-Pb zircon analyses were carried out at the new SHRIMP Remote Operating System (SROS lab, Dipartimento di Scienze Geologiche e Geotecnologie, University of Milan-Bicocca) thanks to an agreement between the Chinese Academy of Geological Sciences (CAGS, Beijing, P.R. China) and the University of Milano-Bicocca. Samples have been prepared accordingly to procedure described in Appendix 2. The $^{206}Pb/^{238}U$ ratios and ages were corrected for common Pb on the basis of the measured $^{207}Pb/^{206}Pb$ ratio according to Compston et al. (1992) and Williams (1998). Since some samples show a high proportion of common Pb, the age calculations were conducted by regressing uncorrected ratios in a Tera-Wasserburg concordia diagram (Tera and Wasserburg 1972). With a few exceptions, the data from each sample are dispersed along a mixing line between common Pb and a single radiogenic end member. The intersection of this mixing line with the Concordia curve defines the age of the samples (Ludwig 1998 and references therein). Data processing was carried out using the Squid 1.08 and Isoplot/Ex3 add-in programs (Ludwig 2001a, b). All analytical data are reported in Tab. 3. The uncertainties are given at $\pm 1\sigma$ level.

In the Gandino area samples for zircon dating were collected in the stock and surrounding dykes emplaced along normal faults. We selected the samples that showed the lowest degree of alteration. The zircon grains from samples PD1 and PD7 are transparent, red in colour and rich in inclusions (mainly apatite). The idiomorphic and prismatic habit, the oscillatory and sector zoning in CL (Fig. 3.2.1a and c) and the Th/U ratios (0.44-1.29; Tab. 3) indicate that zircons are of magmatic origin (Corfu et al. 2003; Hoskin and Schaltegger 2003 and references therein).

The $^{206}Pb/^{238}U$ ages obtained from PD1 zircons scatter from 36.2 ± 0.9 to 42.1 ± 0.8 Ma (Table 3.2.1, for this and all other samples). The selected analyses give a weighted average $^{206}Pb/^{238}U$ age of 39.48 ± 0.42 Ma, whereas on the Tera-Wasserburg (T-W) diagram (Fig. 3.2.1a) they define a line, that intercepts the Concordia at 39.83 ± 0.66 Ma. The zircons from sample PD7 present Th/U ratios (0.50 – 1.30) comparable to those from PD1 (Table 3.2.1). Selected analyses provide $^{206}Pb/^{238}U$ ages from 38.4 ± 0.8 to 40.7 ± 0.9 Ma, with a weighted average $^{206}Pb/^{238}U$ age of 39.25 ± 0.44 Ma. In the T-W diagram (Fig. 3.2.1c) the resulting intercept age is 39.14 ± 0.93 Ma, comparable within error to that determined for sample PD1. The zircons from sample PD6 are relatively small in comparison with the previous samples and predominantly short prismatic. CL images exhibit distinct inherited cores surrounded by thin (< 25 μm) magmatic overgrowth (Fig. 3.2.1b). Only two analyses were performed on these rims and yielded magmatic $^{206}Pb/^{238}U$ ages of 39 ± 1 Ma, consistent within error with those determined for samples PD1 and PD7. Obviously, the number of analyses is too small to consider the age distribution as representative of the entire sample.

One sample (VZ1) was selected from the Presolana area. Zircons from sample VZ1 are euhedral and

prismatic in shape, and their colour ranges from colourless to pale pink. They are typically 100 to 400 µm long, with an aspect ratio of 2. Prism-parallel and prism-perpendicular cracks, as well as metamictic zones are present. The CL images (Fig. 3.2.1d) reveal a fine concentric and oscillatory zoning suggesting a magmatic origin, also supported by Th/U ratio (0.37 - 0.71). U-Th-Pb analyses produced $^{206}Pb/^{238}U$ ages ranging between 41.2 ± 0.7 and 43.4 ± 0.7 Ma (Table 3.2.1), with a weighted average $^{206}Pb/^{238}U$ age of 42.13 ± 0.38 Ma. The analyses VZ1-7.1 and VZ1-13.1 on the T-W diagram (Fig. 3.2.1d) give a slightly older intercept age of 41.88 ± 0.69 Ma comparable within error to the $^{206}Pb/^{238}U$ mean age.

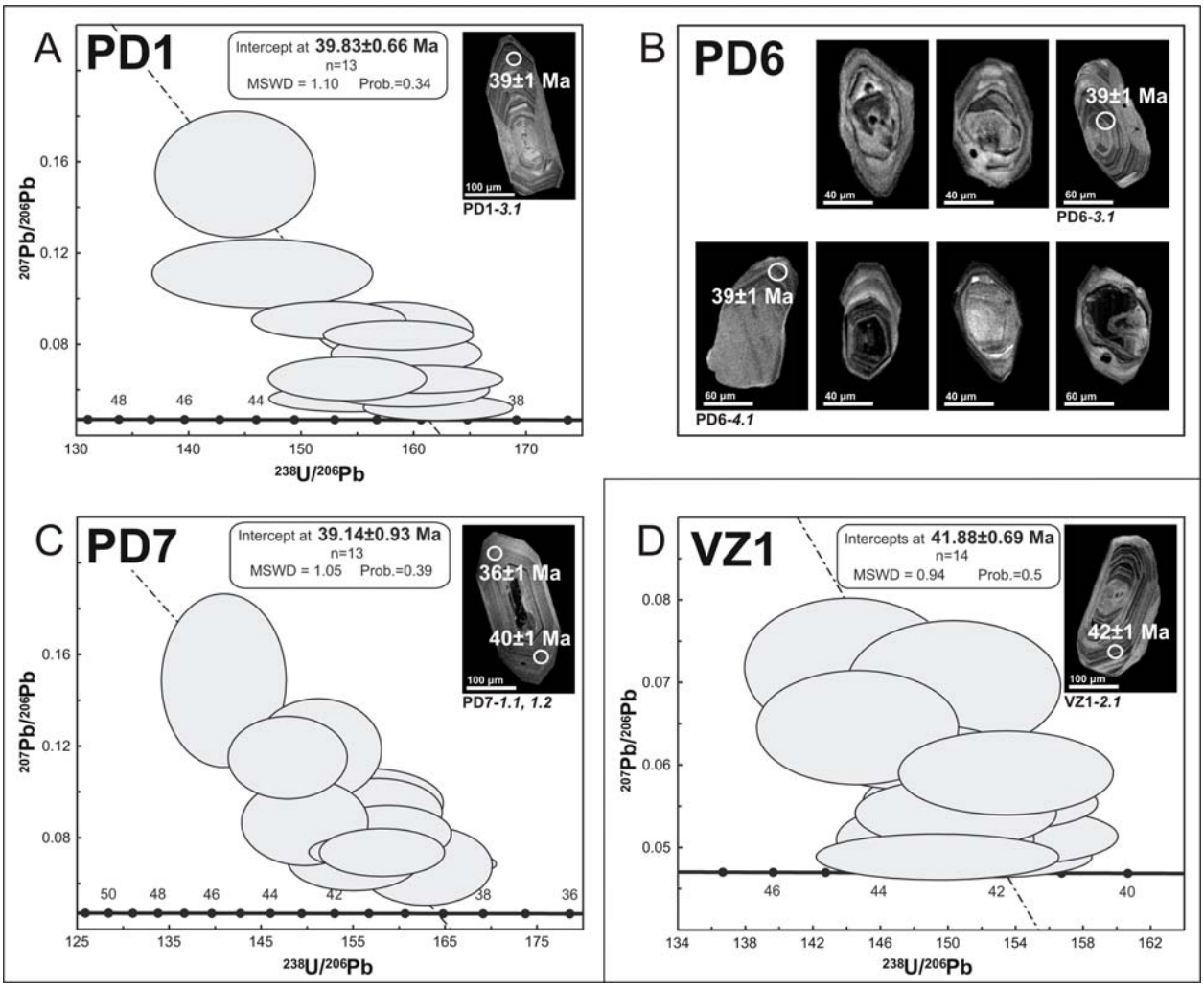

Fig. 3.2.1 Tera-Wasserburg concordia diagrams (Tera and Wasserburg 1972) representing uncorrected U-Pb zircon data from samples PD1 (A), PD7 (C) and VZ1 (D). Ages are defined by the intercept of Concordia with the regression line to common Pb. Error ellipses are 2σ. Numbers on the Concordia are in Ma (D'Adda et al. 2010). CL images of selected zircons from samples PD1 (A), PD6 (B), PD7 (C) and VZ1 (D) are also showed. Circles: SHRIMP pits; numbers: ages in Ma with 1σ error

Table 3.2.1 - SHRIMP U-Th-Pb zircon data

Spot	U	Th	Th/U	$^{206}Pb^*$	f_{206}	Total				Radiogenic		Age (Ma)	
	(ppm)	(ppm)		(ppm)	(%)	$^{238}U/^{206}Pb$	±1σ	$^{207}Pb/^{206}Pb$	±1σ	$^{206}Pb/^{238}U$	±1σ	$^{206}Pb/^{238}U$	±1σ
Sample PD1 *(Gandino dyke)*													
PD1 - 1.1	134	57	0,44	0,8	8,08	146,63	2,7	0,1108	5,6	0,0063	0,0002	40,3	1,1
PD1 - 2.1*	102	56	0,57	0,7	24,04	123,59	2,1	0,2372	5,8	0,0061	0,0002	39,5	1,2
PD1 - 3.1	298	141	0,49	1,6	4,91	158,33	1,8	0,0857	6,1	0,0060	0,0001	38,6	0,7
PD1 - 4.1	124	70	0,58	0,7	4,85	144,21	2,0	0,1543	7,3	0,0060	0,0002	38,5	1,0
PD1 - 5.1	237	100	0,44	1,3	5,51	152,48	1,8	0,0905	3,7	0,0062	0,0001	39,8	0,7
PD1 - 5.2	237	100	0,44	1,3	5,51	152,48	1,8	0,0905	3,7	0,0062	0,0001	39,8	0,7
PD1 - 6.1	347	196	0,58	1,9	3,00	157,82	1,7	0,0706	3,3	0,0061	0,0001	39,5	0,7
PD1 - 7.1	527	232	0,46	2,9	1,16	154,47	1,9	0,0561	4,3	0,0064	0,0001	41,1	0,8
PD1 - 8.1	570	679	1,23	3,0	0,65	162,18	1,7	0,0520	4,4	0,0061	0,0001	39,4	0,7
PD1 - 9.1*	192	75	0,39	4,5	6,97	162,41	2,0	0,1084	12,3	0,0065	0,0001	36,2	0,9
PD1 - 10.1*	110	58	0,53	1,6	22,53	167,71	1,8	0,0530	9,5	0,0059	0,0001	38,0	0,7
PD1 - 11.1	357	198	0,57	1,9	3,64	159,36	1,7	0,0756	4,7	0,0060	0,0001	38,9	0,7
PD1 - 12.1	202	108	0,55	1,1	1,63	159,28	1,9	0,0597	5,1	0,0062	0,0001	39,7	0,8
PD1 - 13.1	260	313	1,24	1,4	2,23	160,97	1,8	0,0645	3,9	0,0061	0,0001	39,0	0,7
PD1 - 14.1	231	149	0,66	1,3	2,25	154,13	1,9	0,0647	6,1	0,0063	0,0001	40,8	0,8
PD1 - 15.1	439	547	1,29	2,4	4,66	158,66	1,7	0,0838	3,1	0,0060	0,0001	38,6	0,7
PD1 - 16.1*	445	184	0,43	2,5	0,21	152,40	1,7	0,0486	16,4	0,0065	0,0001	42,1	0,8
PD1 - 17.1*	189	69	0,38	1,0	7,89	162,61	1,9	0,1093	7,9	0,0057	0,0001	36,4	0,8
									Weighted mean (MSWD, Prob.):			**39.48±0.42**	(1.09, 0.36)
Sample PD7 *(Gandino dyke)*													
PD7 - 1.1*	180	116	0,66	0,9	8,31	162,99	2,5	0,1125	8,6	0,0056	0,0002	36,2	1,0
PD7 - 2.1	409	418	1,06	2,2	2,83	162,13	2,1	0,0693	3,6	0,0060	0,0001	38,5	0,8
PD7 - 3.1	443	332	0,77	2,4	6,16	156,52	2,2	0,0956	6,5	0,0060	0,0001	38,5	0,9
PD7 - 4.1	299	218	0,75	1,6	2,72	162,86	1,8	0,0684	10,3	0,0060	0,0001	38,4	0,8
PD7 - 5.1	317	398	1,30	1,7	5,66	157,73	1,8	0,0916	6,6	0,0060	0,0001	38,4	0,8
PD7 - 6.1	323	155	0,50	1,8	3,78	153,80	1,8	0,0768	3,9	0,0063	0,0001	40,2	0,7
PD7 - 7.1	154	85	0,57	0,9	12,91	140,96	2,0	0,1491	10,3	0,0062	0,0002	39,7	1,2
PD7 - 8.1	310	319	1,06	1,7	4,50	158,79	1,8	0,0824	6,1	0,0060	0,0001	38,7	0,7
PD7 - 9.1	214	138	0,66	1,2	2,95	155,04	1,9	0,0703	7,4	0,0063	0,0001	40,2	0,8
PD7 - 10.1	222	181	0,84	1,3	9,12	151,23	1,9	0,1190	7,6	0,0060	0,0001	38,6	0,9
PD7 - 11.1	205	128	0,64	1,2	5,10	149,76	1,9	0,0873	8,8	0,0063	0,0001	40,7	0,9
PD7 - 12.1	268	203	0,79	1,6	8,65	147,93	1,8	0,1154	6,4	0,0062	0,0001	39,7	0,8
PD7 - 13.1*	135	71	0,53	0,3	32,22	378,37	2,7	0,8361	9,4	0,0000	0,0003	35,3	1,7
PD7 - 14.1	332	193	0,60	1,8	3,48	156,86	1,7	0,0744	3,9	0,0062	0,0001	39,5	0,7
PD7 - 15.1	399	488	1,26	2,2	3,46	158,16	1,8	0,0743	5,8	0,0061	0,0001	39,2	0,7
PD7 - 16.1*	144	79	0,55	2,6	22,32	164,32	1,7	0,0652	3,3	0,0059	0,0001	38,2	0,7
PD7 - 17.1*	424	533	1,30	2,2	2,58	167,49	1,7	0,0672	3,4	0,0058	0,0001	37,4	0,6
									Weighted mean (MSWD, Prob.):			**39.25±0.44**	(0.97, 0.48)
Sample PD6 *(Gandino Stock)*													
PD6 - 3.1	220	179	0,84	1,2	6,44	155,31	2,3	0,0978	4,5	0,0060	0,0001	38,7	0,9
PD6 - 4.1	254	116	0,47	1,4	3,27	159,71	1,9	0,0727	4,1	0,0061	0,0001	38,9	0,8
Sample VZ1 *(Presolana dyke)*													
VZ1 - 1.1*	190	78	0,41	3,9	13,69	152,20	1,7	0,0761	4,9	0,0063	0,0001	39,7	0,7
VZ1 - 2.1	939	459	0,50	5,3	1,32	152,56	1,6	0,0574	2,6	0,0065	0,0001	41,6	0,7
VZ1 - 3.1	1226	790	0,67	6,9	1,25	151,94	1,6	0,0568	2,1	0,0065	0,0001	41,8	0,7
VZ1 - 4.1	1417	850	0,62	8,0	0,27	152,60	1,6	0,0491	2,1	0,0065	0,0001	42,0	0,7
VZ1 - 5.1	1049	515	0,51	5,9	1,11	151,64	1,8	0,0557	3,2	0,0065	0,0001	41,9	0,8
VZ1 - 6.1	1020	679	0,69	5,7	0,58	153,99	1,6	0,0515	2,6	0,0065	0,0001	41,5	0,7
VZ1 - 7.1	549	223	0,42	3,3	3,15	144,18	1,8	0,0719	4,8	0,0067	0,0001	43,2	0,8
VZ1 - 8.1*	115	76	0,66	5,1	11,64	155,27	1,9	0,0599	2,6	0,0063	0,0001	39,7	0,8
VZ1 - 9.1	459	163	0,37	2,6	2,92	150,58	1,8	0,0700	4,8	0,0064	0,0001	41,4	0,8
VZ1 - 10.1	823	337	0,42	4,8	1,79	148,06	1,7	0,0611	2,7	0,0066	0,0001	42,6	0,7
VZ1 - 11.1	1057	541	0,53	6,0	1,09	152,28	1,7	0,0555	2,5	0,0065	0,0001	41,7	0,7
VZ1 - 12.1	1161	424	0,38	6,7	0,53	149,23	1,6	0,0511	3,6	0,0067	0,0001	42,8	0,7
VZ1 - 13.1	1264	839	0,69	7,5	2,24	144,66	1,7	0,0646	4,4	0,0068	0,0001	43,4	0,7
VZ1 - 14.1	1247	852	0,71	7,1	0,94	150,45	1,6	0,0543	3,1	0,0066	0,0001	42,3	0,7
VZ1 - 15.1	1833	926	0,52	10,5	0,27	149,37	2,0	0,0490	2,3	0,0067	0,0001	42,9	0,8
VZ1 - 16.1	1067	511	0,50	6,0	1,55	153,41	1,7	0,0592	3,5	0,0064	0,0001	41,2	0,7
									Weighted mean (MSWD, Prob.):			**42.13±0.38**	(0.92, 0.53)

Notes: Uncertainties given at the 1σ level; Error in FC1 reference zircon calibration was 0.44% for the analytical session (not included in above errors but required when comparing data from different mounts); $^{206}Pb^*$ indicates the radiogenic portion; f_{206}% represents the percentage of ^{206}Pb that is common Pb; (*) spots excluded from age calculations due to suspected Pb loss or high common lead fraction (Watson et al. 1997); MSWD: Mean Square of Weighted Deviates; Prob.: Probability of Fit.

3.3 Fission track dating of apatites from the Gandino area

3.3.1 General principles

Fission tracks are damage features produced in the crystal lattice of some minerals by heavy-charged particles generated by nuclear fissions. When nuclear particles travel through an insulating solid, they cause intense disturbance on the atomic scale, leaving linear trails of disrupted atoms. Fission track analysis is the study and characterization of these features in minerals.

Spontaneous tracks in minerals are mainly produced by the spontaneous fission of the isotope ^{238}U, and the preferred model to describe their formation is the "ion spike explosion model". According to this model, spontaneous fission of ^{238}U produces two highly charged heavy particles which recoil and interact with other atoms by electron stripping and ionization. Repulsion among ionized atoms causes deformation in the lattice with the creation of a "latent" fission track.

As the fission process occurs at a statistically constant rate, fission tracks analysis represent a practical method for dating minerals. It is based on the same general equation of any other isotopic dating methods and it asks the determination of both parent and daughter abundance within the sample. The main difference is that the daughter product is not represented by another isotope but by a physical damage in the crystal lattice. Relatively common minerals such as apatite and zircon are particularly suitable for fission track analysis since they usually have an appropriate concentration of the parent (i.e. ^{238}U) to produce a detectable number of fission events. The abundance of daughter products is determined by counting the number of spontaneous fission tracks on a polished surface of a single crystal, while a quite different approach is used to determine the ^{238}U amount. Fission in ^{235}U is induced in the sample by low-energy thermal neutron irradiation, producing a number of "induced tracks" that is proportional, for a given thermal neutron flux, with the amount of ^{235}U within the sample. As the $^{235}U/^{238}U$ ratio is constant in nature, the abundance of ^{238}U can be therefore estimated.

The meaning of fission track ages is strictly related to the process of *annealing*. Fission tracks are lattice damage which may remain stable over geological times only at relatively low temperature, as at elevated temperatures the displaced atoms along the tracks gradually diffuse restoring the originally ordered state, and the damage is "repaired". This process is known as *annealing* and it usually begins from the ends of the tracks, causing the reduction of their lengths until the complete cancellation. The temperature range in which fission tracks are slowly erased is known as *Partial Annealing Zone* (PAZ, Wagner & Van den Haute, 1992) and it cannot be univocally defined since the annealing process is both temperature- and time-dependent. For apatite it varies between 145° and 80°C for heating events of about 1Ma, and between 110° and 45°C for events of about 1Ga (Gleadow & Duddy, 1981). However it is commonly assumed that the PAZ of apatite corresponds to a temperature range of 120°-60°C (Gleadow & Brown, 1999). At lower temperatures tracks are stable (stability zone) whereas at higher temperatures they are rapidly erased (total annealing zone). Moreover, the cooling range of the PAZ can be simplified in a single temperature value, called *closure temperature*, defined as the temperature at which 50% of the

tracks are retained (Wagner & Reimer, 1972). For the apatite fission track termochronometer it is commonly assumed to be 100°±20°C. Deletion of fission tracks and reduction of their length due to annealing influence the age determinations, as they are based on the counting of fission tracks intersecting a given surface of a crystal. In fact the probability that a long track can intersect the analyzed surface is higher than the probability that a shortened one may intersect the same surface. For this reason an older age is expected for a sample with longer tracks (Laslett *et al*., 1987). On the other hand, if apatite (or zircon) in a rock have been affected by total fission track annealing during a thermal event (i.e. high grade metamorphism) and no other heating occurred up to present time, fission track age determinations provide the age of that event.

3.3.2 Results from the Gandino area

Apatites for fission track dating were extracted from the Gandino stock and surrounding dykes (PD2, PD3, PD4, PD5, PD6 and PD7) and processed according to the standard procedures (see caption of Table 3.3.1). Samples preparation is described in Appendix 3.

Crystals are euhedral, plenty of defects, and display very low U content (see Table 3.3.1). The central ages, in spite of their good accuracy and the high $P(\chi)^2$, have relatively large 1σ values.

Most of the samples yielded an age of 37-38 Ma, which is indistinguishable from the crystallization ages yielded by U-Pb zircon dating. Such a result indicates that the Gandino magmatic bodies were intruded into country rocks already exhumed above the partial annealing zone of apatite (crustal level 1 of Malusà et al. 2010), which is comprised between 60° and 120 °C (Gallagher et al. 1998). In the hypothesis of a "normal" geothermal gradient of 30 °C/km, their depth of emplacement is thus < 2-4 km as also suggested by their textural characters.

Table 3.3.1 - Apatite Fission-Track Data from the Gandino area

Sample	Elev. (m)	Xls	Spontaneous		Induced		$P(\chi)^2$	Dosimeter		AFT age, (Ma) ± 1σ	U, ppm
			Rho-s	Ns	Rho-i	Ni		Rho-d	Nd		
PD2	1120	5	0.714	7	3.367	33	98.62	12.37	6184	45.3 ± 18.9	3.61
PD3	770	9	0.485	19	2.755	108	99.93	12.32	6161	37.4 ± 9.3	3.02
PD4	985	11	0.864	38	4.727	208	99.25	12.28	6138	38.7 ± 6.9	4.32
PD5	655	9	0.444	16	2.444	88	100.00	12.23	6114	38.4 ± 10.5	2.45
PD6	658	14	1.144	35	6.242	191	99.93	12.18	6091	38.5 ± 7.1	6.43
PD7	1005	20	2.797	82	2.797	447	99.81	12.14	6067	38.4 ± 4.7	2.72

Notes: Samples were dated in the Milano-Bicocca Fission Track Lab using the external detector method, after irradiation in the atomic reactor "TRIGA Mk II" at the Oregon State University (U.S.A.). Neutron fluences were measured counting neutron-induced tracks in Corning glass dosimeters CN-5, placed both at the top and at the bottom of the sample holder to have the maximum control on the neutron fluence. Durango and Fish Canyon Tuff apatites were used as standards. Apatite grains were etched with 5N HNO_3 at 20°C for 20 seconds. Muscovite detectors were etched in 40% hydrofluoric acid for 45 minutes. Preparation and counting was carried out by P. D'Adda and M.G. Malusà (zeta: 346.33 ± 3.97). Abbreviations are as follows: Elev., sample elevation; Xls, number of individual grains dated; Rho-s, spontaneous track density ($\times 10^5$ tracks per cm^2); Ns, number of spontaneous tracks counted; Rho-i, induced track density in external detector ($\times 10^5$ tracks per cm^2); Ni, number of induced tracks counted; $P(\chi)^2$, probability of obtaining χ^2 value for n degrees of freedom (where n = number of crystals -1): a probability >5% is indicative of a homogeneous population; Rho-d, induced track density in external detector adjacent to dosimeter glass ($\times 10^5$ tracks per cm^2); Nd, number of tracks counted in determining Rho-d; AFT age is the sample's central fission-track age calculated using zeta calibration method.

Chapter 4

DISCUSSION:

THE ALPINE TECTONIC EVOLUTION OF THE CSA

4.1 Significance of the new geochronological constraints for the Alpine evolution of the CSA

The central sector of the Southern Alps includes a quite complete crustal section comprising a Variscan basement and an overlying Permo-Mesozoic sedimentary cover which were both involved in the Alpine deformations and consequently shortened by folding and thrusting. The absence of reliable time markers has still now hampered a precise interpretation of the timing of the Alpine deformation in this area. In this work new structural and radiometric data have been presented. They allow to provide absolute time markers for the main deformational events and an interpretation of the evolution of this sector of the Alps. As described in Chapter 2, the occurrence of pseudotachylyte veins within fault rocks developed along the Orobic and Porcile thrusts allows the isotope dating of thrusting events in the deepest structural portions of the central Southern Alps. The oldest pseudotachylyte matrix ages for both the Orobic (**79.9 ± 1.8 Ma**) and Porcile (**73.2 ± 2.4** to **68.5 ± 1.9 Ma**) thrusts indicate a Late Cretaceous (Campanian-Maastrichtian) thrust activity. Meier (2003) proposed a similar age (70.8 ± 0.5 Ma) for a pseudotachylyte injection vein in the hanging wall of the Porcile thrust. The recorded Late Cretaceous paleoseismic fault activity along the Orobic and Porcile thrusts indicates the occurrence of a growing orogenic wedge, as also supported by the deposition of the Upper Cretaceous turbiditic successions along the southern margin of the belt (Fig. 4.1.1). This thick siliciclastic turbiditic wedge accumulated in an E-W trending foredeep basin developed immediately to the south of the growing thrust stacks, as hypothized by previous authors

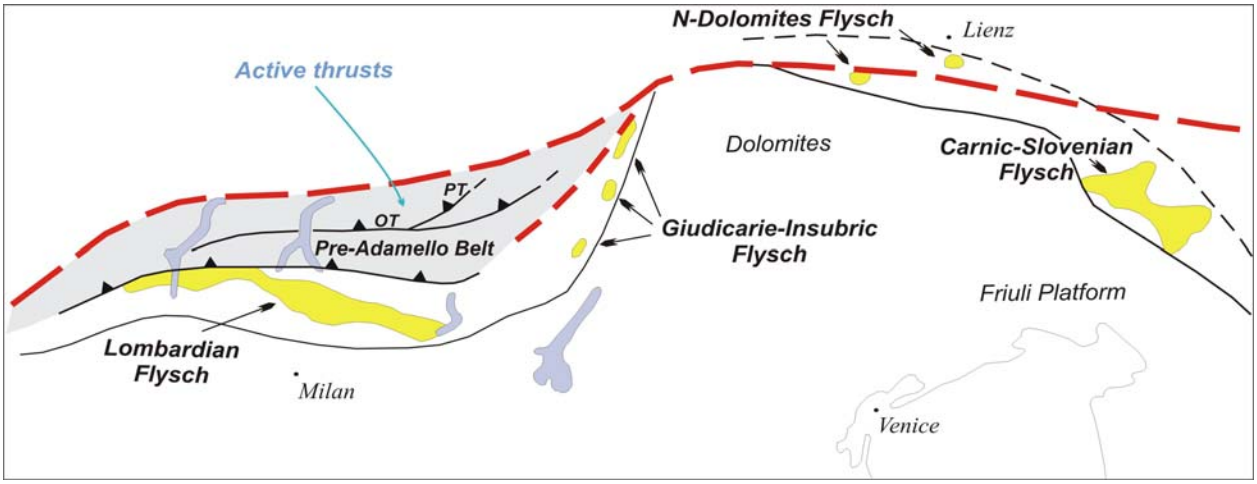

Fig. 4.1.1 Distribution of the Cretaceous flysch (modified from Castellarin et al. 2006).

(Doglioni et al. 1987; Bernoulli and Winkler 1990; Bersezio et al. 1993; Bersezio and Fornaciari 1988; Castellarin et al. 1996). The deposition of this Cenomanian to Campanian succession of terrigenous turbidites, fed from the north, testifies for the deep erosion of continental crust, including Mesozoic carbonate successions and low to medium-high grade metamorphic rocks similar to those now exposed in the Southalpine and Austroalpine basement units. During these compressive events also the Permian-Triassic sedimentary cover was strongly involved in shortening by intense thrusting an folding. The occurrence of two distinct thrusting events can be recognized in different areas through the central sector

of the Orobic belt, as described in previous chapters. As shown in Fig. 4.1.2, Late Cretaceous stacking of Middle and Upper Triassic units (A) was followed by a second thrusting event, probably related to the southward propagation of the Orobic Anticlines system (B). During this second event, the emplacement of the Orobic Anticlines belt caused uplift and backthrusting of the Upper Triassic units over Middle Triassic along the Clusone fault.

After the deposition of the Upper Cretaceous "Lombardian Flysch", the sedimentary succession recorded a marked decrease in the terrigenous input (Bersezio et al. 1993; Di Giulio et al. 2001) up to the Middle Eocene, testifying for a period of relative tectonic quiescence. This indirect evidence suggests that no major deformation and thrusting occurred in the CSA during Paleocene and the beginning of Eocene.

A second cluster of $^{40}Ar/^{39}Ar$ ages obtained on pseudotachylytes along the Orobic and Porcile thrust (56.4 ± 1.1 to 43.4 ± 2.1 Ma, Fig. 3.1.1 and 3.1.2 in chapter 3) points to a Middle Eocene re-activation of these structures also after the Late Cretaceous. Moreover, starting from the Bartonian, increasing terrigenous input testifies for a renewed tectonic activity in the Alps (Bernoulli et al. 1988; Di Giulio et al. 2001; Garzanti and Malusà 2008). According to these data, the reactivation of the Orobic and Porcile thrusts can be correlated to the ongoing Europa-Adria collision which was active during the same time interval northward (Schmid et al. 2004).

Between Middle and Late Eocene (Fig. 4.1.2 C), E-W trending normal faults affected the previously formed compressive structures and a widespread magmatic activity occurred in the Orobic Alps concurrently with the earliest phases of Adamello intrusion. The Adamello batholith was emplaced in a time interval (43-31 Ma (Mayer et al. 2003 and references therein), during which no evidence of compression was found (Brack 1984; John and Blundy 1993). Absolute age constraints for the early tectonic evolution are also given by crosscutting relationships with the Adamello intrusives along the eastern portion of the CSA.

The main Alpine compressive structures, developed in both basement and sedimentary cover, are sealed by the oldest magmatic units, providing a lower age bracket for these structures (Brack 1981, 1984; Callegari and Brack 2002; Mayer et al. 2003; Brack et al. 2008). The magmatic bodies exposed in the Gandino and Presolana areas extend these age constraints to the central sector of the Orobic Alps. The integration of field data with zircon U-Th-Pb and apatite fission-track ages provides first-order pinpoints for the evolution of the CSA (chapter 3).

In the Gandino area, a small stock and several dykes intruded the whole thrust stack. The metamorphic aureole developed around the Gandino stock clearly overprints the thrusts and normal faults that had affected the thrust imbricates. Andesitic dykes were intruded along the ENE-WSW Val Piana e Val d'Agro normal faults, which bound the Corna Lunga unit.

Magma emplacement was favoured by these extensional faults that acted as a preferential path for magma ascent. Because magmatic bodies display no signs of significant solid-state deformation, their emplacement is likely to have occurred at the end of faults activity.

Cross-cutting relationships among dykes, thrusts and normal faults were also observed in the Presolana

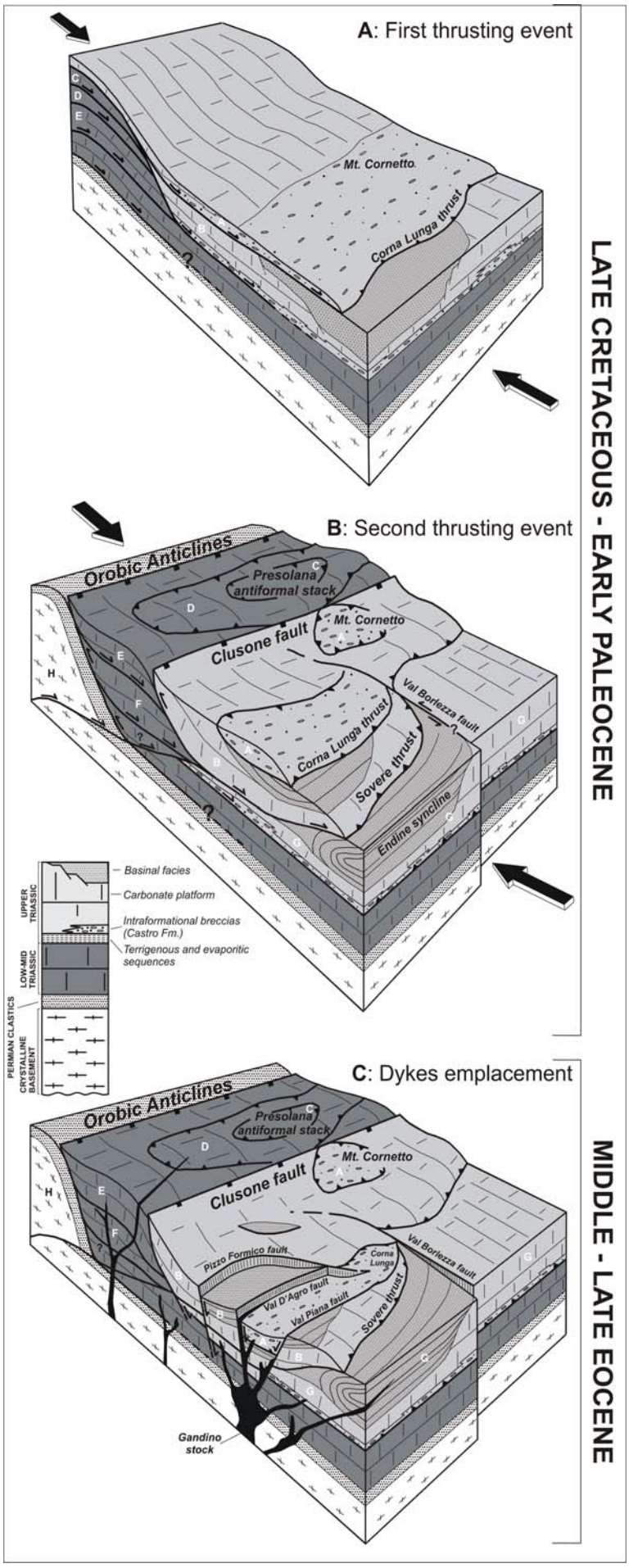

Fig. 4.1.2 Simplified reconstruction of the evolution of the northern-central sector of the CSA during pre-Adamello compressional stages of Alpine tectonics (D'Adda et al. 2010). Late Cretaceous stacking of Middle and Upper Triassic units (A) was followed by a second thrusting event, probably related to the out-of-sequence southward propagation of the Orobic Anticlines system (B). During this second event, the emplacement of the Orobic Anticlines belt caused uplift and backthrusting of the Upper Triassic units over Middle Triassic along the Clusone fault. Between Middle and Late Eocene (C), E-W trending normal faults interested the previously formed compressional structures and a widespread magmatic activity occurred concurrently with the earliest phases of Adamello intrusion. Tectonic slices: *A*, Corna Lunga unit; *B*: Pizzo Formico unit; *C*: Presolana klippe; *D*: Timogno-Presolana unit; *E*: Creste di Valzurio unit; *F*: Vigna Vaga unit; *G*: Val Camonica unit; *H*: Orobic Anticlines system.

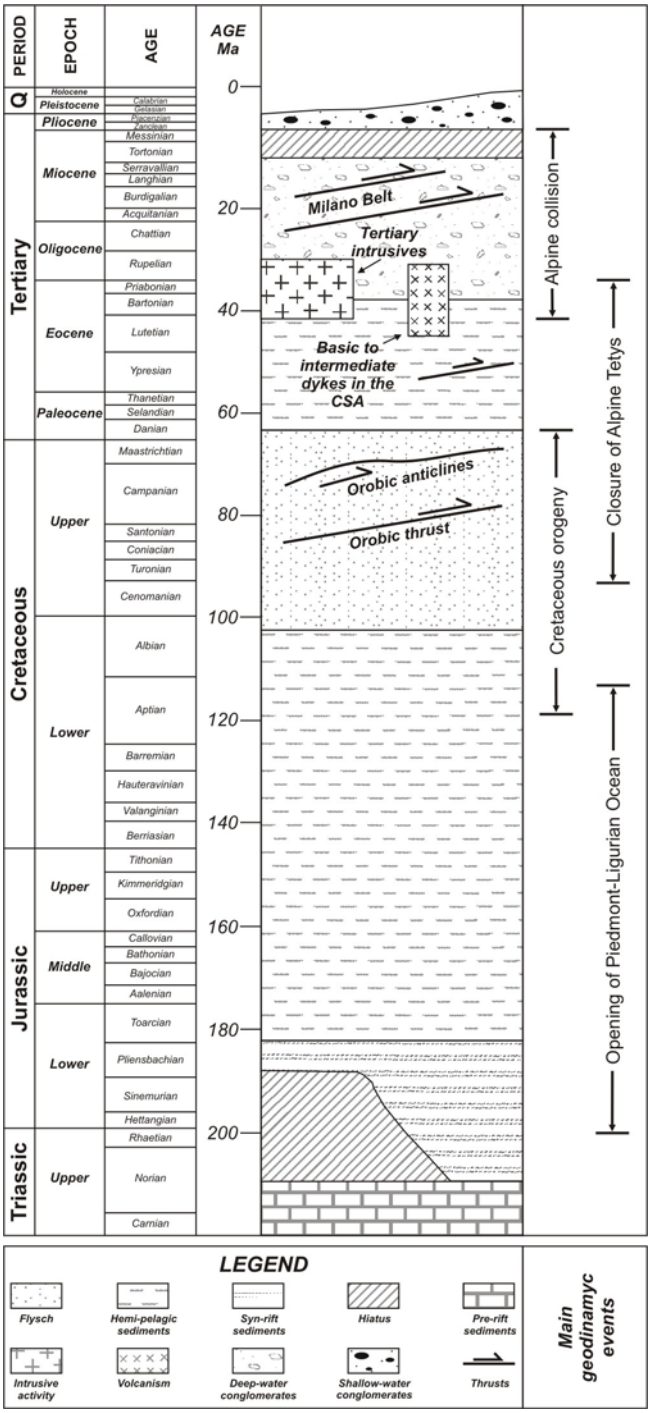

Fig. 4.1.3 Timetable of geologic events related to the Alpine orogeny in the CSA (modified from Handy et al. 2010). The Cretaceous event that led to the formation of the Eoalpine High Pressure Belt in the Austroalpine domain affected also the CSA. It was characterized by the emplacement of the Orobic and Porcile thrusts and related staks in the sedimentary cover, followed by the emplacement of the Orobic Anticlines system. In the Early Eocene a minor reactivation of the Orobic and Porcile thrusts occurred, probably related with the ongoing of the closure of the Ligurian-Piedmont and Europe-Adria collision. Between the Middle Eocene and the Early Oligocene the previously formed stack was interested by the emplacement of basic to intermediate dykes, probably related with the intrusion of the Adamello batholith. From the Late Oligocene up to the Late Miocene compressions caused the inmbrication of several thrust stacks and related folds in the frontal part of the belt (Milano Belt).

area. Here, E-W to ENE-WSE near-vertical dykes post-date the thrusting of the Creste di Valzurio unit over the Vigna Vaga unit, and are in turn cut by small extensional faults.

The Gandino stock and related dykes are quartz-andesitic to dacitic in composition, whereas the Presolana dykes are mainly basaltic (Fig. 2.3.9A). Compositional differences are coupled with slightly different U-Pb zircon ages: 42 ± 1 Ma for the Presolana basaltic andesites and 39 ± 1 Ma for the Gandino andesites and dacites (Tabs. 2.3.2, and 3.2.1 and Fig. 3.2.1). Similar ages for the Gandino dykes (34.5 ± 1.7 to 38.9 ± 1.7 Ma; K/Ar on hornblende) were previously reported by Fantoni et al. (1999), whereas significantly older ages were proposed by Zanchi et al. (1990a) (55.2 ± 1.4 Ma; K/Ar on whole rock). Literature radiometric ages for the Presolana dykes are bracketed in a wider time span, ranging between 37.1 ± 1.7, 52.6 ± 2.6 Ma (Fantoni et al. 1999) and 64 ± 1.1, 63.5 ± 1.3 Ma (Zanchi et al. 1990a). Petrographic observations on our samples, coming from the same sampling locality of Zanchi et al. (1990a) and Fantoni et al. (1999), revealed the occurrence of strong alteration that interests both hornblende phenocrysts and surrounding matrix. In these circumstances an effect of an excess Ar component, affecting both K/Ar and Ar/Ar data, can not be ruled out. Moreover the lack of accurate analytical data description in the cited works prevents any discussion. Ages and geochemical features of the Gandino and Presolana bodies are comparable to those of other Periadriatic magmatic bodies (e.g. Beccaluva et al. 1983; Conticelli et al. 2009). The U-Pb age (42 ± 1 Ma) obtained for the Presolana dykes is very close to age of the oldest units of the Adamello batholith (Corno Alto and Re di Castello units, 42 ± 0.7 Ma; Mayer et al. 2003). Younger mafic to intermediate dykes, similar to the Gandino magmatic bodies, intruded also the Adamello massif. An age of 38 ± 0.4 Ma was obtained by Mayer et al. (2003) on andesitic dykes cross-cutting the tonalites of the Val d'Avio unit. Apatite fission track ages in the Gandino magmatic bodies are indistinguishable, within error, from the zircon U-Th-Pb crystallization ages (37-38 Ma). This indicate that their depth of emplacement is less than 2-4 kilometres, as also suggested by their textural characters. Our radiometric data indicate that the Gandino and Presolana thrust stacks were already formed in the middle Eocene; however no older time brackets can be directly established for the emplacement of these thrust systems. On the basis of these data it is possible to conclude that the emplacement of the main thrust systems in the CSA, evolving from emplacement of the Orobic thrust sheet to the development of the Orobic anticlines, is probably restricted to the Cenomanian-Maastrichtian time window.

Available structural and stratigraphic evidence indicates a strong resume of tectonic activity since the Oligocene, in the later stages or shortly after the intrusion of the Adamello batholith, as also suggested by deformation along the Tonale and Giudicarie lines (John and Blundy 1993; Stipp et al. 2004; Martin et al. 1991). In fact, kinematic analyses along the Tonale line suggest an ongoing strike-slip motion during the exhumation of the northern magmatic units (Avio and Presanella intrusions, respectively dated to 34.6 ± 1.0 and 32.0 ± 2.3 Ma, by Stipp et al. 2004). After the Adamello intrusion, compression lasted at least up to the Late Miocene, propagating southward and causing the imbrication of the fold-and-thrust "Milano Belt " (Fig. 4.1.3 and Schönborn 1992; Pieri and Groppi 1981; Fantoni et al. 2004).

4.2 Implications for the Alpine orogeny

The European Alps formed in the Cretaceous-Tertiary time interval during convergence between African and European plates. Based on the present-day location of high-pressure units and ophiolitic remnants different paleogeographical reconstructions have been provided to reconstruct the Alpine region during the convergence, and several authors mainly focused their works on the comprehension of the evolution during Cretaceous times. Considering stratigraphic, structural, and geochronological data, the occurrence of Cretaceous deformations and metamorphism in the Austroalpine domain of the Eastern Alps has been documented (Von Eynatten and Gaupp 1999; Faulp and Wagreich 2000; Thöni and Jagoutz 1993; Thöni 2006). In fact, high pressure rocks in the Austroalpine basement units of the Eastern Alps (the EoAlpine High Pressure Belt, EHB, of Hoinkes et al. 1999) display a similar age of metamorphism around 90 Ma (Thöni et al. 2008 and Fig. 4.2.1).

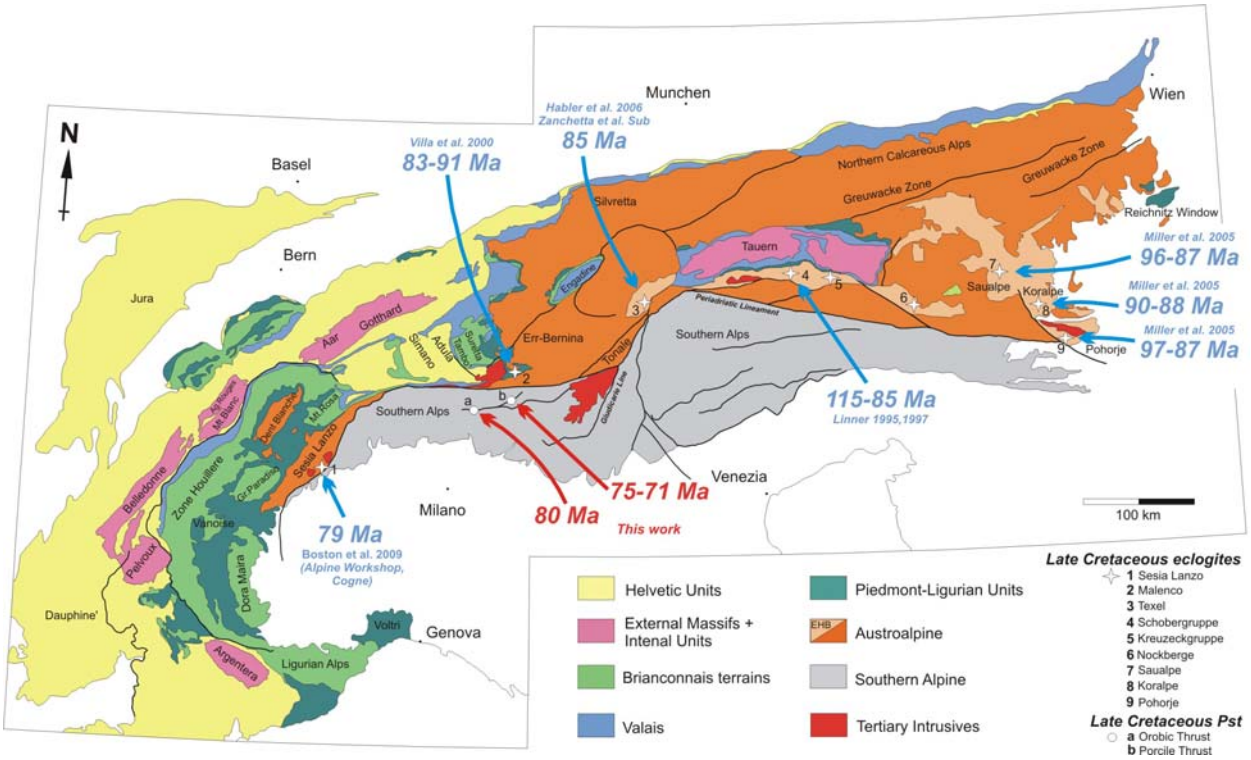

Fig. 4.2.1 Structural map of the Alps (modified from Schmid et al. 2004). The ages of the Cretaceous high-pressure metamorphism in the Austroalpine domain are reported together with Ar/Ar ages of pst veins along the Orobic and Porcile thrust in the Central Southern Alps.

Polino et al. (1990) proposed the occurrence of a single subduction zone below the northern margin of Adria which was active for long time (at least 80 Ma) and led to the growth of a pre-collisional orogenic wedge. It this model the accumulation of parts of oceanic sediments and ophiolitic units descending along the subduction zone was coupled with tectonic erosion of the active margin permitting the insertion of continental units within the subduction zone. This process was followed by the attempted subduction of the attenuated European margin and finally by continent-continent collision.

On the contrary, more recent models suggest the occurrence of two distinct subduction zones during Adria-Europe convergence (Neubauer et al. 2000; Schmid et al. 2004; Stüwe and Schuster 2010; Handy

et al. 2010). According to these authors, the Eo-Alpine Cretaceous orogeny was related to intra-continental subduction within the Adria margin and led to the closure of the westernmost branch of the Neothetys, named Meliata basin. Such event is generally considered to be separated in space and time from subduction of Piedmont-Ligurian oceanic crust which led to continent-continent collision and consequent Tertiary orogeny in the Alps (Handy et al. 2010). The Meliata ocean is generally interpreted as a Triassic intra-Austroalpine basin of the Neotethys ocean, that divided a northern Austroalpine area from a southern one also including the Southalpine domain. Although no direct evidence is available (Faulp and Wagreich 2000), these recently proposed models (Schmid et al. 2004; Schmid et al. 2008; Handy et al. 2010) suggest that the Meliata basin was located in the present-day Carpathians where ophiolitic remnants are preserved as olistoliths in Jurassic mélange formations, and possibly also in the Eastern Alps regions. The attempted subduction of the Austroalpine microcontinent below the Adria margin was related to the closure of this ocean in mid- to Late Cretaceous times and resulted in the high pressure-dominated metamorphism of the EHB (between 95 and 85 Ma, according to Thöni 2006). However, the oceanic nature of the Meliata basin has been recently questioned because of the absence of a true ophiolitic suture and continental characters of EHB rocks (Janàk et al. 2004; Stüwe and Schuster 2010; Handy et al. 2010), and the occurrence of an intra-continental subduction zone, located within the southern margin of the Alpine Thethys, has been suggested.

One of the still open problems related to these proposed models is that the extent of the Late Cretaceous orogenic event was since now considered to be confined to the Austroalpine domain of the Eastern Alps (Schmid et al. 2004). In the Southalpine domain, the occurrence of turbidites, rich in metamorphic clasts, have been widely interpreted to reflect active thrusting in the Southalpine and in the Austroalpine of the Eastern Alps (Doglioni and Bosellini 1987; Bernoulli and Winkler 1990; Castellarin et al 2006), and the depositional age of this deposits (Tuornian-Campanian, Bersezio et al. 1993) agrees with the time of the HP metamorphism of the EHB belonging to the Austroalpine (Thöni 2006). The Cretaceous Alps have been considered the result of W- to NW-directed thrusting in a single-verging orogenic wedge, mainly developed in the Austroalpine basement and cover units, while scarce attention was paid to the Southern Alps.

Data presented and discussed in this work and in Zanchetta et al. (2010) and D'Adda et al (2010) provide direct evidence that thrusting and nappe stacking were active during Late Cretaceous times not only in the Eastern Alps, but also in the CSA significantly extending southward the sector of the Alpine belt affected by the Cretaceous orogenic event. For this reason the pre-collisional Cretaceous belt should be considered as a double-verging orogenic wedge (Fig. 4.2.2) which grew on the roof of the subducting oceanic lithosphere. S- to SE-verging thrusts dominated the low- to non-metamorphic retro-wedge now preserved in the CSA, while W to NW directed thrusts developed in the pro-side of the belt. These two sectors of the double-verging orogen were probably separated by a regional fault system which realistically represented the precursor of the Periadriatic fault , presently located between the Austroalpine units which experienced an important metamorphic imprint during the Alpine orogeny from those which were only

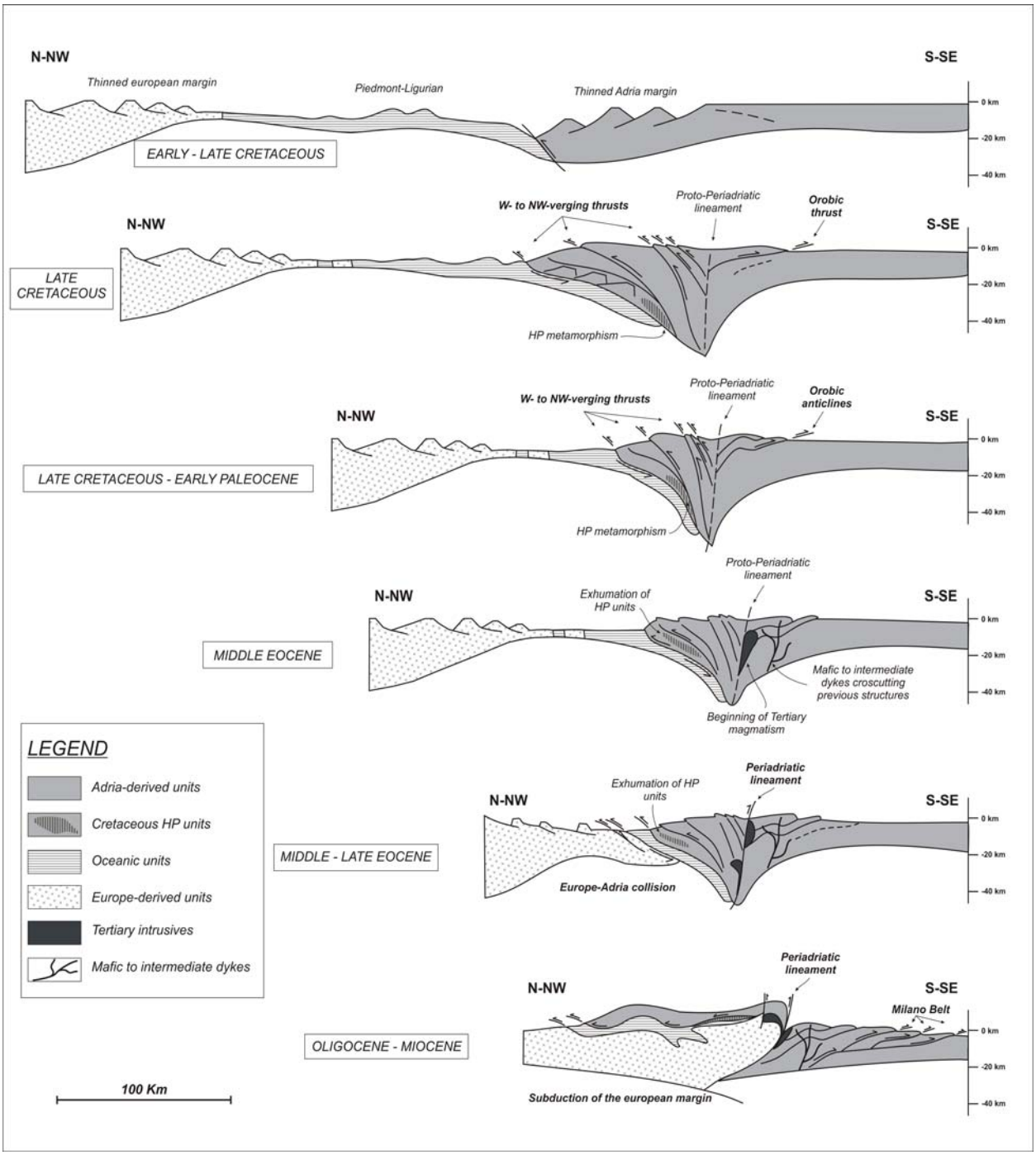

Fig. 4.2.2 Simplified recontruction of the Cretaceous-Tertiary evolution of the Alpine belt during Europe-Adria convergence.

poorly affected by metamorphic processes (Zanchetta et al. in progr).

The onset of the Tertiary continent-continent collision and subsequent subduction of the European margin below Adria strongly overprinted the previously formed structures north of the proto-Periadriatic lineament, and only few remnants of the pre-collisional Cretaceous wedge have been preserved in the Eastern Alps (HP rock complexes of the EHB).

On the contrary, in CSA the collisional event preserved the old thrust pile and major deformations occurred only in the southern part of the belt causing the growth of a complex stack of thrust units, now almost completely buried under the Quaternary Po Plain fill (Fig 4.2.2, Milano Belt).

In this model, the central-northern sector of the CSA (already structured and largely exhumed in the

Cretaceous event) were passively transported southward during this compression and no more internal shorting and deformation occurred. In this view, a fundamental role was certainly played by both the Insubric and the Giudicarie fault systems, which allow the preservation of the older structures separating the CSA from the Alpine axial belt and from the eastern sector of the Southern Alps.

Chapter 5

CONCLUSIONS

During the Alpine orogeny the CSA were interested by intense deformations and severe shortening by folding and thrusting occurred in both sedimentary cover and basement. The reconstruction of the chronology of these events has been, for long time, a matter of debate since the absence of reliable time markers in both basement and sedimentary cover hampered a precise interpretation of the timing of the Alpine deformation in this area. In this work new structural and geochronological data have been collected in different sectors of the CSA and discussed. They allowed to reconstruct the timing of the deformational events that affected this sector of the belt during he Alpine orogeny.

1- ***D3 phase***. In the crystalline basement of the CSA, S1 and S2 pre-Alpine foliation were interested by a first Alpine compressive stage (D3) which caused folding at different scales, affecting the older metamorphic fabrics without the development of an axial plane schistosity. These structures are common through all the basement and in most areas they have a trend ranging between E-W and ENE-WSW (e.g. in the Scaiss-Venina area) suggesting they were related to roughly N-S directed compressions.
Nevertheless, in other areas they show different trends. In the San Marco pass – upper Tartano Valley areas, for example, these folds generally trends to the N and strongly affect the contact between metapelites and the meta-intrusive body that crops out in the Mt. Fioraro area. This different orientation of D3 structures is probably due to the action of a local stress field, caused by the occurrence of the rigid body of the Mt. Fioraro gneiss. However, approaching the Orobic thrust fault zone, a slight E-W re-orientation of fold axes is recognizable. This suggests that D3 folding was probably related N-S compressions also in this area and slightly pre-dates the first stages of thrusting.

2- ***D4 phase.*** In the study area D3 folding is overprinted by N-dipping mylonitic foliation, which is only locally preserved. The development of mylonites within the Orobic thrust fault zone is consistent with folding and cleavage formation in the Permian and Triassic cover in the footwall. In fact, the occurrence of such E-W trending folds within the sedimentary cover can be realistically associated to the same N-S compressive regime responsible for the the formation of both the N-dipping mylonitic and later cataclastic foliations within the basement in the hangingwall.
The transition from ductile (mylonites + folding in the cover) to brittle deformation (faulting and pseudotachylytes formation) along the Orobic and Porcile thrusts resulted in a strong cataclastic overprint on existing fabrics, associated to friction-induced melting of fault rocks and the formation of pseudotachylytes (D4). $^{40}Ar/^{39}Ar$ dating of fault-related pseudotachylytes along the Orobic and Porcile thrust provides a Late Cretaceous age (ca. 80 to 68 Ma) for the beginning of brittle deformations along these structures. This implies that ductile deformation, at least in the presently exposed crustal levels, took place only in the earliest phases of the development of the orogenic wedge.
Thrusting along the Orobic and Porcile thrusts was followed by a second stage of shortening along deeper, not exposed, thrust surfaces, which caused the emplacement of the Orobic Anticlines system. The occurrence of a major Late Cretaceous compressive deformations in the CSA may be directly correlated

to the deposition of the coeval Lombardian Flysch in an E-W trending foredeep basin developed along the margin of the south-verging belt.

Also the Triassic sedimentary cover was strongly interested by thrusting and folding during the earliest stages of Alpine tectonics. In the CSA different imbricates (Grigne group, Mt. Menna and Mt. Arera group, Presolana massif and Gandino area) are the results of two main phases of thrust stacking within the Triassic sedimentary cover, coeval with the emplacement of the Orobic thrust sheet and with the subsequent growth of the Orobic Anticlines. During their growth these stacks were separated from each other by N-S directed strike slip transverse zones (Schönborn 1992). The Grem – Vedra Transverse Zone (GVTZ) is one of these N-S fault zones that interrupt the lateral continuity of an antiformal thrust stack developed within the Lower to Middle Triassic carbonate units. Our field data and analyses indicate that this important fault zone acted in a transpressional regime since the emplacement of the oldest thrust sheets. A pre-Adamello age for these compressive events is supported by a similar structural evolution recorded in the adjacent units of the belt (i.e. the Presolana antiformal stack; Zanchi et al. 1990a; chapter 2 of this work or D'Adda et al. 2010). The progressive southward propagation of the N-Grem fault suggests close kinematic relationships with the thrust stack of the Middle Triassic units, which was emplaced following a break-forward thrust sequence. This indicates that the GVTZ nucleated and developed during the growth of the thrust pile. The transverse zone was then reactivated as an oblique tear fault along the present day S-Grem fault during a subsequent thrust event related with out-of-sequence thrust emplacement (Orobic anticlines) associated to important back-thrusting phenomena in the northern sector of the belt.

3- A Middle Eocene reactivation of the Orobic and Porcile thrusts is suggested by a second $^{40}Ar/^{39}Ar$ age cluster of pseudotachylyte veins generation occurring along these two structures (ca. 55 to 43 Ma). This event can be interpreted as a minor effect of the ongoing Alpine collision, as no important syn-tectonic sedimentation is recorded in the South Alpine foredeep. The already exhumed structures of the northern sector of he CSA were probably reactivated with "horizontal" displacements and minor vertical movements, with no further exhumation, acting as a "thin-skinned"-type thrust pile.

4- Towards the end of the Middle Eocene the previously stacked units of both the crystalline basement and the sedimentary cover were interested by a widespread magmatic activity and were crosscut by hypabissal calc-alkaline bodies, basaltic to dacitic in composition, which postdate both stages of thrust stacking of D4 phase (Orobic thrust and Orobic anticlines). The emplacement of the Gandino stock and related dykes was controlled by ENE-WSW extensional fault systems, pointing to a local extensional regime during magma intrusion. U-Th-Pb zircon data from these magmatic bodies indicate an emplacement age of ca. 42 Ma for the Presolana dykes, and ca. 39 Ma for the Gandino bodies, which are very close to emplacement ages of the oldest units of the Adamello batholith. Fission-track ages point to emplacement at very shallow crustal levels, in country rocks already exhumed above the partial annealing

zone of apatite. This indicates that the northern-central sector of the CSA was already structured and largely exhumed in middle Eocene times and an inferred Late Cretaceous age for the main phases of thrusting is in agreement with obtained radiometric data on pseudotachyyte veins along the Orobic and Porcile thrusts. After magma emplacement no significant crustal thickening and shortening occurred in these already structured and exhumed parts of the CSA. During the subsequent compressional events (D5 phase) the northern and central sectors were probably passively transported to the south along deeper thrust surfaces.

5- ***D5 phase***. After continent-continent collision, the subsequent subduction of the European margin lasted up-to the Miocene and caused intense deformations of the southern part of the belt (Milano Belt). The northern and central sectors of the CSA were not interested by thickening but minor reverse, low-angle, N-dipping fault planes formed in both the basement and the sedimentary cover (SP1 and SP2, see previous chapters).

Data presented in this work provide the first direct evidence of a Late Cretaceous tectonic activity in the CSA, previously envisaged only on the base of the presence of the Cenomanian to Maastrichtian Lombardian flysch (Doglioni and Bosellini 1987; Bernoulli and Winkler 1990; Castellarin et al. 2006) deposited in the E-W trending foredeep at the southern edge of the growing orogenic wedge. Coeval metamorphism and deformation of the Austroalpine units in the Central and Eastern Alps point to a common evolution of the two domains during Late Cretaceous. In fact, in the Austroalpine basement units of the Eastern Alps, high pressure rocks displaying similar age of metamorphism around 90 Ma occur.
Previous authors suggested that this Late Cretaceous orogenic event was considered to be confined to the Austroalpine domain of the Eastern Alps (Schmid et al. 2004; Handy et al. 2010).
Our data indicate that thrusting and nappe stacking were active during Late Cretaceous times also in the CSA, significantly extending southward and eastward the sector of the Alpine belt affected by the Cretaceous orogenic event.
In this scenario, the CSA can represent the low- to non-metamorphic retro-belt of a doubly-verging Cretaceous Alpine chain, in which the high pressure units of the so-called Eo-Alpine High Pressure Belt recorded the coeval activation of a S to SE directed subduction zone.

REFERENCES

Albini S, Battaglia D, Bellini G, Bigoni E, Carminati E, Ceriani S, Forcella F, Gosso G, Guizzetti D, Oliva A, Rebay G, Siletto GB, Spalla MI (1994) Alpine deformations and pre-Alpine remnants in the north-eastern Orobic Alps, Southalpine Belt. In: Montrasio A, and Sciesa E (eds.) Proceedings of Symposium CROP-Alpi Centrali, Quaderni Geod Alpina e Quaternaria 2: 25-39

Angelier J (1984) Tectonic analysis of fault slip data sets. J Geoph Res 89: 5835-5848

Angelier J (1990) Inversion of field data in fault tectonics to obtain the regional stress-III. A new rapid direct inversion method by analytical means. Geophys J Int 103(1): 363-376

Beccaluva L, Bigioggero B, Chiesa S, Colombo A, Gatto GO, Gregnanin A, Montrasio A, Piccirillo EM, Tunesi A (1985) Post collisional orogenic dyke magmatism in the Alps. Mem Soc Geol It 26: 341-359

Bellemans F, De Corte F, Van den Haute P (1995) Composition of SRM and CN U-doped glasses: significance for their use as thermal neutron fluence monitors in fission track dating. Radiation Measurements 24: 153-160

Bergomi MA (2004) Integrated study of the "Gneiss Chiari" in the framework of the Orobic basement of Southern Alps (field relationships, mineral chemistry, geochemistry and geochronology). Eur J Mineral Plinius Italian Supplement 30: 54-59

Bergomi MA, Colombo A, Tunesi A, Caironi V, Boriani A (2004) Ordovician granitoids in the Southern Alps basement (Monte Fioraro Complex – Central Alps): geochemistry and SHRIMP U-Pb zircon age. 32nd International Geological Congress (Firenze – Italy) Abstract Vol. 2: 1062

Berlenbach JW, Roering C (1992) Sheat-fold-like structures in pseudotachylyte. J Struct Geol 14: 847-856

Bernoulli D, Winkler W (1990) Heavy mineral assemblages from Upper Cretaceous South- and Austroalpine flysch sequences (Northern Italy and Southern Switzerland): source terranes and paleo-tectonic implications. Eclogae Geol Helv 83: 287-310

Bernoulli D, Herb R, Grunig A (1988) The Ternate Formation, a Late Eocene bioclastic submarine fan of the Lombardian Basin (Southern Alps). Abstract, Amer Assoc Petrol Geol, Mediterranean Basin Conf Nice Sept 25-28

Berra F, Jadoul F (1996) Norian serpulid and microbial bioconstructions: implications for the platform evolution in the Lombardy Basin. Facies 35: 143-162

Berra F, Rovellini M, Jadoul F (1991) Assetto strutturale delle Prealpi Bergamasche a sud della Faglia di Clusone. Atti Tic Sc Terra 34: 107-120

Berra, F, Carminati E (2009) Subsidence history from a backstripping analysis of the Permo-Mesozoic succession of the Central Southern Alps (Northern Italy). Basin Researches. doi:10.1111/j1365-2117.2009.00453.x

Bersezio R, Fornaciari M (1988) Tectonic framework of the Lombardy foothills (Southern Alps) between Brianza and Lake Iseo. Rend Soc Geol Ital 11: 75-78

Bersezio R, Fornaciari M, Gelati R, Napolitano A, Valdisturlo A (1993) The significance of the Upper Cretaceous to Miocene clastic wedges in the deformation history of the Lombardian southern Alps. Geol Alp 69: 3-20

Bersezio R, Jadoul F, Chinaglia N (1997) Geological map of the Norian-Jurassic succession of the Southern Alps north of Bergamo. Boll Soc Geol Ita 116: 363-378

Bersezio R, Fantoni R, Pessina C (2001) L'assetto strutturale del margine sudalpino-padano: contributo alla conoscenza del sottosuolo nel settore bergamasco. Geol Insubr 6: 81-93

Black LP, Kamo SL, Allen CM, Aleinikoff JN, Davis DW, Korsch RJ, Foudoulis C (2003) Temora 1: A new zircon standard for Phanerozoic U-Pb geochronology. Chem Geol 200: 155-170

Blom JC, Passchier CW (1997) Structure along the Orobic thrust, Central Orobic Alps, Italy. Geol Rundsch 86: 627-636

Brack P (1981) Structures in the southwestern border of the Adamello Intrusion (Alpi Bresciane, Italy). Schweiz Mineral Petrogr Mitt 61: 37-50

Brack P (1984) Geologie der Intrusiva und Rahmengesteine des Sudwest-Adamello (Nord-Italien). Mitt Geol Inst ETH Univ Zurich 7612: 253 pp

Brack P, Dal Piaz GV, Baroni C, Carton A, Nardin M, Pellegrini GB, Pennacchioni G (2008) Carta Geologica d'Italia alla scala 1:50000. Foglio 058, Monte Adamello

Cadel G, Cosi M, Pennacchioni G, Spalla MI (1996) A new map of the Permo-Carboniferous cover and Variscan metamorphic basement in the Central Orobic Alps, Southern Alps – Italy. Mem Sci Geol (Padova) 48: 1-53

Callegari E, Brack P (2002) Geological map of the tertiary Adamello batolith (northern Italy). Explanatory notes and legend. Mem Sci Geol (Padova) 54: 19-49

Carminati E (2009) Neglected basement ductile deformation in balanced-section restoration: An example from the Central Southern Alps (Northern Italy). Tectonophysics 463: 161-166

Carminati E, Siletto GB (1997) The effects of brittle-plastic transitions in basement-involved foreland belts: the Central Southern Alps case (N Italy). Tectonophysics 280: 107-123

Carminati E, Siletto GB (2005) The Central Southern Alps (N. Italy) paleosismic zone: a comparison between field observations and predictions of fault mechanics. Tectonophysics 401:179-197

Carminati E, Siletto GB, Battaglia D (1997) Thrust kinematics and internal deformation in basement involved foreland fold and thrust belt: the Eastern Orobic Alps case (Central Southern Alps, Northern Italy). Tectonics 16: 259-271

Carrapa B, Di Giulio A (2001) The sedimentary record of the exhumation of a granitic intrusion into a collisional setting: the Lower Gonfolite Group, Southern Alps, Italy. Sedimentary Geology 139: 217-228

Casati P, Gnaccolini M (1967) Geologia delle Alpi Orobie Occidentali. Riv. It. Paleo. Strat. 73: 25-162

Cassinis G, Dal Piaz GV, Eusebio A, Gosso G, Martinotti G, Massari F, Milano PF, Pennacchioni G, Perello M., Pessina CM, Roman E, Spalla MI, Tosetto S, Zerbato M (1986) Report on a structural and sedimentological analysis in the Uranium province of the Orobic Alps, Italy. Uranium 2: 241-260

Castellarin (1979) Il problema dei raccorciamenti crostali nel Sudalpino. Rend Soc Geol It 1:21-23

Castellarin A (2009) Basic stratigraphy and tectonics of the Southern Alps around the Giudicarie Lineament (Southern Alps, Italy). Ital J Geosci 128(2): 409-417

Castellarin A, Vai GB, Cantelli L (2006) The Alpine evolution of the Southern Alps around the Giudicarie faults: a Late Cretaceous to Early Eocene transfer zone. Tectonophysics 414: 203-223

Chilès JP, Aug C, Guillen A, Lees T (2004) Modelling the geometry of geological units and its uncertainty in 3D from structural data: the potential-field method. In: Proceedings Orebody Modelling and Strategic Mine Planning, Perth, WA, 22-24 November 2004: pp 313-320

Colombo A, Tunesi A (1999) Alpine metamorphism of the Southern Alps west of the Giudicarie Line. Schweiz. Mineral. Petrogr. Mitt. 79: 183-189

Compston W, Williams IS, Kirschvink JL, Zhang Z, Ma G (1992) Zircon U-Pb ages for the Early Cambrian time-scale. J Geol Soc London 149: 171-184

Conticelli S, Guarnieri L, Farinelli A, Mattei M, Avanzinelli R, Bianchini G, Boari E, Tommasini S, Tiepolo M, Prelević D, Venturelli G (2009) Trace elements and Sr-Nd-Pb isotopes of K-rich, shoshonitic, and calc-alcaline magmatism of the Western Mediterranean Region: Genesis of ultrapotassic to calc-alkaline magmatic associations in a post-collisional geodynamic setting. Lithos 107: 68-92

Corfu F, Hanchar JM, Hoskin PWO, Kinny PD (2003) Atlas of zircon textures. In: Hanchar JM, Hoskin PWO (eds) Zircon, Reviews in Mineralogy and Geochemistry, Mineral Soc America Geochem Soc, Washington D.C. 53: 469-500

Crespi R, Liborio G, Mottana A (1982) On a widespread occurrence of stilpnomelane to the South of the Insubric line, Central Alps, Italy. Neues Jahr Mineral 6: 265–271

De Kemp EA (1999) Visualization of complex geological structures using 3-D Bezier construction tools. Comp Geosc 25 (5): 581-597

De Jong KA (1979) Overthrusts in the central Bergamasc Alps, Italy. Geol en Mijnb 58(2): 277-288

De Kemp EA (2000) 3D visualization of structural field data: examples from the Archean Caopatina Formation, Abitibi greenstones belt, Quebec, Canada. Comp Geosc 26 (5): 509-530

De Kemp EA, Schetselaar EM, Sprague K (2006) 3-D symbolization of L-S fabrics as an aid to the analysis of geological structures. Comp Geosc 32 (1): 52-63

De Michele V, Zezza U (1973) Lo stock leucogabbrico in Valle Rossa (Cene, Bergamo) e la sua aureola metamorfica. Atti Soc Ital Sci Nat Museo Civ Stor Nat Milano 114: 345-382

De Michele V, Zezza U (1978) Manifestazioni ipoabissali quarzodioritiche di età alpine nelle Prealpi Bergamasche (Alpi Meridionali). Atti Soc Ital Sci Nat Museo Civ Stor Nat Milano 119: 181-210

Del Moro A, Pardini G, Quercioli Q, Villa IM, Callegari E (1985) Rb/Sr and K/Ar chronology of Adamello granitoids, Southern Alps. In: Dal Piaz GV (ed) Il magmatismo tardo alpino nelle Alpi. Mem Soc Geol It 26: 285-299

Denison C, Carlson WD, Ketcham RA (1997) Three-dimensional quantitative textural analysis of metamorphic rocks using high-resolution computed X-ray tomography: Part I. Methods and techniques. J Metam Geol 15: 29-44

De Sitter LU (1963) La structure des Alpes Lombardes. In: Livre à la mémoire du Prof. P. Fallot, Tome II. Soc Geol France, pp 247-256, Paris.

De Sitter LU, De Sitter-Koomans CM (1949) The geology of the Bergamasc Alps, Lombardia, Italy. Leidse Geol. Meded 14B: 1-257

D'Adda P, Zanchi A, Bergomi M, Berra F, Malusà MG, Tunesi A, Zanchetta S (2010) Polyphase thrusting and dyke emplacement in the central Southern Alps. Int J Earth Sci: doi:10.1007/s00531-010-0586-2

D'Adda P, Zanchi A, Zanchetta S, Berra F (submitted) Syn thrust deformation across a transverse zone: the Grem-Vedra fault system (Central Southern Alps, N Italy)

Diella V, Spalla MI, Tunesi A (1992) Contrasted thermo-mechanical evolutions in the Southalpine metamorphic basement of the Orobic Alps (Central Alps, Italy). J Met Geol 10: 203-219

Di Giulio A, Carrapa B, Fantoni R, Gorla L, Valdisturlo A (2001) Middle Eocene to Early Miocene sedimentary evolution of the western Lombardian segment of the South Alpine foredeep (Italy). Int J Earth Sci 90: 534-548

Doglioni C, Bosellini A (1987) Eoalpine and mesoalpine tectonics in the Southern Alps. Geol Rundsch 76: 735-754

Dunkl I (2000) Trackkey: a Windows program for calculation and graphical presentation of fission track data. Comput Geosci 28: 3-12

Fantoni R, Bersezio R, Forcella F, Gorla L, Mosconi A, Picotti V (1999) New dating of the Tertiary Magmatic products of the central Southern Alps, bearings on the interpretation of the Alpine tectonic history. Mem Sci Geol (Padova) 51: 47-61

Fantoni R, Bersezio R, Forcella F (2004) Alpine structure and deformation chronology at the Southern Apls – Po Plain border in Lombardy. Boll Soc Geol It 123: 463-476

Faupl P, Wagreich M (2000) Late Jurassic to Eocene paleogeography and geodynamic evolution of the Eastern Alps in: F. Neubauer, V. Höck (Eds), Aspects of geology in Austria. Mitt Österr Geol Gesellschaft 92: 79-94

Forcella F (1988) Assetto strutturale delle Orobie orientali, tra la Val Seriana e la Val Camonica. Rend Soc Geol It 11: 269-278

Forcella F, Jadoul F (2000) Carta Geologica della Provincia di Bergamo alla scala 1:50.000 (Geological Map of the Bergamo Province, scale 1:50.000). Grafica Monti, Bergamo

Froitzheim N, Derks JF, Walter JM, Sciunnach D (2008) Evolution of an Early Permian extensional detachment fault from synintrusive, mylonitic flow to brittle faulting (Grassi detachment fault, Orobic Anticline, Southern Alps, Italy). Geol Soc London, Spec Publ 298, 69-82

Gaetani M (1975) Jurassic stratigraphy of the Southern Alps: a review. C. Squyres (ed.), Geology of Italy, Earth Sc Soc, Lybian Arab. Republ., pp. 377-402, Tripoli.

Gaetani M, Jadoul F (1979) The structure of the Bergamasc Alps. Accad Naz Lincei Rend Cl Sc Fis Mat Nat Ser VIII 46: 411-416

Gaetani M, Jadoul F (1987) Controllo ancestrale sui principali lineamenti strutturali delle Prealpi lombarde centrali. Ren Soc Geol Ita 10: 21-24

Gallagher K, Brown R, Johnson C (1998) Fission track analysis and its applications to geological problems. Annu rev Earth Planet Sci 26: 519-572

Garzanti E, Malusà MG (2008) The Oligocene Alps: Domal unroofing and drainage development during early orogenic growth. Earth Planet Sci Lett 268: 487-500

Gelati R, Napolitano A, Valdisturlo A (1991) Results of studies on the Meso-Cenozoic succession in the Monte Olimpino 2 tunnel. The tectono-sedimentary significance of the 'Gonfolite Lombarda'. Riv Ita Paleontol Stratigr 97(3-4): 565-598

Handy MR, Schmid SM, Bousquet R, Kissling E, Bernoulli D (2010) Reconciling plate –tectonic

reconstructions of Alpine Thethys with the geological-geophysical record of spreading and subduction in the Alps. Earth Sci Rev 102: 121-158

Hoinkes G, Koller F, Rantitsch G, Dachs E, Hock V, Neubauer F, Schuster R (1999) Alpine metamorphism of the Eastern Alps Schweiz Mineral Petrogr Mitt 79: 155-181

Hoskin PWO, Schaltegger U (2003) The composition of zircon and igneous and metamorphic petrogenesis. In: Hanchar JM, Hoskin PWO (eds) Zircon, Rev Mineral Geochem, Mineral Soc Am Geochem Soc, Washington D.C. 53: 27-62

Hurford AJ (1990a) International Union of Geological Sciences Subcommission on Geochronology recommendation for the standardization of fission track dating calibration and data reporting. Nuclear Track 17: 233-236

Hurford AJ (1990b) Standardization of fission-track dating calibration: recommendation by the Fission Track Working Group of the I.U.G.S. Subcommission on Geochronology. Chem Geol 80: 171-178

Hurford AJ, Green PF (1983) The zeta age calibration of fission-track dating. Chem Geol Isotope Geosc 1: 285-317

Husson L, Mugnier JL (2003) Three-dimensional horizons reconstruction from outcrop structural data, restoration and strain field of the Baisahi anticline, Western Nepal. J Str Geol 25(1): 79-90

Jadoul F, Berra F, Frisia S, Ricchiuto T, Ronchi P (1991) Stratigraphy, paleogeography and genetic model of late Carnian carbonate breccias (Castro Formation, Lombardy, Italy). Riv It Paleont Stratigr 97: 355-392

Jadoul F, Berra F, Frisia S (1992) Stratigraphic and paleogeographic evolution of a carbonate platform in an extensional tectonic regime: the example of the Dolomia Principale in Lombardy (Italy). Riv It Paleont Stratigr 98: 29-44

Janàk M, Froitzheim N, Luptàk B, Vrabec M, Krogh Ravna EJ (2004) First evidence for ultra-high-pressure metamorphism of eclogites in Pohorje, Slovenia: Tracing deep continental subduction in the Eastern Alps. Tectonics 23: TC5014, doi:10.1029/2004TC001641

John BE, Blundy JD (1993) Emplacement-related deformation of granitoid magmas, southern Adamello Massif, Italy. Geol Soc Am Bull 105: 1517–1541

Kelley SP, Spray JG (1997) A late Triassic age for the Rochechouart impact structure, France, Meteor. Planet Sci 32: 629-636

Kelley SP, Reddy SM, Maddock R (1994) Laser-probe Ar/Ar investigation of a pseudotachilyte and its host rock from the Outer Isles Thrust, Scotland. Geology 22: 443-446

Laubscher HP (1985) Large scale, thin-skinned thrusting in the southern Alps: kinematic models, Geol Soc Am Bull 96: 710-718

Lin A (2008) Fossil Earthquakes: the Formation and Preservation of Pseudotachylytes. In: Bhattacharji S, Neugebauer HJ, Reitner J, Stüwe K (Eds.). Lecture Notes in Earth Sciences, Springer-Verlag, Berlin, 111

Ludwig KR (1998) On the treatment of concordant uranium-lead ages. Geochim Cosmochim Acta 62: 665-676

Ludwig KR (2001a) A User's Manual for Isoplot/Ex rev. 2.49: A Geochronological Toolkit for Microsoft Excel. Berkeley Geochronological Center, Sp. Publ. N^{o} 1A

Ludwig KR (2001b) SQUID 1.02: A User's Manual. Berkeley Geochronological Center, Sp. Publ. N^{o} 2

Magloughlin JF, Spray JG (1992) Frictional melting processes and products in geological materials: introduction and discussion. In: Magloughlin JF, Spray JG (Eds), Frictional melting processes and products in geological materials. Tectonophysics 204: 197-204

Magloughlin JF, Hall CM, Van der Pluijm BA (2001) ^{40}Ar-^{39}Ar geochronometry of pseudotachylytes by vacuum encapsulation: North Cascade Mountains, Washington, USA. Geology 29: 51-54

Malusà MG, Villa IM, Vezzoli G, Garzanti E (2010) Detrital geochronology of unroofing magmatic complexes. Abstract at EGU General Assembly 2010

Maroni M, Rebay G, Spalla MI (1995) Foliation mapping at the eastern border of the Orobic Alps, Central Southern Alps, Italy: a method of regional scale correlation in polydeformed metamorphic terrains. Mem Sci Geol 47: 275-285

Martin S, Prosser G, Santini L (1991) Alpine deformation along the Periadriatic lineament in the Italian Eastern Alps. Ann Tect 5: 118–140

Maxelon M, Mancktelow NS (2005) Three-dimensional geometry and tectonostratigraphy of the Pennine Zone, Central Alps, Switzerland and Northern Italy. Earth Sci Rev 71: 171-227

Mayer A, Cortiana G, Dal Piaz GV, Deloule E, De Pieri R, Jobstraibizer P (2003) U/Pb single zircon ages of the Adamello baholith, Southern Alps. Mem Sc Geol (Padova) 55: 151-167

Meier A (2003) The Periadriatic Fault System in Valtellina (N-Italy) and the Evolution of the Southwestern Segment of the Eastern Alps. [Ph.D thesis] : 190 pp. Zurich, Switzerland, ETH

McDonough WF, Sun SS (1995) The composition of the Earth. Chem Geol 120: 223-253

Milano PF, Pennacchioni G, Spalla MI (1988) Alpine and pre-Alpine tectonics in the Central Orobic Alps (Southern Alps). Eclog Geol Helv 81: 273-293

Montrasio A, Bersezio R, Forcella F, Jadoul F, Sciesa E (1994) Geological interpretation of the profile CROP – Central Alps – (Passo Spluga – Bergamo). In: Montrasio A, Sciesa E (eds) Proceedings of Symposium 'CROP-Alpi Centrali'. Quad Geodin Alp Quat 2: 171-186

Müller W, Kelley SP, Villa IM (2002) Dating fault-generated pseudotachylytes: comparison of $^{40}Ar/^{39}Ar$ stepwise-heating, laser ablation and Rb-Sr microsampling analyses. Contrib Mineral Petrol 144: 57-77

Nasdala L, Hofmeister WG, Norberg N, Mattinson JM, Corfu F, Dorr W, Kamo SL, Kennedy AK, Kronz A, Reiners PW, Frei D, Kosler J, Wan YS, Gotze J, Hager T, Kröner A, Valley JW (2008) Zircon M257 - a homogeneous natural reference material for the ion microprobe U-Pb analysis of zircon. Geostand Res 32: 247–265

Neubauer F, Genser J, Handler R (2000) The Eastern Alps: Result of a two-stage collision process. Mitt Öst Geol Ges 92:117-134.

O'Hara KD (2001) A pseudotachylyte geothermometer. J Struct Geol 23: 1345-1357

Pennacchioni G, Di Toro G, Brack P, Menegon L, Villa IM (2006) Brittle-ductile-brittle deformation cooling of tonalite (Adamello, Southern Alps) Tectonophysics 427: 171-197

Petermann ZE, Day W (1989) Early Proterozoic activity on Archean faults in the western Superior province. Evidence from pseudotachylite. Geology 17: 1089–1092

Philippi E (1895) Beitrag zur Kenntnis des Aufbaues der Schichtenfolge im Grignagebirge. Ztschr der Dten Geol Ges, pp 665-735, Berlin

Pieri M, Groppi G (1981) Subsurface geological structure of the Po plain, Italy. Progetto Finalizzato Geodinamica CNR, publ 414

Polino R, Dal Piaz GV, Gosso G (1990) Tectonic erosion at the Adria margin and accretionary processes for the Cretaceous orogeny of the Alps. Vol Spec Soc Geol It 1: 345-367

Porro C (1903) Alpi Bergamasche, Carta 1:100000 con sezioni geologiche. Milano

Ravaglia A, Seno S, Toscani G, Fantoni R (2006) Mesozoic extension controlling the Southern Alps thrust front geometry under the Po Plain, Italy: Insights from sandbox models. J Struct Geol 28: 2084-2096

Ravazzi C, Moscariello A (1998) Sedimentation, palaeoenvironmental evolution and time duration of earliest Pleistocene climatic cycles in the 24-56 m FM-core interval (Leffe Basin, northern Italy). In: Van Kolfschoten Th. - Gibbard P (eds): Proceedings of the INQUA-SEQS Symposium "The Dawn of the Quaternary". Medelingen Nederlands Instituut vor Toegepaste Geowetenschappen, 60: 467-490

Renne PR, Swisher CC, Deino AL, Karner DB, Owens TL, De Paolo DJ (1988) Intercalibrations of standards, absolute ages and uncertainties in $^{40}Ar/^{39}Ar$ dating. Chem Geol 145: 117-152

Rodeghiero F, Vailati G (1978) Nuove osservazioni sull'assetto geologico-strutturale del settore centrale del distretto piombo-zincifero di Gorno (Alpi Bergamasche). L'Industria Mineraria, settembre-ottobre 29: 298-302

Roeder D (1992) Thrusting and wedge growth, Southern Alps of Lombardia (Italy). In: Freeman R and Mueller St (Eds): The European Geotraverse, Part 8. Tectonophysics 207: 199-243

Schmid SM, Zingg A, Handy M (1987) The kinematics of movement along the Insubric Line and the emplacement of the Ivrea Zone. Tectonophysics 135: 47-66

Schmid SM, Aebli HR, Heller F, Zingg A (1989) The role of the Periadriatic Line in the tectonic evolution of the Alps. In: Coward MP, Dietrich D, Park RG (eds) Alpine tectonics Geol Soc Sp Publ 45: 153-171

Schmid SM, Fügenschuh, Kissling E, Schuster R (2004) Tectonic map and overall architecture of the Alpine orogen. Eclogae Geol Helv 97: 93-117

Schmid SM, Bernoulli D, Fügenschuh B, Matenco L, Schefer S, Schuster R, Tischler M, Ustaszewski K (2008) The Alpine-Carpathian-Dinaridic orogenic system: correlation and evolution of tectonic units. Swiss J Geosc 101 : 139-183

Schoene B, Crowley JL, Condon DJ, Schmitz MD, Bowring SA (2006) Reassessing the uranium decay costants for geochronology using ID-TIMS U-Pb data. Geochim Cosmochim Acta 70: 426-445

Schönborn G (1992) Alpine tectonics and kinematic models of the central Southern Alps. Mem Sci Geol (Padova) 44: 229-393

Sciunnach D, Tremolada F (2004) The Lombardian Gonfolite Group in Central Brianza (Como and Milano Provinces, Italy): Calcareous nannofossils biostratigraphy and sedimentary record of neo-alpine tectonics. Eclogae Geol. Helv 97: 119-131

Scrocca D, Doglioni C, Innocenti F, Manetti P, Mazzotti A, Bertelli L, Burbi L, D'Offizi S (eds) (2003) CROP Atlas: Seismic Reflection Profiles of the Italian Crust. Mem Descr Carta Geol Italia 62: 1-194

Sherlock SC, Strachan RA, Jones KA (2009) High spatial resolution $^{40}Ar/^{39}Ar$ dating of pseudotachylytes: geochronological evidence of multiple phases of faulting within basement gneisses of the Outer Hebrides (UK). J Geol Soc 166: 1049-1059

Sibson R (1975) Generation of pseudotachylite by ancient seismic faulting. Geophys J Royal Astr Soc 43: 775–794

Siletto G (1990) Polyphase tectonics in the Orobic basement of Passo San Marco (Upper Val Brembana, Southern Alps, Italy). Mem Soc Geol It 45: 101-105

Siletto GB, Spalla MI, Tunesi A, Lardeaux JM, Colombo A (1993) Pre-Alpine structural and metamorphic histories in the Orobic Southern Alps, Italy. In: Von Raumer JF, Neubauer F (eds) Pre-Mesozoic Geology in the Alps. Springer-Verlag, Heidelberg 585-598

Spalla MI, Gosso G (1999) Pre-Alpine tectonometamorphic units in the central Southern Alps: structural and metamorphic memory. Mem Sci Geol (Padova) 51: 221-229

Spalla MI, Carminati E, Ceriani S, Oliva A, Battaglia D (1999) Influence of deformation partitioning and metamorphic re-equilibration on P-T path reconstruction in the pre-Alpine basement of Central Southern Alps (Northern Italy). J Metamorphic Geol 17: 319-336

Spray JG (1987) Artificial generation of pseudotachylyte using friction welding apparatus: simulation of melting on a fault plane. J Struct Geol 9: 49-60

Spray JG (1992) A physical basis for the frictional melting of some rock forming mineral. Tectonophysics 204: 205-221

Steiger RH, Jäger E (1977) Subcommission on Geochronology: convention on the use of decay constants in geo- and cosmochronology. Earth Planet Sci Lett 36: 359-362

Stipp M, Stünitz H, Heilbronner R, Schmid SM (2002) The eastern Tonale fault zone: a "natural laboratory" for crystal plastic deformation of quartz over a temperature range from 250 to 700°C. J Struct Geol 24: 1861-1884

Stipp M, Fügenschuh M, Gromet B, Stünitz LP, Schmid SM (2004) Contemporaneous plutonism and strike-slip faulting: A case study from the Tonale fault zone north of the Adamello pluton (Italian Alps). Tectonics, 23: TC3004, doi: 10.1029/2003TC001515

Stüwe K, Schuster R (2010) Initiation of subduction in the Alps: Continent or ocean? Geology 38(2): 175-178

Swanson MT (1992) Fault structure, wear mechanism and rupture processes in pseudotachylyte generation. Tectonophysics 204: 223-242

Passchier CW, Trouw RAJ (2006) Microtectonics. Springer-Verlag, Heidelberg, Berlin.

Taramelli T (1890) Carta Geologica della Lombardia 1:250000

Tera F, Wasserburg G (1972) U-Th-Pb systematics in three Apollo 14 basalts and the problem of initial Pb in lunar rocks. Earth Planet Sci Lett 14: 281-304

Thomas WA (1990) Controls on locations of transverse zones in thrust belts. Ecl Geol Helv 83(3): 727-744

Thöni M, Jagoutz E (1993) Isotopic constraints for the eo-Alpine high-P metamorphism in the Austroalpine nappes of the Eastern Alps: bearings on Alpine orogenesis. Schweiz Mineral Petrogr Mitt 73: 177-189

Thöni M (2006) Dating eclogite-facies metamorphism in the Eastern Alps - approaches, results, interpretation: a review. Mineral & Petrol 88: 123-148

Thöni M, Miller C, Blichert-Toft J, Whitehouse MJ, Konzett J, Zanetti A (2008) Timing of high-pressure metamorphism and exhumation of the eclogite type-locality (Klupperbrunn-Prickler Halt, Saualpe, south-eastern Austria): constraints from correlations of the Sm-Nd, Lu-Hf, U-Pb and Rb-Sr isotopic systems. J Metam Geol 26: 561-581

Trümpy E (1930) Beitrag zur Geologie der Grigna-gruppe am Comersee (Lombardei). Ecl Geol Helv 23: 375-487

Vailati G (1966) Concentrazioni di minerali di piombo e zinco legate a fenomeni tettonici nel giacimento di Gorno. Simposium internazionale sui giacimenti minerari delle Alpi. Trento, Mendola 11-18 Settembre.

Vance D, Müller W, Villa IM (2003) Geochronology: linking the isotopic record with petrology and textures - an introduction, in: Vance D, Müller W, Villa MI (Eds), Geochronology: linking the isotopic record with petrology and textures. Geol Soc London Spec Pub 220: 1-24

Van der Pluijm BA, Hall CM, Vrolijk P, Pevear DR, Covey M (2001) The dating of shallow faults in the Earth's crust. Nature 412: 172-174

Villa IM, Ruffini R, Rolfo F, Lombardo B (1996a) Diachronous metamorphism of the Ladakh terrain at the Karakorum – Nanga Parbat – Haramosh junction (NW Baltistan, Pakistan). Schweitz Mineral Petrogr Mitt 76: 245-264

Villa IM, Grobéty B, Kelley SP, Trigila R, Wieler R (1996b) Assessing Ar transport paths and mechanisms in the McClure Mountains horneblende. Contrib Mineral Petrol 126:67-80

Villa IM, Hermann J, Müntener O, Trommsdorff V (2000) ^{39}Ar-^{40}Ar dating of multiply zoned amphibole generations (Malenco, Italian Alps). Contrib Mineral Petrol 140: 363–381

Von Eynatten H, Gaupp R (1999) Provenance of Cretaceous synorogenic sandstones in the Eastern Alps:

constraints form framework petrography, heavy minerla analysis and mineral chemistry. Sed Geol 124: 81-111

Wagner G, Van den Haute P (1992) Fission-Track Dating. Kluwert Academic Press

Watson EB, Cherniak DJ, Hanchar JM, Harrison TM, Wark DA (1997). The incorporation of Pb into zircon. Chem Geol 141: 19-31

Williams IS (1998) U-Th-Pb geochronology by ion microprobe. In: McKibben MA, Shanks III WC, Ridley WI (eds) Applications of microanalytical techniques to understanding mineralizing processes. Rev Econ Geology 7: 1-35

Winchester JA, Floyd PA (1977) Geochemical discrimination of different magma series and their differentiation products using immobile elements. Chem Geol 20: 325-343

Winterer EL, Bosellini A (1981) Subsidence and sedimentation on Jurassic passive continental margin. Am Ass of Petr Geol Bull 65: 394-421

Zanchetta S, D'Adda P, Zanchi A, Barberini V, Villa IM (2010) Cretaceous-Eocene compression in the central Southern Alps (N Italy) inferred from $^{40}Ar/^{39}Ar$ dating of pseudotachylytes along regional thrust faults. J Geodyn, doi: 10.1016/j.jog.2010.09.004

Zanchi A, Forcella F, Jadoul F, Bernini M, Bersezio R, Fornaciari M, Rosetti R, Torazzi S (1988) The Faggio-Morterone transverse line: mesoscopic analysis and kinematic implications. Ren Soc Geol Ita 11: 279-286

Zanchi A, Chiesa S, Gillot PY (1990a) Tectonic evolution of the Southern Alps in the Orobic chain: structural and geochronological indications for pre-Tertiary compressive tectonics. Mem Soc Geol It 45: 77-82

Zanchi A, Chinaglia N, Conti M, De Toni S, Ferliga C, Tsegaye A, Valenti L, Bottin R (1990b) Analisi strutturale lungo il fronte della Dolomia Principale in bassa Val Seriana (Bergamo). Mem Soc Geol Ita 45: 83-92

Zanchi A, Salvi F, Zanchetta S, Sterlacchini S, Guerra G (2009) 3D reconstruction of complex geological bodies: Examples from the Alps. Comp & Geosc 3: 49-69

ACKNOWLEDGEMENTS

I would like to thank Prof. Andrea Zanchi for giving me the opportunity to work on this interesting and fascinating project. This work is the result of a number of observations and ideas that he has developed during more than 20 years of studies and field activities in the Orobic Alps. His scientific support and constant encouragement have been fundamental for me during these three years.

I'm also grateful to Dr. Stefano Zanchetta for patiently helping me during the realization of many parts of this thesis and for his reading and correcting the entire manuscript. His work and support have been fundamental, especially during field activity and structural analysis in the crystalline basement, during pseudotachylytes samples analysis, $^{40}Ar/^{39}Ar$ dating and related data processing.

Thanks to Dr. Maria Bergomi for her great help during zircon samples separation, U-Th-Pb zircon dating and data processing.

Thanks to Dr. Marco Malusà for his help during apatite samples separation and preparation, and for teaching me the basic techniques for apatite fission-track analysis.

Also thanks to Dr. Fabrizio Berra for his suggestions and observations during field activity in the Gandino and Val Vedra areas, to Prof. Igor M. Villa for his help during $^{40}Ar/^{39}Ar$ dating of pseudotachylyte samples, to Dr. Valentina Barberini and Dr. Nicoletta Fusi for their support during Micro CT analysis of pseudotachylyte veins.

A special thank goes to Alberto Resentini, Marta Padoan, Marta Limoncelli for all the fun times that we spend together during these years.

Finally, I want to so sincerely thanks my girlfriend Mary for her precious and constant presence, my mother, my father, my sister and my brother for their daily encouragement.

APPENDIX 1

$^{40}Ar/^{39}Ar$ dating of fault-generated pseudotachylytes

1. General principles

The $^{40}Ar/^{39}Ar$ procedure is based on the conversion of ^{39}K into ^{39}Ar through radiation with fast neutrons in a nuclear reactor, permitting the K determination to be made as a part of the Ar isotope analysis. After the irradiation, all five Ar isotopes are measured (^{40}Ar, ^{39}Ar, ^{38}Ar, ^{37}At,^{36}Ar) and the age of the selected sample is calculated from the ratio of the radiogenic daughter product ^{40}Ar to ^{39}Ar (as a proxy for ^{40}K):

$$t = (1/\lambda) \, \mathrm{Ln}[J \, (^{40}Ar/^{39}Ar) + 1]$$

where t is the age of the sample, λ is the decay constant of ^{40}K and J is a parameter that takes into account the intensity, duration and spatial heterogeneity of neutron irradiation.

The measurement of the Ar signature of a selected sample after irradiation can be investigated trough IR or UV $^{40}Ar/^{39}Ar$ laser microprobe spot dating technique or by stepwise-heating experiments (Kelley et al., 1994; Müller et al., 2002; Sherlock et al., 2009). The great advantage of the stepwise-heating technique is that it allows to identify the occurrence of different chemical reservoirs within the sample: different domains are differently susceptible to diffusional Ar loss and consequently break down at different temperatures (Müller et al., 2002). The results of a step-heating experiment are normally displayed in an $^{40}Ar/^{39}Ar$ age spectrum plot (i.e. Fig. 3.1.1 and 3.1.2). The determination of a reliable age from the spectrum plot depends on the identification of an “age-plateau”, which is defined by a series of adjacent steps comprising at least the 50% of the total argon release.

However, a major problem is represented by discordant and irregular age spectra which cannot be interpreted with a conventional approach, and both mineralogy and differential breakdown during laboratory degassing must be taken into account (Villa *et al*., 1996a, b, 2000; Müller *et al*., 2002). The $^{38}Ar/^{39}Ar$ and $^{37}Ar/^{39}Ar$ ratios of each heating step can be considered as good approximation of the Cl/K and Ca/K ratios of the phase that provides most gas during the step. For this reason, age spectra have to be interpreted together with chemical information provided by Ar isotopes from K, Ca and Cl produced during radiation in the nuclear reactor, and independent chemical data provided by EMPA and SEM (Villa *et* al., 2000; Müller *et al*., 2002).

This approach is crucial for $^{40}Ar/^{39}Ar$ dating of pseudotachylytes, since they represent complex systems composed of melt, clasts and alteration phases. The chemical control from both Ar isotopes (Cl/K and Ca/K ratios) and EMPA analyses yields accurate melt-related ages, even in cases of complex age spectra, and is thus fundamental for their discrimination.

2. Samples analysis by EMPA and SEM

Polished thin sections used for petrographical characterisation, SEM (Scanning Electron Microscope) and EMPA (Electron Micro-Probe Analyses) investigations and analyses were cut from the opposite face of

rock chips later drilled to obtain micro-cores for stepwise heating experiments.

The chemical composition of pseudotachylyte matrix has been determined with a Jeol JXA 8200 Superprobe (Department of Earth Sciences, University of Milano), equipped with five WDS (wave-length-dispersive) and one EDS (energy-dispersive) spectrometers. Natural silicates have been used as standards. Matrix analyses were performed with 5 μm to 10 μm beam diameter at 15 kV and 5 nA of beam current in order to avoid Cl, Na and K diffusion. Resulting data have been processed trough a ZAF correction procedure. The most of the samples have been also investigated with a EDS-equipped SEM (Department of Geosciences and Geotechnologies, University of Milano-Bicocca) to check the textural characteristics previously observed with the optical microscope.

3. Sample preparation

A number of micro-cores was produced from each rock sample of interest. They were collected from polished faces of rock chips using a vertical drill equipped with micro corers. Each obtained micro-core had a diameter of 1 to 4 millimetres and an approximate weight of 70-100 mg. All cores were finally cleaned ultrasonically in deionized water.

It is well acknowledged that pseudotachylytes can contain a variable amount of inherited clasts/minerals older than the pseudotachylyte itself. The occurrence of mixed mineral generations if remains undetected would lead to systematic inaccuracies in dating (Müller *et al.*, 2002; Vance *et al.* 2003). In order to minimize this undesired effect, all the micro-cores were screened with an X-ray Micro Computed Tomography (MicroCT).

4. Sample analysis by X-ray Micro Computed Tomography (microCT)

Drilled micro-cores were analysed by X-ray Micro Computed Tomography (MicroCT) combined with image analysis techniques in order to asses in three dimension the clast/matrix ratio for each pseudotachylyte sample to be analysed for $^{40}Ar/^{39}Ar$ dating.

X-ray microCT produces stacks of two-dimensional grey-value images (referred to as “slices”) that reveal the interior of an object as if it had been sliced open for viewing. The contrast in a X-ray CT image is generated by differences in X-ray absorption within the scanned object, mainly depending on density and chemical composition (i.e. mean atomic number) variations throughout the object. A clear and exhaustive explanation about how the technique works can be found in Denison *et al.* (1997).

MicroCT analyses were performed with a BIR Actis 130/150 Desktop Micro-focus CT/DR system (Department of Geosciences and Geotechnologies, University of Milano Bicocca). The cores were fixed to a plastic sample holder with their longitudinal axis in vertical position. The x-ray tube was supplied with an energy of 100 keV and 80 mA. The dimensions of the voxel (3D pixel, which indicates the resolution of the images) of the obtained images are: x, y = 0.0025 mm, x = 0.0027 mm. Each 2D image (slice) represents a sample thickness of 0,0027 mm. The maximum resolution achieved after image processing of raw data was in the order of 5-10 μm.

The obtained 3D microCT image stacks were processed with the NIH-ImageJ software (NIH: http://rsbweb.nih.gov/ij/). The aim of image analysis work was to select micro-cores with the lowest clast/matrix ratio in order to minimize the inherited, i.e. clast-related, Ar component during stepwise heating experiments. Pseudotachylyte matrix appears generally lighter in colour than quartz, plagioclase and also lithic clasts, commonly dominated by quartz. In order to automatically perform the image processing the grey-scale threshold values used to identify inherited clasts were defined by comparison with SEM images (100 to 1200 X).

Three micro-cores, preventively scanned with MicroCT, then cut perpendicular to their longitudinal axis, mounted in araldite, polished with diamond paste and coated with graphite. BSE (Back Scattered Electrons) images were combined with qualitative EDS analyses to identify mineral phases. The comparison between SEM data and corresponding MicroCT slices allowed the definition of accurate greyscale threshold values for each mineral phase to be used for image processing. Manual correction were later performed on processed MicroCT stacks of images to eliminate the outer rim of the micro-cores, usually falling within the threshold window of quartz due to "edge effect" during acquisition.

5. $^{40}Ar/^{39}Ar$ dating

Selected micro-cores were cleaned ultrasonically in deionized water and then wrapped in aluminium foil. Samples and standards were irradiated for 5 hours in a fast neutron flux at the *Triga Mark II* reactor at the University of Pavia (Italy).

Stepwise heating experiments were performed at the Geochronology Laboratory of University of Bern (Switzerland). Samples were loaded in a double vacuum resistance furnace attached to a SAES C50 Zr-Al getter pump . The samples were heated in 10 or 11 steps for 15 to 30 minutes at temperatures from 500°C to 1400°C. The released gas was transferred in 7 minutes to a second getter (AP10) and, after additional 15 to 45 min cleaning up, the gas was led to a MAP215-50B rare gas mass spectrometer. The gas was measured through a Faraday cup in peak jumping mode between 35.5 and 40.5 mass. Analytical data of $^{40}Ar/39^{Ar}$ stepwise-heating experiments are reported in Table 3.1.3 after machine background and ^{37}Ar decay corrections only. To calculate ages (relative to a MMhb-1 standard age of 523.1 Ma, see Renne *et al.*, 1998) the following interference corrections were used: $(^{39}Ar/^{37}Ar)_{Ca}$ = 0.00067;$(^{36}Ar/^{37}Ar)_{Ca}$ = 0.000255; $(^{40}Ar/^{39}Ar)_{K}$ = 0.011.

APPENDIX 2

SHRIMP U-Th-Pb analytical techniques

1. Samples preparation

Zircon separation was carried out at laboratories of the Department of Geological Sciences and Geotechnologies of the University of Milan-Bicocca. After crushing and sieving, the heavy mineral fraction, including both zircon and apatite, was separated using a Wilfley table. Magnetic minerals (i.e. magnetite, amphiboles, pyroxenes, biotite and muscovite) were removed using a Frantz magnetic separator, under increasing field strengths from 0.2 to 1.0 A. The remaining quartz-feldspathic fraction was passed through different heavy liquids: tetrabromoethane (2.963 g/cm^3) allows the separation of zircon and apatite from most of the remaining heavy minerals, while zircon (4.6 - 4.7 g/cm^3) was then separated from apatite (3.1 - 3.35 g/cm^3) using the di-iodomethane (3.35 g/cm^3). Mineral concentrates were then washed with acetone and dried. About 100-150 individual zircon crystals were finally hand picked using an optical microscope.

Crystals were mounted in an epoxy resin disc with several pieces of Temora zircon standard (Black et al. 2003) at laboratories of Chinese Academy of Geological Sciences. The disc was ground-down and polished so as to effectively section the zircons in half. Zircon grains were imaged optically using reflected and transmitted light. The mount was carbon coated for cathodoluminescence (CL) imaging and then cleaned and gold coated in readiness for ion microprobe analysis.

2. Samples dating, calibration and standards

U-Th-Pb analyses were carried out at the new SHRIMP Remote Operation System (SROS) lab at the University of Milano-Bicocca (Italy) using the SHRIMP II ion microprobe located at the Beijing SHRIMP Centre, Chinese Academy of Geological Sciences. Instrumental conditions and data acquisition were generally as described by Compston et al. (1992) and Williams (1998). An average mass resolution of > 5000 (1%) was obtained during measurement of Pb/Pb and Pb/U isotopic ratios. Five scans through the masses Zr_2O^+, $^{204}Pb^+$, $^{206}Pb^+$, $^{207}Pb^+$, $^{208}Pb^+$, $^{238}U^+$, $^{248}ThO^+$, and $^{254}UO^+$ were made for each age determination. The zircon standards used were M257 (561.3 ± 0.3 Ma, U ~ 840 ppm, Th/U ~ 0.27; Nasdala et al. 2008) for U concentrations and Temora (416.8 ± 1.1 Ma; Black et al. 2003) for interelement fractionation. The beam size was ~20-25 μm and each analysis spot was rastered over 120–200 s prior to analysis, in order to remove any common Pb on the surface or contamination from gold coating. The ^{235}U decay constant used for age calculation is after Schoene et al. (2006), whereas the ^{238}U one is after the IUGS Subcommission on Geochronology (Steiger and Jäger 1977).

APPENDIX 3

Apatite fission track dating

1. Method

Two different techniques are generally used to calculate fission track ages: the population method and the external detector method. The latter has been used in this work.

The *population method* (POP) is based on the determination of spontaneous and induced track densities on two different groups of crystals of the same sample (Wagner & Van den Haute, 1992). This procedure implicitly assumes that the U distribution is uniform in the numerous analyzed grains of a certain sample and is inappropriate, for example, for analyzing strongly zoned grains.

With the *external detector zeta (ζ) calibration method* (EDM) fission track ages are determined on individual grains. Uncertainties inherent the thermal flux and the fission decay constants are avoided and the assumption of uniform uranium distribution in a given population of grains is made unnecessary. For this method the fundamental fission track age equation is:

$$t = (1/\lambda_d)\ \mathrm{Ln}[\lambda_d\ (\rho_s/\rho_i)\ \rho_d\ \zeta\ g + 1] \qquad (1)$$

where t is the age, ρ_s and ρ_i are the spontaneous and induced track densities (tracks / unit area), λ_d is the α-decay constant of ^{238}U, ρ_d is the track density in a glass of known uranium concentration (dosimeter) insert in the samples holder to monitor the neutron flux of the reactor, g is a geometry factor (usually = 2) and ζ is a constant of proportionality which has to be determined for each individual analyst using samples of known ages (at least 5 analyses on standard samples in different irradiations are required to obtain a credible value). Once ζ has been determined, ρ_s and ρ_i are the fundamental values which have to be measured by counting of fission tracks under an optical microscope.

The size of induced tracks is normally about 3-14 nm in width (Paul and Fitzgerald, 1992) and the use of a transmission electron microscope represents the only way to observe them (Gallagher et al., 1998). However, they can be opened and enlarged for ordinary optical microscope observations with a simple chemical etching procedure, since they are much more reactive with respect to the surrounding undamaged lattice (Wagner & Van den Haute, 1992). In apatite, etched tracks form almost cylindrical holes, 1-2 μm wide and about 16 μm long. The etching rate usually vary with the crystallographic orientation of the etched surface and this is the factor that controls the shape and the orientation of etch pits (intersections of fission tracks with the polished surface). A complete parallelism of etch pits can be observed only on c-axis parallel surfaces which are preferred for fission track counting as they guarantee the most uniform etching degree.

After etching the polished surface of an epoxy resin mount containing selected apatite crystals, an essentially U-free detector (typically a foil of white mica) is sealed against such a surface. The obtained sandwich is then irradiated, in a nuclear reactor, with low-energy thermal neutrons, inducing fission in ^{235}U. During this process, a mirror image of each grain forms on the detector as some heavy particles can

cross the interface between the mineral and mica producing damages through its crystal lattice. Subsequently only the mica is etched to reveal induced tracks. By counting the number per unit area of induced tracks in the mica (ρ_i) it is possible to estimate the ^{235}U (parent) concentration of the mineral grain, which in turn allows to calculate the ^{238}U concentration as the $^{235}U/^{238}U$ ratio is constant and known. On the other hand, by counting the number per area of spontaneous fission tracks in the mineral (ρ_s), we can estimate the concentration of the daughter products. Once obtained the values of ρ_i and ρ_s it is possible to apply equation (1) to calculate the fission track age.

The fission track age is usually reported as an average estimate of the individual single grain ages (at least 20, when possible), and three "mean age estimate" are generally used: mean, pooled and central ages. The first is represented by the sum of the counted spontaneous tracks divided by the sum of the counted induced tracks, while the second is the arithmetic mean of the individual crystal ratios of spontaneous to induced tracks. The central age is the preferred sample age estimate, and is calculated as the weighted mean of the log normal distribution of single grain ages (Galbraith & Laslett, 1993). The three estimated ages are essentially the same when the variation in the count population is represented by a Poisson distribution.

2. Samples preparation and fission track counting

Samples for apatite fission track dating were processed using the same procedure described for SHRIMP U-Th-Pb zircon dating (see Appendix 2). After heavy liquids separation, apatite concentrates were mixed with epoxy resin on a microscope slide. The distribution of grains was done under a low-magnification microscope, in order to better distribute crystals and obtaining a single layer. After hardening the resin with a hot plate, apatite mounts were hand-ground using wet grinding papers until sufficient internal cross-sections of apatite grains were exposed. Mounts were finally polished with a polishing machine using a 3 μm diamond slurry on a felt cloth for about 10 minutes and then repeating this process using a 1 μm diamond slurry on a different felt cloth. To enlarge spontaneous fission tracks on apatite crystals for optical microscope observations all polished samples were then chemically etched. Each mount was put in HNO_3 5M for 20 seconds and immediately washed for few minutes. Glasses were then cut according to the size of mounts (about 10x15 mm) and one of the corner was smoothed. A 0.1-0.3 mm thick, U-free muscovite sheet was cut according to the size of each mount, put in contact with the polished surface an fixed with adhesive tape. Samples, standards and dosimeters (CN-5) were put in a holder and fixed with a screw. Dosimeters were positioned both at the top and at the bottom of the holder to have the maximum control on the neutron fluence. Standards were preferentially put closed to them. Samples were irradiated in the atomic reactor "TRIGA Mk II" of the Oregon State University (U.S.A.) and, after irradiation, a period of about two months has been required to allow the radioactivity to reach acceptable levels. Subsequently, the muscovite sheets were put in a PVC container with HF 40% for 45 minutes in order to enlarge induced fission tracks for optical microscope counting. Muscovites were then washed with distilled water for few hours. Finally, each mount-mica couple was fixed on a microscope slide and a

label containing the sample name and irradiation numbers was put along a side of the slide.

According to the external detector method, spontaneous tracks density was measured on apatite crystals fixed on each mount while induced tracks density was measured on the corresponding mica. Counting of tracks was carried out using microscope equipped with a motorized stage, reflected and transmitted lights, and with a total magnification of *x*1250. Before counting the stage was calibrated to automatically move from an apatite crystal on the mount to the corresponding "imprint" on the mica. For each sample, when possible, twenty apatite grains were selected on the basis of some fundamental requirements: crystal section parallel to the *c*-axis (etch pits parallel to each other), no fractures, no inclusions and no zoning. On each chosen crystal, a certain area was selected using a grid inserted in the ocular, and induced tracks within that area were counted. Moving on the corresponding image on the mica, induced tracks number was determined within an area equal to that used for the crystal on mount.